UNIVERSIDADE FEDERAL DE SANTA CATARINA
CENTRO DE CIÊNCIAS FÍSICAS E MATEMÁTICAS
PROGRAMA DE PÓS-GRADUAÇÃO EM FÍSICA

Daniel Souza Lima

Self assembling of exotic superfluid modulated phases

Florianópolis
2025

Daniel Souza Lima

Self assembling of exotic superfluid modulated phases

Tese submetida ao Programa de Pós-Graduação em Física da Universidade Federal de Santa Catarina como requisito parcial para a obtenção do título de Doutor em Física.

Orientador: Prof. Alejandro Mendoza Coto, Dr.

Florianópolis
2025

Ficha catalográfica gerada por meio de sistema automatizado gerenciado pela BU/UFSC.
Dados inseridos pelo próprio autor.

Lima, Daniel Souza
Self assembling of exotic superfluid modulated phases / Daniel Souza Lima ; orientador, Alejandro Mendoza-Coto, 2025.
77 p.

Tese (doutorado) - Universidade Federal de Santa Catarina, Centro de Ciências Físicas e Matemáticas, Programa de Pós-Graduação em Física, Florianópolis, 2025.

Inclui referências.

1. Física. 2. Supersólidos. 3. Quasicristais quânticos. 4. Condensados de Bose-Einstein. 5. Interações dipolares. I. Mendoza-Coto, Alejandro . II. Universidade Federal de Santa Catarina. Programa de Pós-Graduação em Física. III. Título.

Daniel Souza Lima

Self assembling of exotic superfluid modulated phases

O presente trabalho em nível de Doutorado foi avaliado e aprovado, em 3 de setembro de 2025, pela banca examinadora composta pelos seguintes membros:

Prof. Alejandro Mendoza Coto, Dr.
Universidade Federal de Santa Catarina

Prof. Rogelio Díaz-Méndez, Dr.
BA Cloud Software & Services

Prof. Vinizius Zampronio Pedroso, Dr.
Università di Firenze

Prof. Lucas Nicolao, Dr.
Universidade Federal de Santa Catarina

Certificamos que esta é a versão original e final do trabalho de conclusão que foi julgado adequado para obtenção do título de Doutor em Física.

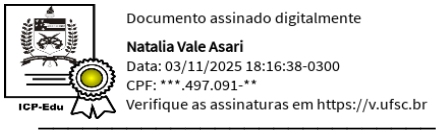

Prof. Natalia Vale Asari, Dra.
Coordenação do Programa de Pós-Graduação

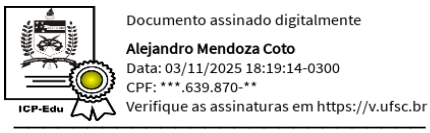

Prof. Alejandro Mendoza Coto, Dr.
Orientador

Florianópolis, 2025.

Statement of Authorship

I hereby declare that the thesis submitted is my own work. All direct or indirect sources used are acknowledged as references. I further declare that I have not submitted this thesis at any other institution in order to obtain a degree.

Acknowledgements

Este trabalho não seria possível sem a orientação paciente do Prof. Dr. Alejandro Mendoza-Coto, cuja sabedoria científica, dedicação e capacidade de enxergar além do óbvio foram fundamentais em cada etapa desta jornada. Sua orientação firme, porém respeitosa, foi um verdadeiro exemplo de como orientar com rigor e humanidade.

Também sou profundamente grato pelo apoio cuidadoso e constante de Carolina Gehring van Paemel, que esteve ao meu lado nos momentos mais desafiadores e compartilhou comigo as alegrias das pequenas e grandes conquistas ao longo do caminho.

Agradeço à Universidade Federal de Santa Catarina (UFSC) por proporcionar o ambiente acadêmico necessário para o desenvolvimento deste trabalho, bem como à Fundação de Amparo à Pesquisa e Inovação do Estado de Santa Catarina (FAPESC) e à Coordenação de Aperfeiçoamento de Pessoal de Nível Superior (CAPES) pelo suporte financeiro e institucional.

A todos os colegas do grupo de pesquisa, aos amigos que compreenderam minhas ausências e torceram por mim, e à minha família, que sempre acreditou em mim mesmo nos momentos em que eu duvidei — meu sincero muito obrigado.

Resumo

Esta tese aprofunda a compreensão teórica das fases supersólidas e quasicristalinas em condensados de Bose-Einstein, aplicando métodos variacionais baseados em séries de Fourier normalizadas e validando-os com a solução numérica da equação de Gross-Pitaevskii. O primeiro estudo explora como a inclinação do vetor de polarização dos dipolos afeta a densidade modulada do estado fundamental em geometria planar, revelando múltiplas fases (hexagonal, listras e favo de mel) e pontos críticos no diagrama de fases, além de anisotropias e deformações dependentes do ângulo de inclinação. O segundo estudo investiga, motivado por sistemas de QED em cavidade, como potenciais de interação projetados em espaço de momento podem estabilizar fases quasicristalinas superfluídas com simetrias octagonal, decagonal e dodecagonal, identificando as condições mínimas para sua estabilização e destacando a robustez particular da estrutura dodecagonal devido à sua rede vetorial única. Ambos os trabalhos mostram que essas fases exóticas apresentam superfluidez e contribuem para o avanço no entendimento de condensados de Bose-Einstein com interações inovadoras e propriedades emergentes.

Keywords: Supersólido. Quasicristal quântico. Condensado de Bose-Einstein. Campo Médio Variacional. Fases Exóticas da Matéria.

Abstract

This thesis advances the theoretical understanding of supersolid and quasicrystalline phases in Bose-Einstein condensates by applying variational methods based on normalized Fourier series and validating them with numerical solutions of the Gross-Pitaevskii equation. The first study investigates how tilting the dipole polarization vector in planar geometry affects the ground-state modulated density, revealing multiple phases (hexagonal, stripe, and honeycomb), critical points, and anisotropies in the phase diagram, as well as deformations in the density modulation depending on the tilt angle. The second study, motivated by cavity QED systems, explores how engineered interaction potentials in momentum space can stabilize superfluid quasicrystalline phases with octagonal, decagonal, and dodecagonal symmetries, identifying the minimal conditions for their stabilization and highlighting the particular robustness of the dodecagonal structure due to its unique wave vector lattice. Both works demonstrate that these exotic phases exhibit superfluidity, thus advancing the understanding of Bose-Einstein condensates with novel interactions and emergent properties.

Keywords: Supersolid. Quantum quasicrystal. Bose-Einstein condensate. Variational Mean-Field. Exotic Phases of Matter.

List of Figures

Contents

Parte I

Introduction

1 State of the art on supersolids

"By convention sweet and by convention bitter, by convention hot, by convention cold, by convention color; but in reality atoms and void."
Democritus

The Greek atomist[1] makes explicit the difference between the way which things might appear to the mundane perceptions - in terms of the convention *nomos* (*νόμος*) - and how they are in reality - the nature *physis* (*φύσις*). From the early intuitions to the contemporary understanding of Physics, the search for novel states of matter constitutes a long history of fundamental research in the field of many-body quantum physics.

This start with the foreseen prediction of the exotic state of matter comprised by macroscopic quantum effects, by hypothesizing a non-interacting Bose gas when cooled down to zero temperature, a scenario introduced by Albert Einstein [18], inspired by a work of Satyendra Bose [19] in 1924, who introduced the idea of counting microstates of indistinguishable quantum particles, deducing the Planck's distribution at the end of his paper. Einstein extended further into the discussion of a non-interacting ideal monoatomic gas. Another example is the discovery of superfluidity in liquid helium [20, 21], in which the liquid flows without viscosity, which causes for example the spectacular fountain effect [1][22], Figure 1.

Unlike a non-interacting gas, the interactions are relatively strong. The density of the liquid helium is high, so the system departs considerably from an ideal Bose gas description. The ground state has a small macroscopic occupancy[2]; hence, Einstein's approach would not suffice at the time. Additionally, the discovery of superconductivity back in 1911 by Heike Kamerlingh Onnes [24] had added one more strange phase of matter to be explained, which would satisfactorily happen more than 50 years later with the BCS theory of superconductivity [25]. In this theory, the gas of electrons in a metal forms the Cooper pairs, which is a result of the deformation of the positively charged ionic lattice of the metal caused by the electrons. These fermionic pairs behave as composite bosons that can undergo a condensation below a critical temperature, just as a weakly interacting Bose gas. Thus, different physical phenomena are described by the same mathematical pattern. Finally, the Bose-Einstein condensate (BEC from now on) of ^{87}Rb was observed only 71 years after the publication of Einstein and Bose, Fig. 2, by Anderson et al. [4].

The continuous development of theoretical physics has led to a deeper understanding

[1] None of Democritus' writings have survived; the knowledge of his vast body of work is almost wholly reliant on doxographical evidence [17].

[2] At $T = 0$, ^{4}He occupies around 10% of its $\mathbf{k} = 0$ one-body state [23].

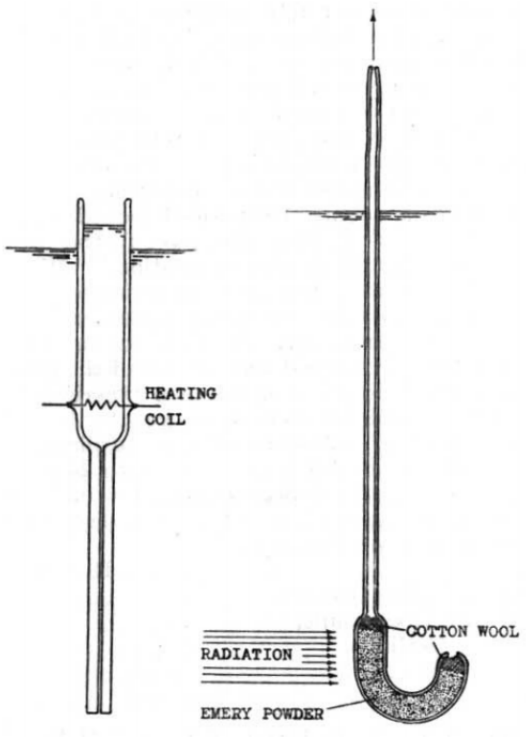

Fig. 1. Fig. 2.

Figure 1 – Original schematics depiction of the experimental setup created by Allen and Jones [1]. Either by a heating coil or by the thermal radiation of a 60 W bulb, only the inviscid superfluid can flow through the tubes obstructed with tightly packed emery powder or by cotton wool, and then spill a height of over 16 cm. In the heated region, there are thermally excited states, and the superfluid mode of the liquid is diminished, then superfluid diffuses into this region, to restore the equilibrium between normal liquid and superfluid (the two-fluid model of Helium superfluid, explained by Landau in 1937 [2, 3]).

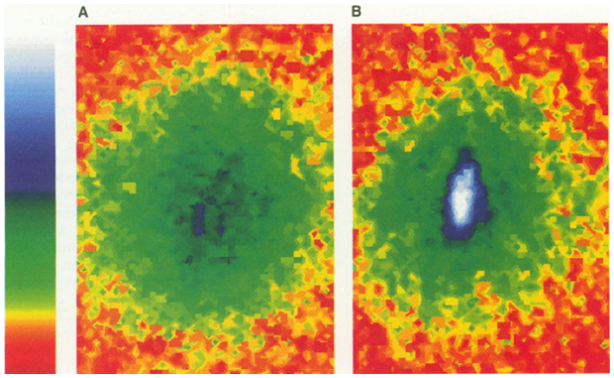

Figure 2 – The cloud's velocity distribution is illustrated using false-color in a field of view of each image is 200μm $\times$ by 270μ m. (a) An instant before the condensation. (b) After the condensation. Source: Anderson et al. [4].

of the *physis* of phase transitions and phases of matter, encompassing the concept of spontaneous symmetry breaking developed by Landau [26] and symmetry principles [27]. If the Lagrangian/Action of a system is invariant under transformations of a particular symmetry, one says this system has a symmetry. By these principles, conserved quantities and relevant observable objects can be determined. The phase transition is then associated with a quantity called *order parameter*, which would be zero in the disordered phase and non-zero in the ordered phase. For example, typically, in a two-dimensional ferromagnetic system of spins, when the temperature T is greater than $T_c \sim 2.27$K, the system has zero average magnetization (the disordered phase), but when $T < T_c$, the magnetization is

non-zero (ordered phase). The disordered phase is characterized by a ground state that remains invariant under all symmetry transformations of the Lagrangian. Conversely, the onset of order is marked by a non-zero order parameter. This ground state is no longer symmetric; it spontaneously selects one direction from the set of degenerate possibilities, thus breaking the original symmetry of the Lagrangian. These ideas have been applied to explain a multitude of phenomena, ranging from superfluidity, BEC, and ferromagnetism [26] in condensed matter physics, the electro-weak force in high energy physics [28, 29], and even the stock market [30].

Among these examples, the spontaneous breaking of translational symmetry and the global gauge symmetry of the Gross-Pitaevskii equation[3] have been the subject of investigation for a long time before the experimental realization of the BEC in 1995 [4]. The capacity of a system to exhibit a particular modulated pattern, or more accurately, a type of spatial *order*[4], has been tackled by the tools of condensed matter [32]. The interparticle pair interaction potential, $v(r)$, existing among a system's constituents, is the main ingredient that promotes the *self-assemble* into modulated phases. Either for quantum systems, or classical systems, it has been thoroughly proved that the capacity to form cluster crystals depends on the dimension of the system (one-, two-, or three-dimensions), and the Fourier transform of $v(r)$, $\hat{v}(k)$. Let us focus on two-dimensional classical soft systems, for which the $v(r)$ is bounded. Let us denote by Q^+-potential those systems whose $\hat{v}(k)$ has only a positive part, and by $Q^\pm$-potential those that change the signal. Then, systems with Q^+-potentials exhibit freezing followed by density-driven reentrance, e.g., Fig. 3(a) which show that a fluid phase surrounds the solid phase[5], as well as forming *simple crystals* (one occupancy per lattice cell). $Q^\pm$-systems, however, form stable solids at all temperatures (no reentrance), revealing clustering as the dominant stabilization mechanism [33, 34] (Fig. 4). In soft-core quantum systems, it is expected that the same conclusions from classical systems hold for finite temperature and zero-temperature [35, 36, 37].

Although we already have a criterion for cluster-crystal self-assembly, nothing is stated as to whether, for example, a two-dimensional system could self-assemble into an indefinitely extended, spatially periodic crystalline lattice at any temperature. We must avoid that assumption and move beyond a purely qualitative analysis. A more precise description therefore requires consideration of both positional and orientational order.

As a starting point, in one- and two-dimensional systems with sufficiently short-range interactions, the Mermin–Wagner theorem [32, 38, 39] prohibits spontaneous bre-

[3] The Gross-Pitaevskii equation is the Schrödinger equation for the wavefunction of the condensate [31].

[4] For solids, we would be most interested in the spatial correlation, the Debye-Waller factor, which is the correlation $\langle\hat{\rho}(\mathbf{r})\hat{\rho}(0)\rangle$, whose Fourier transform gives the X-ray structure factor, as well as in the orientational correlation function [32].

[5] i.e., as we dislocate through a horizontal line of density/pressure in a phase diagram with the start point at a homogeneous phase, as we vary the density along this horizontal line, eventually an inhomogeneous phase is achieved, and, then, we reenter in a homogeneous phase back again.

aking of continuous symmetries (e.g., global phase and translational) at any finite temperature. Furthermore, regarding the two-dimensional melting [40][6], the Kosterlitz–Thouless–Halperin–Nelson–Young (KTHNY) theory [41, 42] shows that, above zero temperature, two-dimensional systems lack true long-range positional order: they exhibit only quasi-long-range order up to a critical temperature—marked by power-law decay of spatial correlations [32]—and revert to exponential decay [32] above that temperature.

This remarkable result predicts a two-stage melting transition via an intermediate hexatic phase, in which the orientational correlations decay algebraically [40]. The hexatic phase arises from thermal unbinding of dislocation pairs, whereas the final transition to the isotropic fluid is driven by proliferation of free disclinations [40].

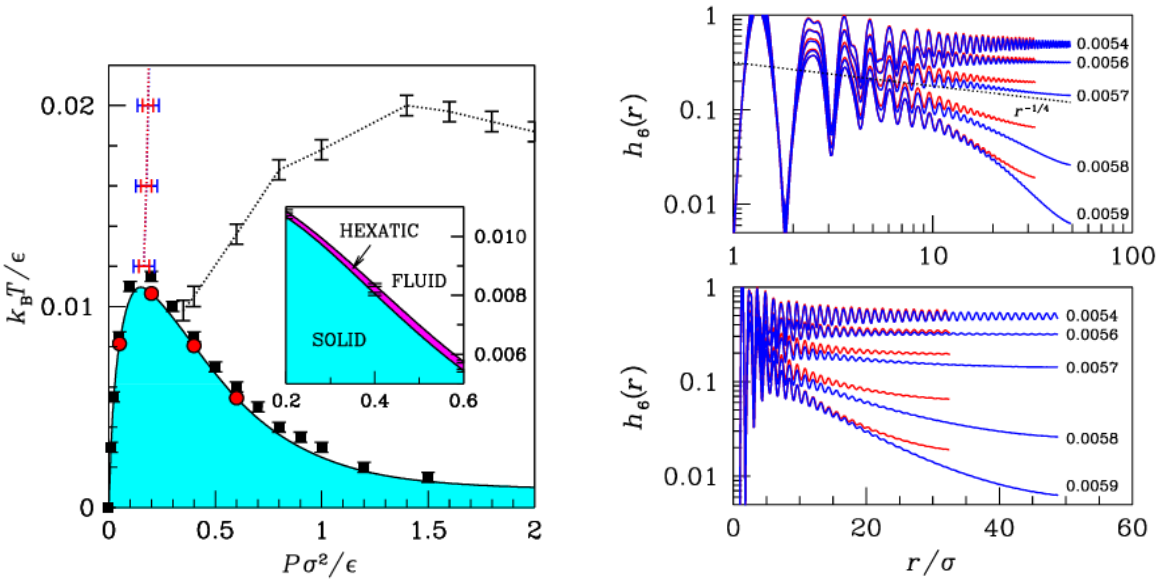

(a) (b)

Figure 3 – (a) Phase diagram (pressure × temperature) of 2D GEM2, a Q^+-potential that exhibits reentrance, for low temperatures, the hexatic phase is a thin region around the solid phase, with red dots at the computed solid-to-hexatic transition points. (b), The orientational correlation function computed for different Monte Carlo simulations, $N = 2688$ (red) and $N = 6048$ (blue). Top: log-log plot; bottom: log-lin plot. As the temperature T increases from 0.0054 to 0.0059, there is a qualitative change in the large-distance behaviour of correlation, from constant (solid) to power-law decay (hexatic fluid), up to exponential decay (normal fluid). Source: Prestipino et al. [5].

As an example, results of Monte Carlo simulations of two-dimensional GEM2 [5] and GEM4[7] [43] systems are shown in Figs. 3 and 4. The KTHNY theory predicts the algebraic decay $\sim r^{-\eta(T)}$ of the orientational correlation function in the hexatic phase versus exponential decay in the fluid, and a universal exponent $\eta = 1/4$ at the hexatic-fluid

[6] For a simple triangular crystal.

[7] A GEMα system means a system whose interparticle interaction potential has the mathematical form $\exp(-r^\alpha)$.

transition, which was seen in Fig. 3. In both cases, the solid phase exhibited quasi-long-range spatial order, which was accompanied by long-range orientational order.

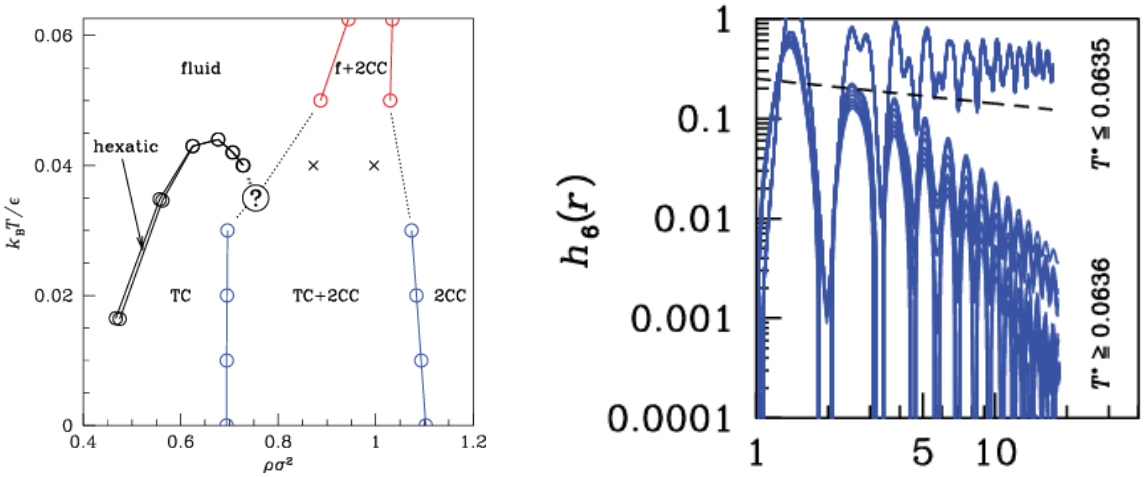

Figure 4 – (Left) Phase diagram (density × temperature) of 2D GEM4, a $Q^{\pm}$-potential that exhibits no reentrance. (Right) The orientational correlation function was computed by different Monte Carlo simulations. The black dashed line represents a hypothetical decay $r^{-1/4}$. Source: Prestipino et al. [6].

Another crucial aspect involves the spontaneous breaking of global gauge symmetry, associated with the condensate wavefunction itself [44, 45, 23]. This symmetry breaking occurs when the condensate's wavefunction assumes a definite value. As the condensate exists, its superfluid velocity, determined by its phase gradient [31], serves as the critical velocity in Landau's criterion for dissipationless flow [2, 31]. The behavior of the one-body density matrix $n(\mathbf{r}, \mathbf{r}') \to \rho_0$ for $|\mathbf{r} - \mathbf{r}'| \to \infty$ is termed as *off-diagonal long-range order* (ODLRO) [46], where the asymptotic value indicates the condensate fraction [46] of the occupation of the ground-state quantum wavefunction of the condensate [23]. In two-dimensional systems, for finite temperature, ODLRO is absent; however, for sufficiently small temperature, the one-body density matrix decays algebraically (quasi-long-range order). Only at $T = 0$ two-dimensional systems exhibit true ODLRO. Having established these key aspects, we now focus exclusively on two-dimensional systems.

Landau's criterion establishes the condition for dissipationless mass transport within the condensate at velocities below a critical threshold [47], with superfluidity characterized by the superfluid fraction. Intuitively, this fraction encompasses the lack of inertia that we would normally expect as a response to an applied velocity [10]: a force along direction α may produce a superfluid response along direction β, confirming that the superfluid fraction is intrinsically tensorial. In Monte Carlo simulations, it is typically calculated using the winding number of discretized paths [48], which reduces mathematically to the projected area swept by the path [49]. An alternative method computes the expectation value of the mechanical angular momentum [50], yielding well-defined maximum and minimum superfluid fraction values [51]. A third approach directly utilizes the phase of

the system's quantum wave function in a frame co-moving with velocity $\mathbf{v}$ (where distinct directions contribute independently), as implemented in Ref. [52]. Here, the phase gradient is integrated to compute the laboratory-frame total momentum, deriving the superfluid fraction tensor f_{ij}. For algorithmic details, see Appendix B; this is the method applied in our work.

Thus, a quantum system can condense and sustain a significant superfluid fraction. When density modulation coexists, a supersolid phase emerges – requiring simultaneous crystalline order and superfluidity in two-dimensional quantum systems. For instance, a two-dimensional system with an interparticle Gaussian potential has an isolant crystalline phase [7], Fig. 5, due to the absence of superfluidity in its crystalline phase. This work employed Monte Carlo simulations for a system with the Hamiltonian

$$\hat{H} = -\frac{\Lambda}{2}\sum_{i=1}^{N}\nabla_i^2 + \sum_{i<j}^{N}\exp\left[-\frac{1}{2}r_{ij}^2\right], \tag{1.1}$$

where Λ is the de Boer parameter, determining the quantum fluctuation, i.e., this parameter essentially compares the de Broglie wavelength of particles to the interparticle spacing [53][8], and a dimensionless interparticle distance $r_s \propto 1/\sqrt{\rho}$ is used, and, by varying the density density ρ and Λ, different phases could be achieved. As a result, this numerical investigation of the phase diagram for this soft-core system revealed two distinct phases: a simple crystalline (triangular) and a superfluid phase, the latter exhibiting reentrant behavior at high densities (small r_s), Fig. 5. Notably, neither cluster crystal nor supersolid phases were observed. This absence aligns with two key factors: (1) the positive-definite nature of the interaction potential in Fourier space, and (2) the cluster crystal stability conjecture proposed in Ref. [54], which conjectured that adding an attractive component to the interaction (making it non-positive definite in Fourier space) could allow the system to become supersolid.

[8] A large Λ indicates that quantum effects (like wave-like behavior) are significant. At the same time, a small Λ suggests that the classical behavior dominates.

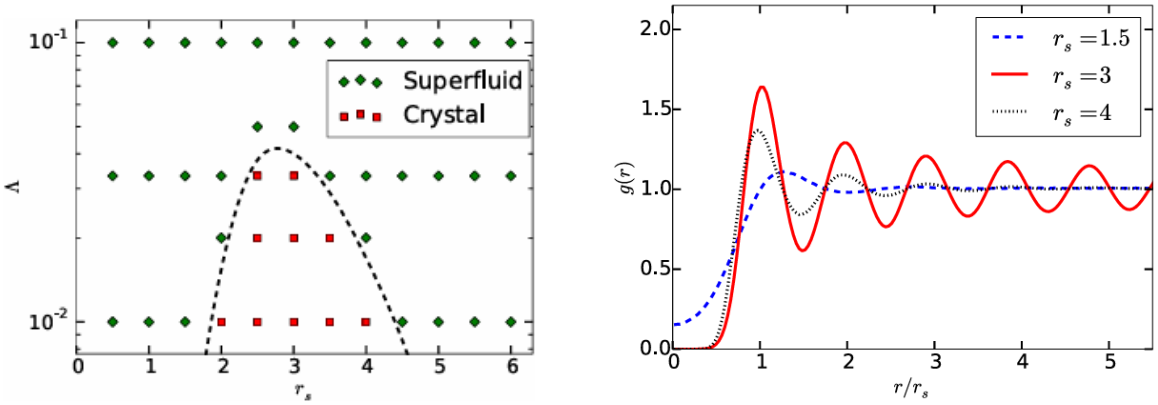

(a) (b)

Figure 5 – (a) The phase diagram at zero temperature of 2D GEM2. (b) At $\Lambda = 1/30$, the radial distribution function $g(r)$ assumes a periodic value for the $r_s = 3$, and for $r_s = 4$, the system re-enters the superfluid phase. Source: Kroiss et al. [7].

On the other hand, a simulation of another soft-core potential, this time with a $Q^{\pm}$-potential, Rydberg-dressed bosons showed a supersolid phase as follows. In this work, Cinti et al. [8] ran a path-integral Monte Carlo simulation of a two-dimensional quantum system whose Hamiltonian is

$$\hat{H} = -\sum_{i=1}^{N} \frac{\nabla_i^2}{2} + \sum_{i<j}^{N} \frac{U}{1+r^6}, \tag{1.2}$$

where U is the interaction strength, and a scaled density $R_c^2\rho$ is used because the spatial units are rescaled by the soft-core distance R_c. This time, as the Fourier transform of the potential has a negative part[9], a $Q^{\pm}$-potential. Thus, the interaction, even being soft-core, might pull in atoms closer, enabling clustering, and, most importantly, wave functions overlapping. This results in a non-zero superfluid fraction because atoms could be transported from one site to another, Fig. 6.

[9] The 2D Fourier transform of $v(r)$ writes [55]

$$\hat{v}(k) = \left(\frac{2\pi^2}{3}\right)\left(\frac{e^{-k/2}}{k}\right)(e^{-k/2} - 2\sin(\pi/6 - \sqrt{3}k/2)). \tag{1.3}$$

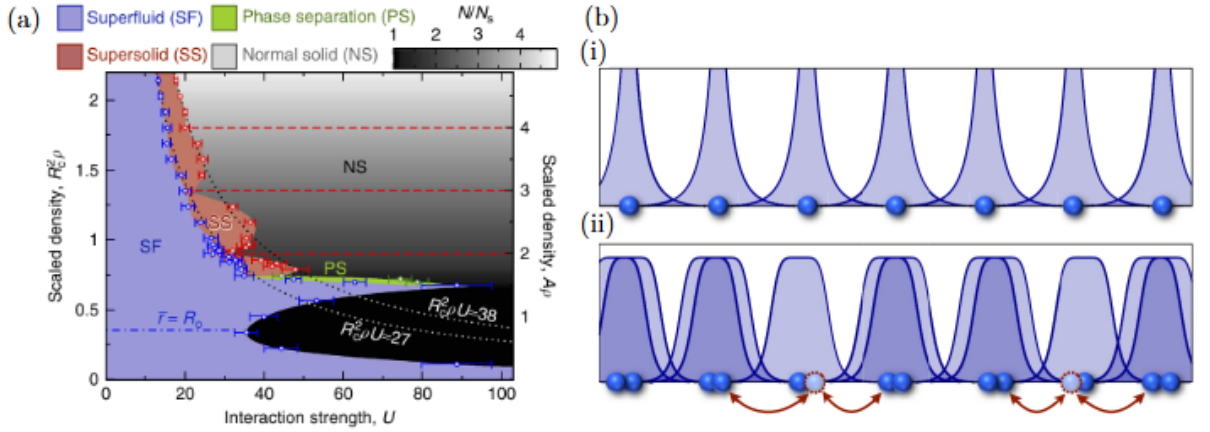

Figure 6 – (a) The phase diagram. (b) (i) For singular potentials characterized by pure power-law repulsion, as highlighted in blue, the particles organize into a commensurate, insulating crystalline phase. That would be the case for the GEM2 of Kroiss et al. [7]. (ii) Upon removal of the singularity, particle clustering becomes possible and, under suitable conditions, leads to the formation of an incommensurate crystal with a particle density exceeding the number of lattice sites. The delocalization of defects via inter-site tunneling can subsequently induce a finite superfluid response in the self-organized crystalline ground state. Source: Cinti et al. [8].

1.1 Dipolar Bose-Einstein condensates in quasi-two-dimensional systems

Alongside supersolids observed with Rydberg-dressed potentials, another companion platform of studying self-assembly systems at zero-temperature involves using dipolar Bose quantum gases[10] trapped in a plane (the dynamics is frozen along an axis by a trap potential), with interactions tuned via the Feshbach resonance[56, 57, 58, 59] [11].

Initially, associating the dipolar potential with soft-core potentials in two dimensions at $T = 0$ may seem problematic since the former diverges at the origin while the latter remains finite. The Fourier transform of the dipolar potential [60]

$$\tilde{U}(\mathbf{k}) = \frac{4\pi}{3}\left(3\frac{k_z^2}{\boldsymbol{k}^2 + k_z^2} - 1\right), \tag{1.4}$$

may also diverge as $(\boldsymbol{k}, k_z) \to \mathbf{0}$. However, by assuming a specific z-profile $\phi(z)$—such as a Thomas-Fermi or Gaussian profile, consistent with experimental confinement in opto-magnetic traps—the z-dependence integrates out during the convolution

$$\int d\mathbf{r}d\mathbf{r}' v(\mathbf{r} - \mathbf{r}')|\phi(\mathbf{r})|^2|\phi(\mathbf{r}')|^2. \tag{1.5}$$

[10] For more details on dipolar interaction, consult the Appendix A.

[11] The Feshbach resonance is $a(B) \propto 1 - \frac{\Delta}{B - B_0}$, where $a(B)$ is the dipole coupling parameter depends on the magnetic field B, and Δ is a resonance width[56, 58].

This yields an effective $Q^{\pm}$-class potential in the xy-plane, defining a ***quasi***-two-dimensional system. The resulting potential lacks divergence at the origin and decreases monotonically in $\boldsymbol{k}$, but unlike $Q^{\pm}$-class potentials, exhibits no minima. Nevertheless, similar to Rydberg systems, it may still promote crystal clustering. Consequently, pancake-shaped systems could host supersolid phases within inhomogeneous phases.

Experimentally, the realization of BECs with dipolar atoms has been reported [61, 62, 63, 64], and the supersolid phase has been observed in a modulated quasi-two-dimensional BEC of dysprosium atoms [65, 9], such as in Fig. 7, and, likewise, with clear evidence of superfluidity provided by the observation of quantum vortices [66] recently.

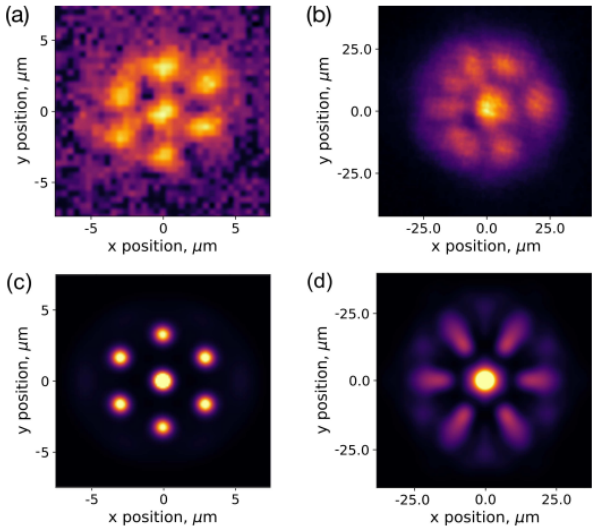

Figure 7 – Experimental realization of a dipolar modulated condensate. (a) Density profile. (b) State after 36 ms time-of-flight (TOF) expansion. A hexagonal modulation structure is explicitly observed. (c, d) Corresponding simulations for same trap, and with $N \approx 4.4 \times 10^4$ atoms within the droplets. Source: T. Bland et al. [9].

Supersolid phases in dipolar BECs remain an active research frontier. Both Gross-Pitaevskii equation solutions and variational approaches have been employed: Zhang et al. [67] applied variational methods to identify hexagonal and honeycomb phases, later extending this work to include stripe phases in Ref. [68]. Complementarily, Ripley et al. [10] solved numerically the Gross-Pitaevskii equation, also revealing three supersolid states – stripes, honeycomb, and hexagonal crystals (Fig. 8). Crucially, the stripe phase exhibits maximally anisotropic superfluidity: the superfluid fraction tensor reaches its maximum along the stripe direction while minimizing perpendicular to it (Fig. 8, phase diagram).

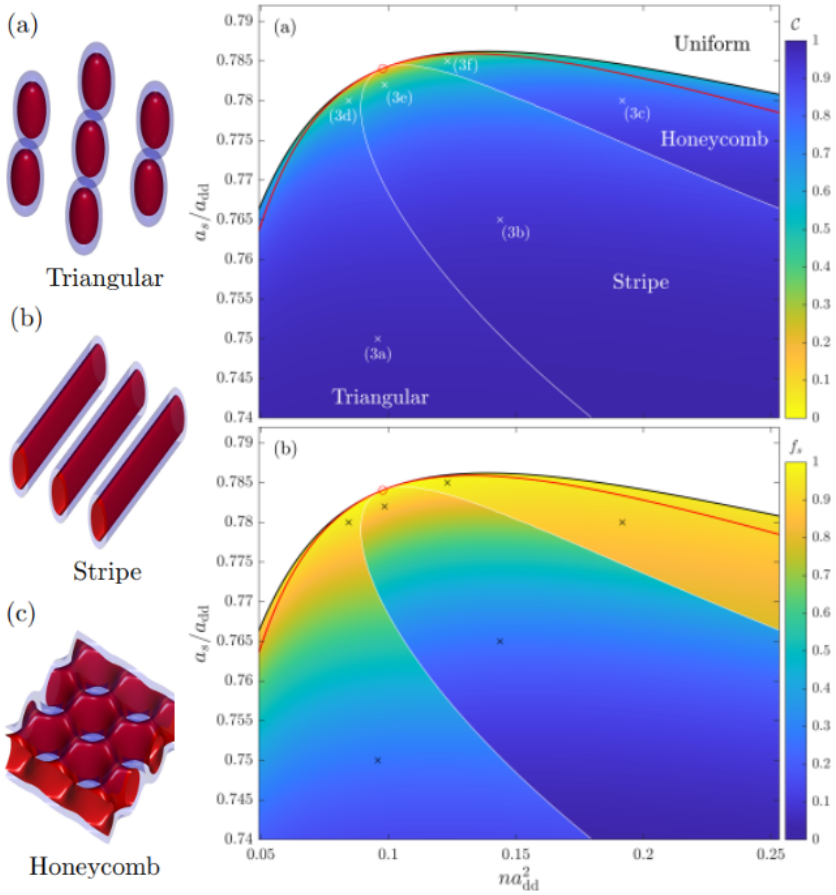

Figure 8 – At left, isosurfaces of probability of the condensate ground-state found when solving the GPE for different combinations of density and interaction parameters (a_{ss}/a_{dd}). At right, ground-state phase diagrams showing (a) the contrast C and (b) the superfluid fraction f_s. Source: Ripley et al.[10].

Interestingly, homogeneous phases of strictly 2D dipolar condensates were examined via hypernetted-chain equations (HNC) [69, 11]. This study revealed modulated instabilities in the homogeneous phase, strongly suggesting stripe-phase formation as the dominant instability pathway, as we can see in Fig. 9, in which the homogeneous instability of the static structure function occurs only in the k_y direction.

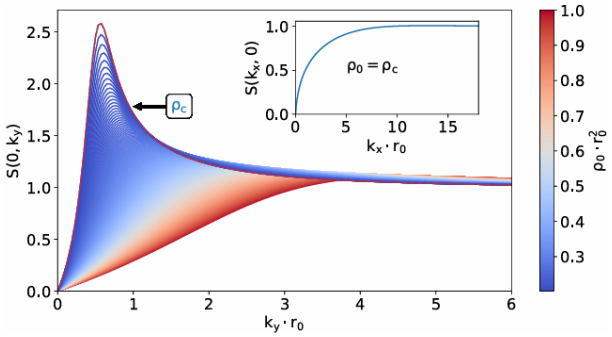

Figure 9 – Static structure factor $S(0, k_y)$ as a function of k_y. r_0 is a scaled length whose square normalizes the density (ρ_0) and wavevector in the y-direction k_y. As the density approaches a critical density, a large peak develops. $S(k_x, 0)$, shown in the inset, does not peak according to the variation of the density ρ_0. Source: Staudinger et al. [11].

Besides the variety of possible analyses, it was discovered that, in dipolar gases, the zero-point energy correction of Bogoliubov excitations, the Lee-Huang-Yang interaction [70], which adds beyond mean-field effects [71, 67, 72], have been theoretically proven essential for stabilizing quantum droplets [73, 74, 75]. For example, very recently, Adhikari et al. [76] showed that the inclusion of the Lee-Huang-Yang interaction further enriches the phase diagram by enabling metastable states such as multi-droplet solitons in strongly dipolar NaCs condensates (dipole strength $> 10\times$ Dy).

Dipolar supersolids also exhibit recurrent characteristics in different dimensions. Blakie et al. [12] studied a tube-dipolar system with confinement in the xy-plane, the dipoles oriented along the y-axis, and the axis of the tube oriented along the z-axis. This one-dimensional cigar-shaped dipolar condensate has first-order phase transitions: for low and high densities, discontinuous transitions take place between inhomogeneous and homogeneous phases [12], Fig. 10. For the two-dimensional case, under proper conditions (specifically, the new condition we are presenting here), this can be compared to the transitions between different modulated phases.

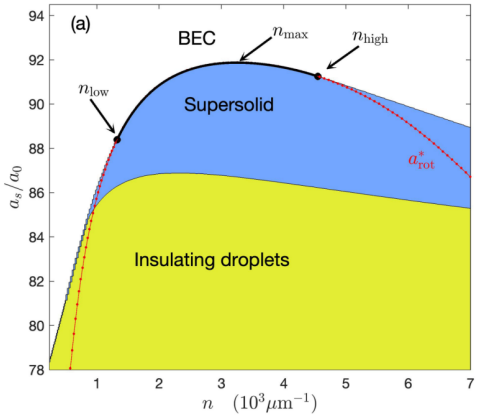

Figure 10 – Continuous transition for density $n \in [n_{\text{low}}, n_{\text{high}}]$, and the s-wave scattering length a_s in units of atomic Bohr length a_0. The dashed red line represents the roton instability of the uniform BEC. For values of density n out of the interval $[n_{\text{low}}, n_{\text{high}}]$, the system suddenly exhibits a modulated phase, which can be either a supersolid phase or insulating droplets. The sudden change from a homogeneous phase to a modulated phase is a first-order transition. Between the black continuous line, with n in the interval $[n_{\text{low}}, n_{\text{high}}]$, the system changes smoothly from a homogeneous phase to a modulated phase, i.e., it is a second-order phase transition. For more details on this work, see Ref. [12]. Author: Blakie et all[12].

As mentioned, Zhang et al. [68] computed the phase diagram for a single-component dipolar BEC, which consists of a hexagonal, stripe, and a honeycomb phase. This work is a chronological evolution from a previous, less evolved work on supersolids [67], in which they did not treat the stripe phase. Then, in another work on one- and two-component dipolar BECs, Zhang et al. [77] reported ring-lattice structures in two-dimensional dipolar bosons: these are metastable phases that consist of a mesh-up between triangular and honeycomb states.

In all these works on two-dimensional dipolar bosons mentioned, the dipolar polarization of the BEC is set along the z-axis, with no tilting angle relative to this axis, always perpendicular to the plane of the condensate. Also, in contrast to the cigar-shaped dipolar BEC, there is only one point of second-order phase transition, a triple point hexagonal-stripe-honeycomb phase at the boundary with the homogeneous phase, and the boundary between the homogeneous and the modulated phase is entirely a first-order transition.

1.2 Quasicrystals

In this section, we review key aspects of quasicrystals in bosonic condensates. First, we examine a foundational soft-matter classical system. Subsequently, we discuss its quantum counterpart. Finally, we identify critical research directions emerging from this

comparison.

We will have tailored special potentials in the reciprocal space according to a specific choice of the number of potential wells, the distance ratio among these wells, the pattern of how these potentials can be arranged, and their depth. These potentials decay to zero as k approaches infinity. For example, Barkan et al. [13] proposed a two-dimensional classical soft-matter system, whose interacting potential, the Lifshitz-Petrich-Gauss (LPG) potential, writes

$$\tilde{U}(k) = \exp\left(-\frac{k^2}{2\sigma^2}\right)(D_0 + D_2k^2 + D_4k^4 + D_6k^6 + D_8k^8), \tag{1.6}$$

whose Fourier transform in the real space has the same functional form

$$U(r) = \exp\left(-\frac{\sigma^2r^2}{2}\right)(C_0 + C_2r^2 + C_4r^4 + C_6r^6 + C_8r^8), \tag{1.7}$$

where C_i coefficients are linear functions of the coefficients D_i. The set of coefficients were chosen such that $U(0) = C_0 = 1$ and $\tilde{U}(1) = \tilde{U}(\tilde{k}_n)$ equal to some value less than 0.1. For example, the potential displayed in Fig.11 depicts different cases which lead to distinct geometric patterns.

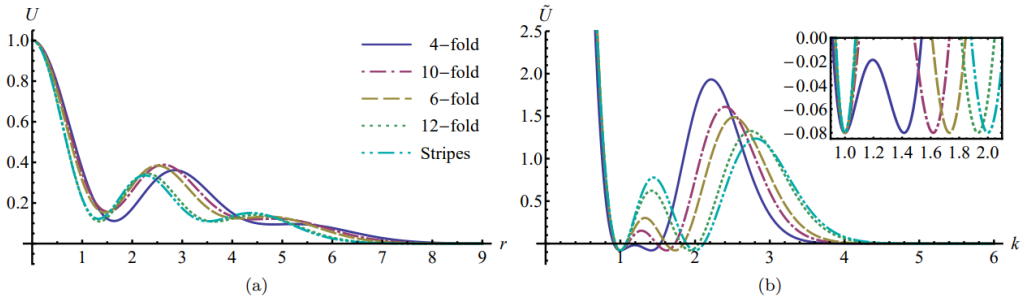

Figure 11 – a) Graph of the potential $U(r)$. b) In the Fourier transform $\tilde{U}(k)$, the first minimum consistently appears at $k = 1$, with subsequent minima at $k_4 = \sqrt{2}$ (blue), $k_5 = (1 + \sqrt{5})/2$ (red), $k_6 = \sqrt{3}$ (brown), $k_{12} = \sqrt{2 + \sqrt{3}}$ (green), and $k_\infty = 2$ (cyan). The inset magnifies these features. Each kind of potential (color) is associated to a different quasicrystal pattern. Source: Barkan et al. [13].

While the potentials are nearly indistinguishable in real space (Fig. 11(a)), making it difficult to predict their stabilized cluster crystals, they exhibit distinct features in reciprocal space (Fig. 11(b)) where the wavenumber ratio q, which is the ratio between the distance of the second well in relation to the first well, becomes apparent. This highlights an important constraint: any realistic potential must be carefully tuned in real space to achieve the required Fourier-space minima. The LPG potential, based on simultaneous instability at two length scales, leads to clusters of quasicrystals [78, 13]. The Fig. 12 displays particle distributions, as the radial distribution function $g(r)$ describes an angular

averaged distribution, providing a glimpse of the geometric pattern. The item Fig. 12(a) makes more visually explicit how the radial distribution behaves differently for each geometric pattern, as it is indicated by the diffraction diagrams.

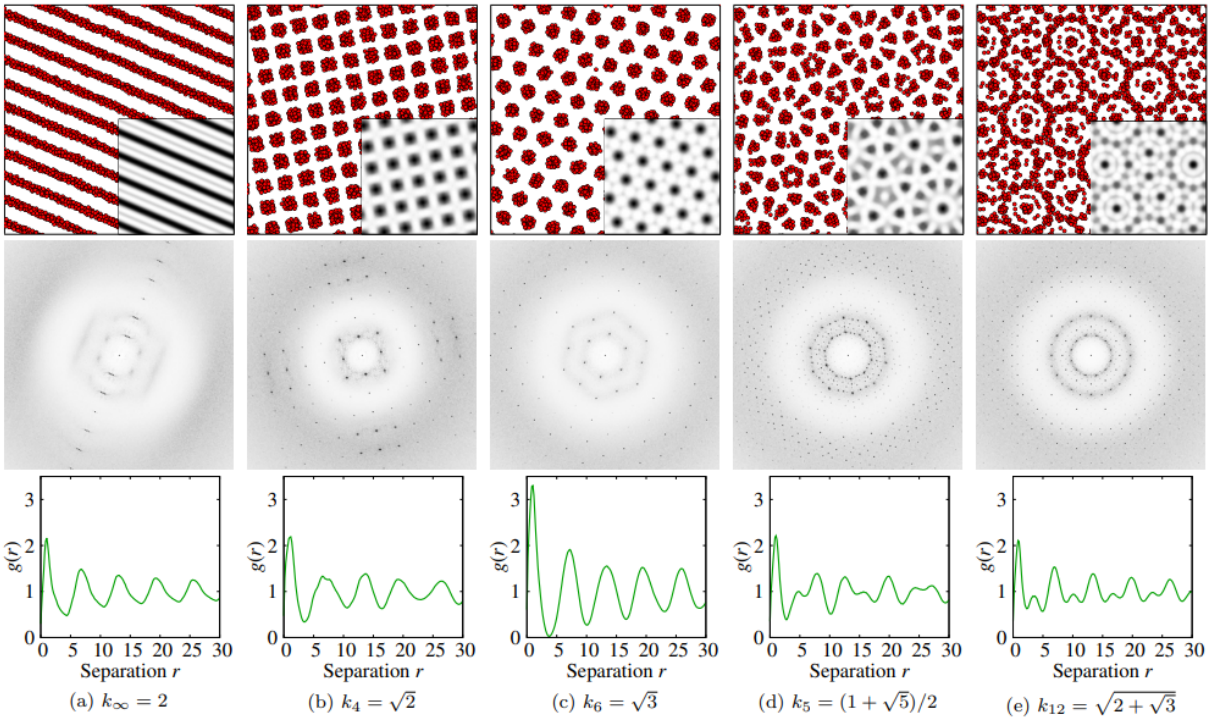

Figure 12 – Results from dynamics simulation (top), mean-field prediction (insets in grayscale), diffraction diagrams (middle), and radial distribution functions (bottom). For more details, consult the source of the Figure. (a) stripes, periodic (b) tetragonal and (c) hexagonal, as well as quasiperiodic (d) decagonal and (e) dodecagonal clusters. Source: Barkan et al.[13].

In two-dimensional bosonic condensates, it has been verified that Lifshitz-type potentials can also lead to quasicrystals. Pupillo et al. [14] implemented the Path-Integral Monte Carlo simulation of an ensemble of $N = 2^{13} = 8192$ particles of a system whose Hamiltonian is

$$\hat{H} = -\frac{\Lambda^2}{2}\sum_{i=1}^{N}\nabla_i^2 + \sum_{i<j}^{N} U(|\mathbf{r}_i - \mathbf{r}_j|), \tag{1.8}$$

where the authors guaranteed $V(|\mathbf{r}_i - \mathbf{r}_j|)$ to be equal to the one reported in Ref. [13] of the classical system simulation, Λ is the de Boer parameter [79, 80] which encodes the magnitude of quantum fluctuations. At finite temperature, this simulation found dodecagonal quasicrystals with finite superfluidity [14], and a phase diagram was also constructed which also contain a cluster solid and supersolid phases. Nonetheless, as the absolute-temperature goes to zero, the cluster solid phase is persistent, and the quasicrystal phase exists between a range of temperature above the zero-temperature, as it can be seen in the phase diagram, Fig. 13.

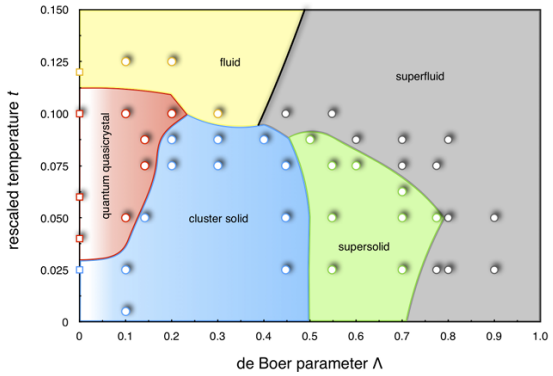

Figure 13 – Phase diagram constructed with multiple simulations of path-integral Monte Carlo simulation with $N = 8192$ particles. The thick black line denotes the Berezinskii-Kosterlitz-Thouless transition that separates the superfluid from the normal fluid. Note that at t_0 there is no quantum quasicrystal. Source: Pupillo et al. [14]

At zero temperature, Mendoza-Coto et al. [81] studied a two-dimensional system with a three-well Lifshitz potential, discovering a stable dodecagonal quasicrystalline lattice with finite superfluidity—a hallmark of supersolid-quasicrystal behavior. Their variational mean-field approach employed a Fourier-based ansatz, revealing 12-fold symmetric patterns with persistent superfluid properties. The work further established a comprehensive phase diagram (Fig. 14), demonstrating the coexistence of quasiperiodic order and superfluidity.

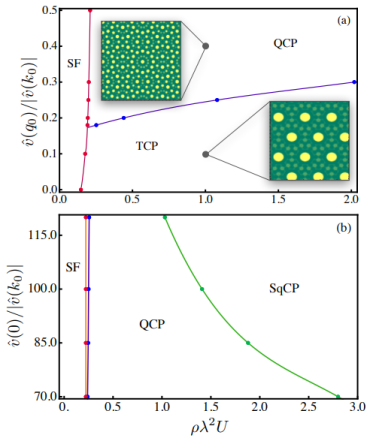

Figure 14 – Phase diagrams composed of superfluid (SF) phase, QCP, TCP, and SqCP stand for 12-fold quasicrystal phase, triangular crystal phase, and square crystal phase, respectively. Vertical axis is a normalized depth of the Fourier transform potential $\hat{v}(k)$ at the origin (bottom inset), and at a secondary minimum at q_0 (top inset). Horizontal axis is the scaled density $\rho\lambda^2$ times the potential intensity U. Source: Mendoza-Coto et al. [15].

While the Lifshitz potential provides a convenient mathematical framework for studying quasicrystal formation, it has no confirmed experimental realization so far. Meanwhile, optical-cavity platforms have emerged as promising experimental tools for producing effective interactions that stabilize modulated phases in ultracold gases [82,

83, 84, 85, 68, 86]. In such experiments, a mirror array confines light to create cavity modes with selected resonances. Repeated bouncing of light within the cavity mediates interactions between particles via photons supplied by an external pump [85]. Such systems provide exceptional control over the form and spatial extent of interactions, making them ideal for exploring quantum many-particle behavior.

Advances in high-finesse optical cavities have recently enabled the design of photon-mediated forces that act as fully programmable effective interactions between ultracold particles, allowing one to tune their sign, spatial profile, and interaction range [16], as sketched in the experimental setup of Fig. 15. A Bose–Einstein condensate is positioned along the z-axis of an optical cavity with resonance frequency ω_c and photon decay rate κ. Inside the cavity, atoms interact with the electromagnetic mode through a position-dependent Rabi coupling $g(z) = g_0 \cos(2\pi z/\lambda_c)$, where g_0 is the maximum coupling strength and $\lambda_c = 2\pi c/\omega_c$ sets the wavelength of the cavity mode. A condensate of longitudinal length L is irradiated by a narrow laser beam with waist $w \ll L$ and local frequency $\Omega(\mathbf{r}, t)$; the beam is dynamically swept over the sample along a trajectory $\boldsymbol{r}_0(t)$, in a raster pattern whose horizontal passes are spaced by l [16]. For a laser operating at frequency ω_L, detunings from the atomic and cavity resonances are defined as $\Delta_a = \omega_L - \omega_a$ and $\Delta_c = \omega_L - \omega_c$, respectively, where ω_a denotes the natural atomic transition frequency. In this configuration, two atoms interact via an effective cavity-photon-mediated potential [87, 16] that can be expressed as

$$v(\boldsymbol{r}, \boldsymbol{r}') = g\delta(\boldsymbol{r} - \boldsymbol{r}') + \frac{2\Delta_c g_0^2}{\Delta_a^2(\kappa^2 + \Delta_c^2)} \overline{\Omega(\boldsymbol{r}, t)\Omega(\boldsymbol{r}', t)} \tag{1.9}$$

where g is the contact interaction strength between atoms and the time average of the laser scanning over one period is

$$\overline{\Omega(\boldsymbol{r}, t)\Omega(\boldsymbol{r}', t)} = \frac{1}{T}\int_0^T dt \Omega(\boldsymbol{r}(t) - \boldsymbol{r}_0(t))\Omega(\boldsymbol{r}'(t) - \boldsymbol{r}_0(t)) \tag{1.10}$$

being v the scanning velocity, and the period $T = L^2/lv$. The temporal average 1.10 can then be written as

$$\overline{\Omega(\boldsymbol{r}, t)\Omega(\boldsymbol{r}', t)} = \frac{1}{T}\sum_{y_n}\int_0^T dt \Omega(\boldsymbol{r}(t) - \boldsymbol{r}_0(t))\Omega(\boldsymbol{r}'(t) - \boldsymbol{r}_0(t)) \tag{1.11}$$

where the trajectory of each scanning line follows $\boldsymbol{r}_0(t) = (x(t), y) = (vt, y_n)$, with $y_n = nl$ for $n = 1, 2, \cdots, L/l$. We extended each horizontal line integral to $\pm\infty$, justified by the laser's finite range which ensures the integrand vanishes sufficiently far from both $\boldsymbol{r}$ and $\boldsymbol{r}'$. From Eq. 1.11, we convert the time integral to a spatial integration over x. Moreover, when the line spacing l is smaller than the laser's characteristic width w ($l < w$), the discrete sum over n becomes expressible as a continuous integral over y, yielding:

$$\overline{\Omega(\boldsymbol{r}, t)\Omega(\boldsymbol{r}', t)} = \frac{1}{L^2}\int_{-\infty}^{\infty} dy \int_{-\infty}^{\infty} dx \Omega(\boldsymbol{r} - (x, y))\Omega(\boldsymbol{r}' - (x, y)). \tag{1.12}$$

We now implement the coordinate transformation $(x, y) \to \boldsymbol{r}' + (x, y)$. Exploiting the laser profile's radial symmetry $\Omega(\boldsymbol{r}) = \Omega(-\boldsymbol{r})$, we obtain:

$$\overline{\Omega(\boldsymbol{r}, t)\Omega(\boldsymbol{r}', t)} = \frac{1}{L^2}\int_{-\infty}^{\infty} dy \int_{-\infty}^{\infty} dx \Omega(\boldsymbol{r} - \boldsymbol{r}' - (x, y))\Omega((x, y)) = \frac{1}{L^2}(\Omega * \Omega)(\boldsymbol{r} - \boldsymbol{r}'). \tag{1.13}$$

The time-averaging process constitutes a spatial convolution dependent solely on distance. Within this framework, the laser profile decomposes as $\Omega(\boldsymbol{r}) = \Omega_0(\boldsymbol{r})h(\boldsymbol{r})$, where Ω_0 denotes the laser intensity and $h(\boldsymbol{r})$ represents a dimensionless spatial form factor. Following Eq. 1.13, the pair interaction potential 1.9 becomes

$$v(\boldsymbol{r}, \boldsymbol{r}') = g\delta(\boldsymbol{r} - \boldsymbol{r}') + \frac{2\Delta_c g_0^2}{\Delta_a^2(\kappa^2 + \Delta_c^2)}\frac{\Omega_0^2}{L^2}(h * h)(\boldsymbol{r} - \boldsymbol{r}'), \tag{1.14}$$

with Fourier transform

$$\hat{v}(q) = g - \nu_0 \hat{h}^2(q), \tag{1.15}$$

where

$$\nu_0 = \frac{2\Delta_c g_0^2}{\Delta_a^2(\kappa^2 + \Delta_c^2)}\frac{\Omega_0^2}{L^2}. \tag{1.16}$$

Current experimental capabilities [16, 85] enable nearly unconstrained implementation of such interaction potentials. In the context, the parameter g is introduced as a constraint, such that the admissible values of the function characterizing the laser intensity profile do not exceed the magnitude of the pairwise contact interaction. To model $\hat{h}^2(q)$, in our work "*Engineering interaction potentials for stabilizing quantum quasicrystal phases*", we employ Gaussian basis functions, because we consider as a flexible approach enabling precise control over reciprocal-space potential minima positions and depths. This tunability facilitates systematic investigation of competing length scales governing spontaneous pattern formation. Building on the methodology of Mendoza-Coto et al. [15], we implement a variational mean-field treatment of the energy density functional to systematically investigate quantum condensate ground states.

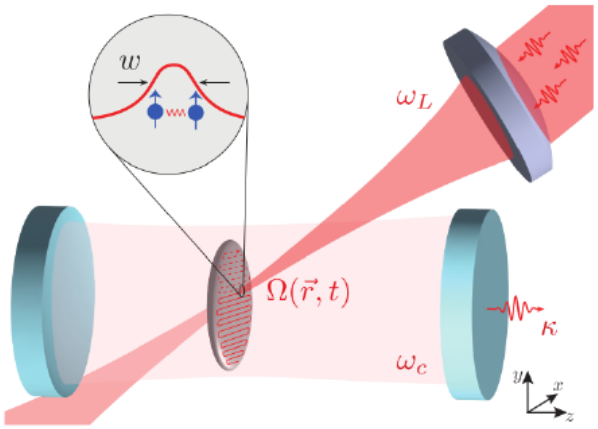

Figure 15 – The experimental configuration couples a BEC (gray) to an optical cavity mode (light red confined between blue mirrors) with resonant frequency ω_c, where the BEC is confined in a plane perpendicular to the cavity axis. A scanning laser with mode function $\Omega(\boldsymbol{r}, t)$ and frequency ω_L periodically illuminates the sample along horizontal lines, while photons escaping at rate κ enable real-time monitoring. The magnified region highlights the microscopic mechanism: only atoms within the laser's transverse field interact via photon exchange. This local process, determined by the laser profile $\Omega(\boldsymbol{r}, t)$, yields an effective many-body interaction potential after time averaging across the entire system [16]. Source: Bonifacio et al. [16].

1.3 Open questions

In summary, recent studies of dipolar bosonic systems polarized perpendicular to a planar geometry [67, 10, 77, 88, 89] have identified three modulated ground-state phases: a low-density hexagonal solid, an intermediate-density stripe phase, and a high-density honeycomb lattice. Transitions between these phases have been described as continuous transitions of second-order, converging to a critical point in the thermodynamic limit characterized by the meeting point of three inhomogeneous phases [68]. This observation contrasts with soft-core bosonic supersolids, where first-order transitions dominate between homogeneous and modulated phases [90, 91, 55, 92]. The potential for a continuous supersolid-superfluid transition in 2D systems could simplify experimental realization by reducing metastability [9].

The fundamental question is whether continuous transitions between distinct phases represent universal behaviour. How would an eventual tilting of the trap potential relative to the z-axis affect this phenomenon? Could first-order transition lines emerge? While a Ginzburg-Landau approach describes second-order transitions, its domain of validity requires careful examination. Additionally, how would such tilting affect superfluidity? Analogous to cigar-shaped dipolar BECs, the second transition might only exist within a specific density range. Would critical points between stripe, honeycomb, and hexagonal phases persist under variable tilting angles? How would the phase diagram change? Our

work *Supersolid dipolar phases in planar geometry* addresses these questions.

Regarding quasicrystals, quantum soft matter systems exhibit phases with quasiperiodic long-range order displaying dodecagonal symmetry [14, 15], governed by two or three characteristic length scales. Concurrently, the variational approach (which is significantly less computationally intensive than dynamical simulations of a quantum system) of the Ref. [15] revealed 12−fold symmetry quasicrystals using a novel triple-well potential of Lifshitz's type [15]. This raises two key questions: (1) How does the number of potential wells influence emergent symmetries? If two competing length scales might drive a quasicrystal, what about three or more? And what about varying their depth? (2) How does the depth ratio between wells modify the phase behaviour? Could novel symmetries (e.g., octagonal) emerge? These questions and more form the basis of *Engineering interaction potentials for stabilizing quantum quasicrystal phases.*

2 Publication: *Supersolid dipolar phases in planar geometry: effects of tilted polarization*

Supersolid dipolar phases in planar geometry: effects of tilted polarization

Daniel Lima,[1,*] Matheus Grossklags,[1,†] Vinicius Zampronio,[2,‡] Fabio Cinti,[2,3,4,§] and Alejandro Mendoza-Coto[1,2,¶]

[1] *Departamento de Física, Universidade Federal de Santa Catarina, 88040-900 Florianópolis, Brazil*
[2] *Dipartimento di Fisica e Astronomia, Università di Firenze, I-50019, Sesto Fiorentino (FI), Italy*
[3] *INFN, Sezione di Firenze, I-50019, Sesto Fiorentino (FI), Italy*
[4] *Department of Physics, University of Johannesburg, P.O. Box 524, Auckland Park 2006, South Africa*

The behavior of dipolar Bose-Einstein condensates in planar geometries is investigated, focusing on the effects of the polarization orientation. While perpendicular polarization produces a phase diagram with hexagonal, stripes, and honeycomb phases ending at a single critical point, the presence of an in-plane polarization component transforms the critical point into three critical lines, separating two phases at a time and changing radically the appearance of the phase diagram. All transition lines contain first- and second-order regions, while the phase diagram itself shows a resemblance with those displayed by quasi-one-dimensional dipolar systems. Finally, we investigate the effect of introducing an in-plane polarization on the structural properties of the phases and determine the superfluid fraction. Our results show that this process induces an axial deformation on the hexagonal and honeycomb phases, resulting in an anisotropic behavior in the long distance properties of the system like superfluidity. We expect that the rich phenomenology observed provides motivation for new experiments and theoretical works.

I. INTRODUCTION

The study of patterns with unconventional symmetries such as stripes phases [1–4], smectic liquid crystals [5–7], cluster crystals [8–13], and quasicrystals [14–19], has become a central topic of modern many-body physics. These systems reveal a variety of phenomena over different physics fields, including soft matter [20, 21], superconductivity [22, 23], cavity QED systems [24], and long-range interacting systems [25]. Ultracold atomic systems have emerged as an ideal platform [26] to investigate such exotic states of matter, thanks to their unprecedented controllability and tunability [27]. In particular, dipolar Bose-Einstein condensates (BECs), characterized by long-range dipole-dipole interactions, have proven to be a quite versatile system in this context [25, 28–30]. Recent experiments have demonstrated the formation of quantum droplets and supersolids [28, 31, 32]. In many cases, the existence of such states can be seen as a macroscopic manifestation of quantum fluctuations [33], since these effects stabilize phases that would otherwise undergo collapse due to the presence of attractive interactions [34–36].

In the case of supersolids, a phase that simultaneously displays discrete translational symmetry and superfluidity [37, 38], initial experimental studies focused on quasi-one-dimensional systems, where density modulations are induced along an elongated trap [39]. However, recent breakthroughs have enabled the realization of two-dimensional supersolids [40, 41], producing new structural transitions and a large variety of crystalline phases. Theoretical investigations [42–47] have predicted complex phase diagrams that include hexagonal, stripes and honeycomb configurations, with phase transitions governed by density and interaction parameters [48, 49]. Notably, the emergence of metastable states, such as ring-lattice patterns, highlights the intricate competition between different symmetries and interactions [44].

Recently, a series of works [43, 44, 49–51] have addressed in detail the study of the ground-state phase diagram of a Bose dipolar gas in planar geometry when the system is polarized perpendicular to its plane. Those works have shown that, in such conditions, the system develops three modulated phases: a hexagonal solid at low densities; a stripes phase at intermediate densities; and a honeycomb phase at high densities. The transition between these phases is always first order, except at the critical point of the system in which all phase boundaries converge. The existence of this critical point in the thermodynamic limit is particularly interesting considering that soft-core bosonic supersolid phases usually display a first-order transition between the homogeneous and the modulated phases [52–55]. Moreover, from the experimental point of view, the existence of a continuous supersolid-superfluid transition could facilitate the production of the 2D supersolid phase [41], since typically metastable states are produced when the system is driven from the superfluid to the supersolid phase.

In this work, we study the effects of arbitrary polarization orientation for a dipolar boson system in planar geometry. Our results show that when the polarization vector exhibits a component along the system's plane, the critical point predicted for the case of perpendicular polarization evolves into multiple critical lines. As an example, in Fig. 1(a), we show the phase diagram obtained for a tilting angle $\alpha = 30°$. We were able to identify three different modulated phases according to the den-

* daniel.s.lima@posgrad.ufsc.br
† matheus.grossklags@posgrad.ufsc.br
‡ vinicius.zamproniopedroso@unifi.it
§ fabio.cinti@unifi.it
¶ alejandro.mendoza@ufsc.br

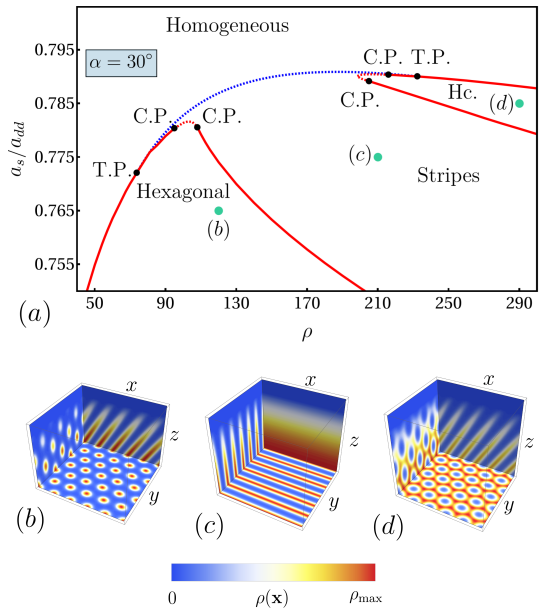

Figure 1. Phase diagram and modulated phases developed by a dipolar planar bosonic gas for a polarization orientation $\alpha = 30°$, with respect to the normal direction to the plane of the system. In (a), we present the phase diagram of the system at a fixed polarization orientation varying the average density of particles ρ and the ratio a_s/a_{dd}. In (b-d) we show slice density plots of the 3D density patterns exhibited by the system in the modulated phases identified. The areal average density of particles is measured along the plane perpendicular to the polarization vector.

sity pattern in the xy-plane of the system: a compressed hexagonal lattice, a stripes phase, and a stretched honeycomb phase (see Fig. 1(b-d)). As can be observed, the topology of the phase diagram obtained differs significantly from the one known for perpendicular polarization, displaying some similarities with the phase diagram of quasi-one-dimensional cigar-shaped dipolar systems. Indeed, as can be observed, the system presents a wide intermediate density region in which the transition from the one-dimensional modulated pattern (stripes) to the homogeneous superfluid phase is second order. Moreover, we investigate how the polarization orientation impacts the structural properties of the ground-state phases and the superfluid fraction.

This paper is organized as follows: Sec. II introduces the microscopic model and outlines the theoretical framework used to describe the modulated phases of a BEC in planar geometry with tilted polarization. Sec. III is dedicated to presenting the evolution of the phase diagram of the single-mode system as the tilting polarization angle is varied. Furthermore, Sec. IV focuses on the study of the properties of the system using fully converged spectral expansions. Here, we present a comparison with single-mode results and investigate in detail the structural properties of the system as well as the impact of the tilted polarization on the superfluid properties. Finally, Sec. V delivers an ending discussion and concluding remarks.

II. MODEL AND METHODS

We consider a three-dimensional system of N identical dipolar bosons with mass m at zero temperature, confined along the z-direction by a harmonic trap with potential $U(\boldsymbol{x}) = \omega^2 z^2/2$, where ω corresponds to the frequency of the trap (see Fig. 1). The particles interact through collisions, modeled as a zero-range interaction with scattering length a_s as well as through a non-local dipolar interaction, characterized by a scattering length a_{dd}. Moreover, we consider that the magnetic moment of all particles is polarized along the direction $(\sin(\alpha), 0, \cos(\alpha))$, i.e., forming an angle α with the trapping direction. For simplicity in the mathematical description, we work in a rotated coordinate system of the form $x' = x\cos(\alpha) - z\sin(\alpha)$, $y' = y$ and $z' = z\cos(\alpha) + x\sin(\alpha)$. In this new coordinate system, the polarization direction coincides with the z'-axis, the central plane of the system is given by $z' = \tan(\alpha)\, x'$ and the trapping potential is written as $U(\boldsymbol{x}') = \frac{1}{2}\omega^2 \left(z'\cos(\alpha) - x'\sin(\alpha)\right)^2$. To avoid cumbersome notation, from now on we will omit the prime symbol in our calculations to refer to the new coordinate system. Taking as units of length $\delta l = 12\pi a_{dd}$ and time $\delta t = m\delta l^2/\hbar$, respectively, the mean-field energy per particle functional can be expressed as

$$\frac{E}{N} = \int d\boldsymbol{r} \left\{ \frac{1}{2}|\boldsymbol{\nabla}\psi|^2 + U(x,z)\,|\psi|^2 + \frac{2}{5}N^{3/2}\gamma|\psi|^5 + N\frac{a_s}{6a_{dd}}|\psi|^4 + \frac{N}{8\pi}\int d\boldsymbol{r}' V(\boldsymbol{r}-\boldsymbol{r}')\,|\psi(\boldsymbol{r})|^2|\psi(\boldsymbol{r}')|^2 \right\}, \tag{1}$$

where the Lee-Huang-Yang (LHY) [33] coefficient can be written as $\gamma = \frac{4}{3\pi^2}\left(a_s/(3a_{dd})\right)^{5/2}\left[1 + \frac{3}{2}(a_{dd}/a_s)^2\right]$ [56–58]. Finally, the dipole-dipole interaction potential $V(\boldsymbol{r})$ for a system polarized along the z-direction is given by

$$V(\boldsymbol{r}) = \frac{1}{r^3}\left(1 - \frac{3z^2}{r^2}\right). \tag{2}$$

The ground-state phase diagram of the model in the thermodynamic limit can be accessed by minimizing the energy per particle functional subject to the constraint $\int d\boldsymbol{r}|\psi(\boldsymbol{r})|^2 = 1$. Here, the integration domain extends over the region $[0, L_x] \times [0, L_y]$, such that $L_x \times L_y \to \infty$ while $z \in (-\infty, +\infty)$. Moreover, the number of particles in the system is given by $N = \rho L_x L_y$, where ρ stands for the areal density of particles along the xy-plane perpendicular to polarization direction [59].

In agreement with the scenario in which the magnetization is oriented perpendicular to the plane of the system

($\alpha = 0$), we consider a ground-state wave function of the form

$$\psi(\boldsymbol{r}) = \frac{1}{\sqrt{A}}\phi(x,y)\,\chi(z_\perp(x,z)), \tag{3}$$

where $A = L_x L_y$ stands for the area of the system, $z_\perp = z\cos(\alpha) - x\sin(\alpha)$, and $\chi^2(z_\perp(x,z))$ describes the localized density profile produced by the confining potential $U(z_\perp(x,z))$ on the transversal direction (see Fig. 1). Without generality loss, we replace the normalization condition for $\psi(\boldsymbol{x})$ by the following two independent normalization conditions for $\chi(z_\perp)$ and $\phi(x,y)$, $\int dz\chi^2(z_\perp(x,z)) = 1$ and $\int_A dxdy|\phi(x,y)|^2 = A$. In analogy with previous works [43, 48], we consider that $\chi^2(z_\perp)$ follows a Thomas-Fermi profile of the form

$$\chi^2(z_\perp) = \frac{3\cos(\alpha)}{4\sigma}\left(1 - \frac{z_\perp^2}{\sigma^2}\right)\Theta(\sigma - |z_\perp|), \tag{4}$$

where σ represents the width of the system to be determined variationally and $\Theta(u)$ stands for the Heaviside step function. Replacing the proposed ansatz for $\psi(\boldsymbol{x})$ in Eq. (1), we obtain that the energy per particle of the system can be rewritten as

$$\begin{aligned}\frac{E}{N} = \int \frac{d\boldsymbol{r}}{A}\Bigg\{&\frac{1}{2}|\boldsymbol{\nabla}\phi(\boldsymbol{r})|^2 + \frac{\omega^2\sigma^2}{10}\\ &+\frac{9\sqrt{3}\pi}{256}\frac{\gamma(\rho\cos(\alpha))^{3/2}}{\sigma^{3/2}}|\phi(\boldsymbol{r})|^5 + \frac{\rho\cos(\alpha)}{10\sigma}\frac{a_s}{a_{dd}}|\phi(\boldsymbol{r})|^4\\ &+\frac{\rho\cos(\alpha)}{2\sigma}\int d\boldsymbol{r}' V_{\text{eff}}(\boldsymbol{r}-\boldsymbol{r}')|\phi(\boldsymbol{r})|^2|\phi(\boldsymbol{r}')|^2\Bigg\},\end{aligned} \tag{5}$$

where $\boldsymbol{r}$ stands for the vector position in the xy-plane and the effective potential $V_{\text{eff}}(\boldsymbol{r})$ is defined by its form in momentum space $\hat{V}_{\text{eff}}(\boldsymbol{k}) = 2/5 - F(k_x\sigma/\cos(\alpha), k_y\sigma/\cos(\alpha), \alpha)$ where

$$\begin{aligned}F(q_x,q_y,\alpha) = \int_{-\infty}^{\infty}\frac{dq}{2\pi}&\left(\frac{3(-q\cos(q)+\sin(q))}{q^3}\right)^2\\ &\times\frac{q_y^2 + (q_x - q\tan(\alpha))^2}{q_y^2 + q^2 + (q_x - q\tan(\alpha))^2}.\end{aligned} \tag{6}$$

It is worth mentioning that in Eq. (5) the kinetic energy contribution along the z-direction has been neglected as usual within the Thomas-Fermi approximation. This procedure has been validated by previous works reporting similar results with or without such an approximation [43, 48].

Now that the energy per particle functional for the 2D effective problem associated with the configurations of $\phi(\boldsymbol{r})$ have been constructed, the ground-state properties of the system, including its phase diagram, can be determined from the direct minimization of such functional. With this goal, we consider three different kinds of possible solutions: a homogeneous state, a stripes configuration along the x-axis, and a 2D solution with hexagonal symmetry that can be stretched or compressed along the x-axis as well. The x-axis, in our case, coincides with the direction of the in-plane polarization of the system.

A. Homogeneous state

In the case of the homogeneous state we have $\phi_{\text{h}}(\boldsymbol{r}) = 1$, resulting in an energy per particle of the form

$$\begin{aligned}\frac{E_{\text{h}}}{N} =&\frac{\omega^2\sigma^2}{10} + \frac{9\sqrt{3}\pi}{256}\frac{\gamma(\rho\cos(\alpha))^{3/2}}{\sigma^{3/2}} + \frac{\rho\cos(\alpha)}{10\sigma}\frac{a_s}{a_{dd}}\\ &+\frac{\rho\cos(\alpha)}{5\sigma}\left(1 - \frac{3}{2}\sin^2(\alpha)\right).\end{aligned} \tag{7}$$

The properties of this phase are then obtained after the minimization of E_{h}/N with respect to the single parameter σ. Moreover, we verified that the value of σ for all the modulated solutions that will be presented shortly does not differ significantly from its corresponding value for the homogeneous solution. For this reason, to simplify the numerical evaluation, we will approximate the value of σ in those cases by the corresponding value obtained for the homogeneous solution.

B. Stripes state

In this case, we consider that the ground-state wave function takes the form

$$\phi_{\text{st}}(\boldsymbol{r}) = \frac{1 + \sum_{n\geq 1} c_n\cos(nk_0 y)}{1 + \frac{1}{2}\sum_{n\geq 1} c_n^2}, \tag{8}$$

where the set of coefficients c_n's are taken as variational parameters as well as the wave vector of the modulation k_0. The normalization factor introduced in the denominator of the right-hand side of Eq. (8) is required to guarantee the normalization condition previously mentioned for $\phi(\boldsymbol{r})$. An important aspect to be noticed is that we have explicitly considered that the stripes are oriented along the in-plane component of the polarization vector, which in our case coincides with the x-axis. This alignment is produced by the attractive component of the dipolar interaction that creates an anisotropy minimizing the energy in such configuration.

C. Hexagonal solid and honeycomb states

In analogy with the results obtained for dipolar gases confined in a planar geometry, we also consider compressed or stretched solutions with hexagonal symmetry of the form

$$\phi_{\text{hx}}(\boldsymbol{r}) = \frac{1 + \frac{1}{2}\sum_{m,n}{}' c_{m,n}\cos(k_0\boldsymbol{e}_{mn}\cdot\boldsymbol{r})}{1 + \frac{1}{4}\sum_{m,n}{}' c_{m,n}^2}, \tag{9}$$

where $\boldsymbol{e}_{mn} = m\boldsymbol{e}_1 + n\boldsymbol{e}_2$, with $\boldsymbol{e}_1 = (0,1)$ and $\boldsymbol{e}_2 = (1/2\cot(\theta), -1/2)$ and m and n integers. The prime on top of the sum symbol excludes the case $(m,n) = (0,0)$. The form of the selected basis $\{\boldsymbol{e}_1, \boldsymbol{e}_2\}$ is general enough to allow simultaneously homogeneous axial deformations of the hexagonal pattern along the x-axis and to recover continuously the energy functional corresponding to the fully symmetric hexagonal pattern, when we have $\alpha = 0$ and $\theta = \pi/6$. It is worth noticing that a solution with $\theta < (>)\ \pi/6$ corresponds to a hexagonal pattern compressed (stretched) along the x-axis. Moreover, to preserve the symmetries of these patterns under axial deformations along the x-direction, the variational coefficients $c_{m,n}$'s are set to be equal when they correspond to equivalent wave vectors $k_0\boldsymbol{e}_{mn}$ by inversion and reflection symmetries with respect to the x and y axes. It is important to mention that in this case, besides the variational parameters $c_{m,n}$'s, the characteristic wave vector k_0 and the parameter θ are determined from the minimization of the energy per particle in Eq. (5) evaluated for the ansatz in Eq. (9). Finally, it should be noticed that since the hexagonal solid (honeycomb) phase is identified as a triangular lattice of clusters (voids) of particles, the dominant Fourier amplitudes $c_{1,0}$ and $c_{0,1}$ which corresponds to the lowest non zero wave vectors of the pattern, will be both positive (negative). In general, given that both solutions could simultaneously exist as metastable states, it is important to consider these two possibilities as initial conditions in the energy minimization process, in addition to the stripes and homogeneous states, when selecting the actual ground-state of the system for a certain set of parameters.

D. Variational method

The substitution of the wave function ansätze for the homogeneous, stripes and axially deformed hexagonal or honeycomb solution into the energy per particle functional in Eq. (5) allow us to obtain closed analytical expressions for the energy of these phases in terms of the variational parameters c's, the characteristic wave vector k_0, θ and σ. Hence the global minimum of these energy functions, resulting from the minimization respect to the variational parameters, correspond to the energy of each corresponding phase. Naturally, the ground-state of the system is identified as the solution providing the lowest energy value.

The numerical minimization of the energy function for each ansatz is performed using the Wolfram Mathematica platform. We employed an interior point minimization method, setting 12 to 16 working precision digits, and a precision and accuracy goal of 10 to 16 digits. The accurate determination of the variational energies is key for the determination of smooth phase boundaries since the relative energy difference between the various solutions can be rather small. See appendix A for further details of the variational method and related approximations employed.

The main advantage of the spectral method described over standard finite difference methods is related to the fact that, unless we go deep into the modulated regions of the phase diagram, the number of relevant Fourier amplitudes is usually quite limited, improving significantly the computational cost of the variational problem.

E. Superfluid tensor

As discussed in literature [49, 60], the superfluid fraction tensor for a supersolid of mass M can be defined from the reduction of its translational inertia when we consider that the system is confined by moving walls. Thus, the superfluid tensor is defined as

$$f_s^{ij} = \delta_{ij} - \lim_{v\to 0} \frac{1}{M}\frac{\partial P_i}{\partial v_j}, \quad i,j = \{x,y\} \tag{10}$$

where v_j stands for the j-component of the moving walls and P_i represents the equilibrium momentum of the system. Considering the problem of the equilibrium state of the system with such boundary conditions, it is possible to conclude that the superfluid fraction tensor can be operationally computed as [60–62]

$$f_s^{ij} = \delta_{ij} - \int \frac{d\boldsymbol{r}}{A}|\phi(\boldsymbol{r})|^2 \frac{\partial K_i}{\partial r_j}, \tag{11}$$

where the auxiliary functions $K_x(\boldsymbol{r})$ and $K_y(\boldsymbol{r})$ satisfies respectively the equations

$$\boldsymbol{\nabla}\cdot(\rho(\boldsymbol{r})\boldsymbol{\nabla}K_i(\boldsymbol{r})) = \frac{\partial\rho(\boldsymbol{r})}{\partial r_i}, \tag{12}$$

where $\rho(\boldsymbol{r}) = |\phi(x\cos(\alpha), y)|^2$. This expression for $\rho(\boldsymbol{r})$ corresponds to the probability density along the central plane of our system, which is the one to be considered if we want to study its planar-superfluid properties.

To proceed, instead of directly solving the problem posed by Eq. (12), we took a different route to determine $K_{x,y}(\boldsymbol{r})$. Our approach is based on recognizing that Eq. (12) corresponds to the Euler-Lagrange equation of the action

$$S[K_i(\boldsymbol{r})] = \int \frac{d\boldsymbol{r}}{A}\left(K_i(\boldsymbol{r})\frac{\partial\rho(\boldsymbol{r})}{\partial r_i} + \frac{\rho(\boldsymbol{r})}{2}(\boldsymbol{\nabla}K_i(\boldsymbol{r}))^2\right). \tag{13}$$

It is not difficult to realize that the above functional for $i = \{x,y\}$ is convex, hence the solutions of Eq. (12) correspond to their respective global minimum. We should notice that since the density profile has the generic form $\rho(\boldsymbol{r}) = \sum_{m,n} b_{m,n}\cos(k_0\boldsymbol{e}_{mn}\cdot\boldsymbol{r})$, we have

$$\frac{\partial\rho(\boldsymbol{r})}{\partial r_i} = -\sum_{m,n} k_0 b_{m,n}\sin(k_0\boldsymbol{e}_{mn}\cdot\boldsymbol{r})\, e_{mn}^{(i)}, \tag{14}$$

where $e_{mn}^{(i)}$ stands for the i-component of $\boldsymbol{e}_{mn}$. This means that $\partial\rho(\boldsymbol{r})/\partial x_i$ is an odd function, satisfying $\partial\rho(-\boldsymbol{r})/\partial x_i = -\partial\rho(\boldsymbol{r})/\partial x_i$.

Moreover, the most general solution that can be constructed for $K_i(\boldsymbol{r})$ which is consistent with the periodicity of the corresponding density pattern $\rho(\boldsymbol{r})$ has the form

$$K_i(\boldsymbol{r}) = \sum_{m,n} a^{(i)}_{m,n} \sin(k_0 \boldsymbol{e}_{mn} \cdot \boldsymbol{r}) + \sum_{m,n} b^{(i)}_{m,n} \cos(k_0 \boldsymbol{e}_{mn} \cdot \boldsymbol{r}). \tag{15}$$

We can notice here that the expansion containing the cosine (sine) terms corresponds to an even (odd) component of $K_i(\boldsymbol{r})$, named hereafter as $K_i^+(\boldsymbol{r})$ $\left(K_i^-(\boldsymbol{r})\right)$. As expected, the even (odd) component of $K_i(\boldsymbol{r})$ satisfy $K_i^{+(-)}(-\boldsymbol{r}) = +(-) K_i^{+(-)}(\boldsymbol{r})$. Replacing $K_i(\boldsymbol{r}) = K_i^+(\boldsymbol{r}) + K_i^-(\boldsymbol{r})$ into Eq. (13) and taking into account the parity of $\partial\rho(\boldsymbol{r})/\partial x_i$ and $K_i^{\pm}(\boldsymbol{r})$, we can conclude that

$$S[K_i(\boldsymbol{r})] = \int \frac{d\boldsymbol{r}}{A} \left(K_i^-(\boldsymbol{r}) \frac{\partial\rho(\boldsymbol{r})}{\partial r_i} + \frac{\rho(\boldsymbol{r})}{2} \left(\boldsymbol{\nabla} K_i^-(\boldsymbol{r})\right)^2 + \frac{\rho(\boldsymbol{r})}{2} \left(\boldsymbol{\nabla} K_i^+(\boldsymbol{r})\right)^2 \right). \tag{16}$$

The functional $S[K_i(\boldsymbol{r})]$ in Eq. (16) is written as the sum of two independent contributions, each depending solely on $K_i^+(\boldsymbol{r})$ and $K_i^-(\boldsymbol{r})$, respectively. The first contribution is given by $S_1\left[K_i^+\right] = \int d\boldsymbol{r}/A\ \rho(\boldsymbol{r}) \left(\boldsymbol{\nabla} K_i^+(\boldsymbol{r})\right)^2/2$, while the second takes the form $S_2\left[K_i^-\right] = \int d\boldsymbol{r}/A \left(K_i^-(\boldsymbol{r})\, \partial_i\rho(\boldsymbol{r}) + \rho(\boldsymbol{r}) (\boldsymbol{\nabla} K_i^-(\boldsymbol{r}))^2/2\right)$. As a result, the absolute minimum of $S[K_i]$ can be determined through the independent minimizations of $S_1\left[K_i^+\right]$ and $S_2\left[K_i^-\right]$. It is possible to notice that since $\rho(\boldsymbol{r})$ is strictly positive, the absolute minimum of $S_1[K_i^+]$ is zero, and is achieved when $K_i^+(\boldsymbol{r})$ is a constant. Given that the superfluid fraction tensor f_s^{ij}, computed via Eq. (11), depends only on the spatial derivatives of $K_i(\boldsymbol{r})$ and not on its overall value, we are free to set this constant to zero without altering the resulting f_s^{ij}. As a consequence, all Fourier coefficients $b^{(i)}_{m,n}$ are zero and hence we have

$$K_i(\boldsymbol{r}) = K_i^-(\boldsymbol{r}) = \sum_{m,n} a^{(i)}_{m,n} \sin(k_0 \boldsymbol{e}_{mn} \cdot \boldsymbol{r}), \tag{17}$$

where $\boldsymbol{r} = (x\cos(\alpha), y)$ and $\boldsymbol{e}_{mn}$ is defined as in Eq. (9). Inserting the ansatz for $K_i(\boldsymbol{r})$ and the ground-state probability density $\rho(\boldsymbol{r})$ in Eq. (13) allows us to obtain upon integration a closed expression for the action, $S[\{a^{(i)}_{m,n}\}]$, in terms of the Fourier amplitudes $\{a^{(i)}_{m,n}\}$. The minimization of such many-variables functions allow us to determine the Fourier amplitudes $\{a^{(i)}_{m,n}\}$ of the expansion of $K_i(\boldsymbol{r})$ and naturally provides a direct route to calculate the components of the superfluid fraction tensor. The main advantage of the method proposed resides in the fact that in most cases a quite limited number of Fourier amplitudes are needed to achieve convergence in the expansions of $K_{x,y}(\boldsymbol{r})$, speeding up significantly the numerical evaluation of the superfluid properties of the system from the knowledge of the ground-state wave function.

III. SINGLE-MODE RESULTS

Upon minimization of the energy per particle functions for the different kinds of solutions considered, the ground-state phase diagram of the system can be constructed in the density ρ and a_s/a_{dd} plane, for a fixed polarization orientation α. Here it is worth to remember that the case $\alpha = 0$ corresponds to the scenario where polarization is normal to the plane of the system. To understand the main effects of tilting the polarization vector, we firstly focus on the study of the critical regime of the modulated phases. In this regime, the modulation amplitude is expected to be small and consequently among all the Fourier modes in the expansion of $\phi(\boldsymbol{r})$, those corresponding to the zero and the lowest non-zero Fourier wave vectors dominates the solution. Hence, considering ground-state ansätze of this form and following the variational method outlined in Sec. II D, we are able to calculate the phase diagram of the system within the single-mode approximation.

In Fig. 2, we present a sequence of phase diagrams varying the polarization tilting angle α for a frequency trap $\omega = 0.08$. As can be observed in Fig. 2(a), the resulting phase diagram for the case in which the polarization is perpendicular to the plane of the sample agrees with previous works [48, 49]. In this case, the system displays homogeneous, hexagonal, honeycomb and stripes phases converging all at a single critical point (C.P.), firstly reported by Zhang et al. [48] and improved posteriorly upon inclusion of the stripes phase [44, 49]. Interestingly, as shown in Fig. 2(b-f), when the polarization vector is tilted with respect to the plane of the system ($\alpha > 0$), the critical point at $\alpha = 0$ turns into three second order critical lines – plotted as dashed lines in Fig. 2 – which ends at critical points. Beyond the critical points, the phase boundaries correspond to first order phase transitions, which in Fig. 2 are presented with full lines. Second and first order phase boundaries are identified by monitoring the behavior of the characteristic Fourier mode serving as order parameter for each kind of phase. In our case, these parameters are selected as $c_{0,1}$ for the hexagonal and honeycomb phases and c_1 for the stripes phase, see Sec. II B and Sec. II C. As expected, we classify a transition as second order when the corresponding order parameter goes continuously to zero at the phase boundary and first order when it remains finite at the transition. Hence, C.P.'s mark those places over the phase boundary where the first order phase boundary turns continuously into second order.

For $\alpha > 0$, we identify the same kind of phases observed for $\alpha = 0$, the main geometrical difference is the development of an uniaxial anisotropy producing the compression of the hexagonal pattern ($\theta < \pi/6$) and the stretch-

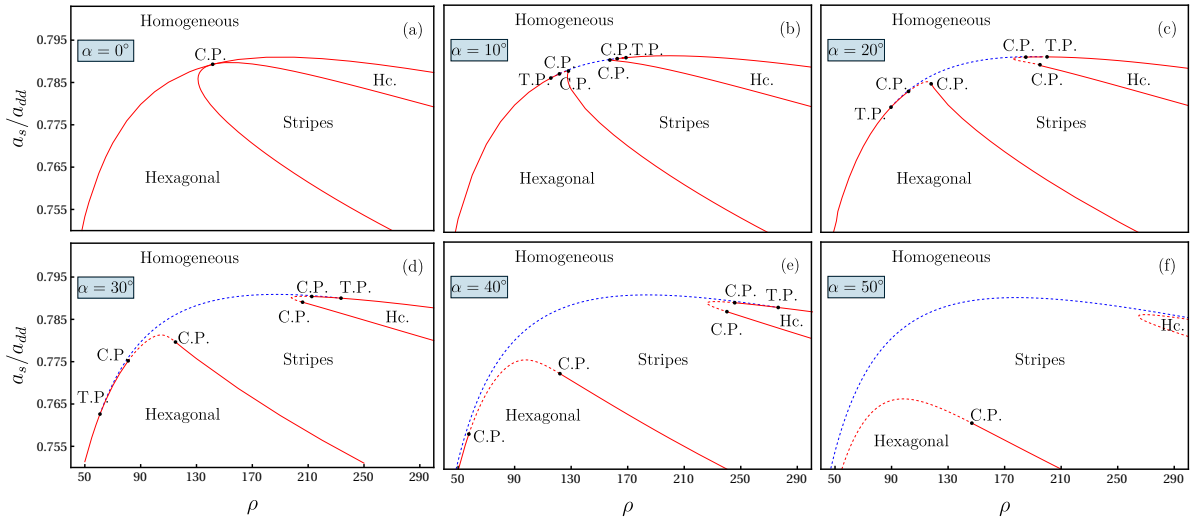

Figure 2. Ground-state phase diagrams for a fixed trap frequency $\omega = 0.08$ for different values of the tilting angle α. Four distinct phases are observed: a homogeneous phase, a hexagonal compressed phase, a honeycomb stretched (Hc.) phase, and a stripes phase. Dashed lines correspond to continuous transition, while full lines correspond to first-order transitions between these phases. The acronyms C.P. and T.P. stand for critical point and triple point, respectively.

ing of the honeycomb structure ($\theta > \pi/6$) along the x-axis. The sequence of phase diagrams clearly shows the crossover process in which the critical lines continuously decrease their extension until they converge to a single critical point at $\alpha \to 0$. On the other hand, as the tilting angle α is increased, the extension of the second order critical lines grows as well as the stability region of the stripes phase. This makes the stripes phase the dominant modulated phase for large values of α. Moreover, for $\alpha > 0$, two different triple points (T.P.) are developed in the system, one at low densities where the hexagonal, stripes, and homogeneous phases meet and another at high densities where the honeycomb, stripes and homogeneous phases converge.

A natural question one might ask at this point is how general the results obtained within the single-mode approximation are. The single-mode study presented here and in many previous works [39, 43, 44, 48] do not seek numerical accuracy in the description of the phase diagram, but to capture qualitatively its main features. One of the main messages of the present work is to show that a tilted polarization creates an anisotropy in the planar configuration that turns the $\alpha = 0$ critical point into three independent critical lines for $\alpha > 0$. Interestingly, it is possible to present an analytical argument (see appendix B) based on the single-mode approximation explaining the origin of this behavior. The reason is ultimately related to the presence of the axial anisotropy which changes the rotational symmetry of the hexagonal-like patterns from six- to two-fold producing a Ginzburg-Landau (G.L.) expansion for the energy per particle containing only even powers of the characteristic Fourier amplitude of the hexagonal pattern. This property of the Ginzburg–Landau expansion, together with the presence of two independent control parameters in our case, ρ and a_s/a_{dd}, accounts for the emergence of critical lines in the phase diagram, in contrast to the behavior observed for $\alpha = 0$.

IV. MANY-MODES RESULTS

Now, we explore the effects of higher-order Fourier modes on the ground-state wave function. To this end, we allowed a large enough Fourier basis to achieve a fully converged solution. We choose arbitrarily the cases $\alpha = 30°$ and $\alpha = 50°$ to compare the many-modes and the single-mode phase diagrams. As can be observed in Fig. 3, the presence of the secondary modes does not alter the stripes-homogeneous critical line (blue dashed). This occurs because higher-order harmonics in the stripes solution become sub-leading at this phase boundary, turning the single-mode approximation exact in this region. Meanwhile, the critical lines corresponding to the continuous transitions from compressed hexagonal to stripes phase and from stretched honeycomb to stripes phase – represented with dashed red lines in Fig. 3 – are weakly affected by the higher-order harmonics for $\alpha = 30°$ and more strongly for $\alpha = 50°$. This behavior arise because these phase boundaries are located inside the bulk of the stripes phase where the stripes solution always contain higher-order harmonics, thus affecting the position of the critical line when higher-order harmonics are included.

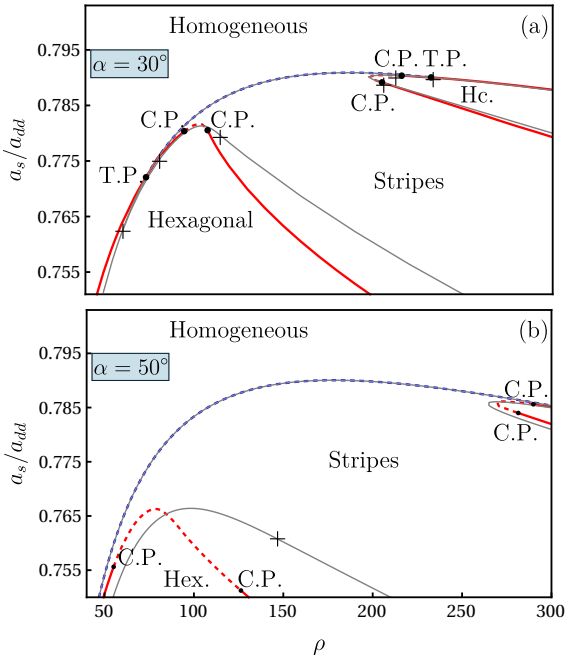

Figure 3. Comparison between the many-modes phase diagram and the single-mode phase diagram for a tilting angle $\alpha = 30°$ and a trap frequency $\omega = 0.08$. Red and blue lines correspond to the many-modes calculation, while gray lines correspond to the single-mode case already presented in Fig. 2. The notation employed to name phases and characteristic points is the same followed in Fig. 2. Dots (crosses) mark the limits of the critical lines and triple points for the many-modes (single-mode) case.

Despite the quantitative differences between the single and the many-modes phase diagrams, a comparison between Fig. 2 and Fig. 3 confirms the main qualitative predictions of our single-mode study regarding the development of critical lines, critical and triple points for $\alpha > 0$, as well as the growth of these critical lines and the stripe phase as the tilting angle α is increased. It is worth to notice the stability enhancement of the stripes phase when considering the many-modes ansatz. This behavior is somewhat expected since this is the kind of modulated solution most affected by the single-mode approximation, while the hexagonal solution contains two independent variational Fourier amplitudes, at this level of approximation, the stripes solution contains only one.

Now we turn our attention to the impact on the structural properties of tilting the polarization of the system. As already mentioned in Sec. III, the phases with hexagonal symmetry for $\alpha = 0$ are deformed when $\alpha > 0$. In general, the presence of a tilted polarization with respect to the plane of the system creates an additional effective attractive dipolar interaction between the clusters of particles in the direction of the in-plane polarization. This leads to a compression of the hexagonal solid phase and a stretching of the lattice of voids in the honeycomb phase along the x-direction. This effect can be measured by the ratio between the distance to the next nearest clusters (voids) along the x-direction (D_x) and along the diagonal direction (D_d). It is not hard to show that given the ansatz for $\phi_{\rm hx}(\boldsymbol{r})$, we have that $D_x/D_d = 2\sin(\theta)$. Here D_x and D_d are measured between the center of clusters (voids) and on a plane perpendicular to the polarization vector, which sets the 3D filaments orientation.

In Fig. 4(a-b) and Fig. 4(d-e) we show two examples of the probability density patterns $\phi^2(\boldsymbol{r})$ for two different points in the $(\rho, a_s/a_{dd})$ plane for $\alpha = 30°$, the definition of D_x and D_d as well as the behavior of the corresponding ratio D_x/D_d varying α. We can observe that, for the example values considered, the deformation of the hexagonal phase is much greater than the one experienced by the honeycomb phase as the polarization tilting angle α is increased. This seems to be reflecting a higher resistance to deformations of the honeycomb in comparison with the hexagonal pattern. Such deformations of the solutions not only affect the geometric features of the density pattern but, more interestingly, they impact the superfluid properties of the system.

As discussed in literature, long wavelength properties in a system with hexagonal symmetry are typically isotropic, this occurs for instance with the elastic response and also occurs with the superfluid fraction tensor [60, 63]. In this sense, a natural check of the technique employed to compute the superfluid fraction tensor is to recover the same values for f_s^{xx} and f_s^{yy} for the hexagonally symmetric configurations obtained when $\alpha = 0$. As can be observed in Fig. 4(c) and Fig. 4(f), the superfluid tensor components along the x and y directions are indeed equal for perpendicular polarization ($\alpha = 0$). Moreover, the off-diagonal components of the superfluid fraction tensor remain zero for all α's. A natural result, since both hexagonally symmetric patterns and stripes patterns have zero off-diagonal components when the configuration is symmetric against reflections with respect to the x and y axes. To complement our discussion of the superfluid properties we simultaneously present in Fig. 4(c) and Fig. 4(f) the contrast of the corresponding modulated phases, defined as

$$C = \frac{\mathrm{Max}\left(|\psi|^2\right) - \mathrm{Min}\left(|\psi|^2\right)}{\mathrm{Max}\left(|\psi|^2\right) + \mathrm{Min}\left(|\psi|^2\right)}. \tag{18}$$

The results show that as the polarization develops a component along the x-direction ($\alpha > 0$) the superfluid fraction along this direction (f_s^{xx}) grows steadily while the y component decreases as long as we remain within the hexagonal and honeycomb phases. In the case of the hexagonal phase, this is a response to the tendency of the system of approximate clusters along the x-direction and make them further apart in the other directions when α is increased. Interestingly, despite the significant variation of the superfluid properties, the contrast of the modulated phases does not display a significant variation along

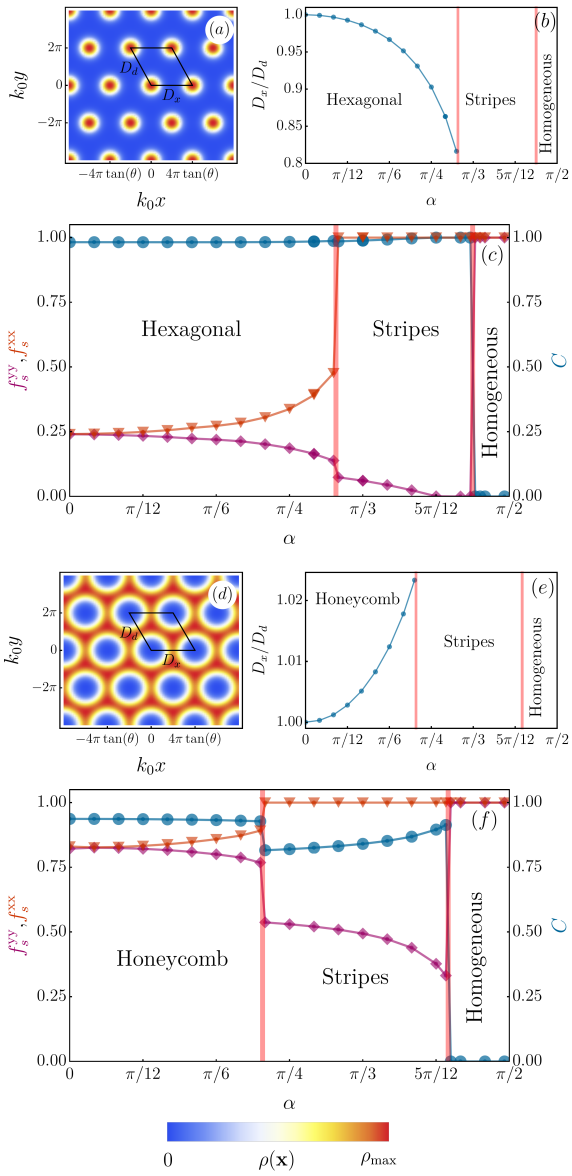

Figure 4. Variation of structural properties with the tilting angle α for the points $(120, 0.755)$ (a-c) and $(350, 0.779)$ (d-f) in the $(\rho, a_s/a_{dd})$ plane. Figs. (a) and (d) present the density profiles for $\alpha = 30°$. Figs. (b) and (e) show the evolution of the ratio D_x/D_d for the two examples considered. Finally, Figs. (c) and (f) presents the evolution increasing α of the superfluid fraction tensor components f_s^{xx} (orange triangles) and f_s^{yy} (purple diamonds) as well as the contrast (C) (blue circles) for the two example points considered. The pink stripe localizing the transition between modulated phases in (c) and (f) has a width equal to 1°.

this process.

In the case of the honeycomb phase, a smaller anisotropy between f_s^{xx} and f_s^{yy} is observed when compared with the hexagonal case. In this scenario, the leading mechanism for the variation of the superfluidity as α is increased does not seem to be related to the deformation of the honeycomb lattice since it remains at small values over the whole phase (see Fig. 4(e)). The variation of the superfluidity with α in this case is produced by a process of particle redistribution in which the regions linking maximum density points along the x-direction in a "zig-zag" trajectory (see Fig. 4(d)) gets more homogeneous and wider, while regions linking maxima along the y-direction becomes more localized.

Within the stripes region we have $f_s^{xx}(\alpha) = 1$, while $f_s^{yy}(\alpha)$ develops a decreasing behavior with α (see Fig. 4(c) and (f)). This behavior is produced by an increase of the attraction between particles in a given stripe as in plane polarization component is increased, which promotes particle localization along the y-axis and hinders superfluidity between stripes. At the same time, as α is increased the variational condensate width σ decreases (see Fig. 5(b)) which decreases the dipolar repulsion of the homogeneous configuration up to a point in which a transition to the homogeneous state becomes favorable. We verified that this a strong first order transition as the stripes configuration is metaestable in the vicinity of the phase boundary with the homogeneous state.

V. FINAL DISCUSSION

In the last few years, a surge of interest in the possible impacts of topological ingredients on Bose-Einstein condensation has emerged as a hot topic in the search for exotic phases in the field of ultracold quantum gases. Different authors have considered bubble, torus, cylinder among other possible geometries to study how different configurations produce non-trivial condensate properties and modulated phases [13, 64–67]. In this sense, we consider in the present work a relatively simple setup that has remained unexplored so far [28–30], a planar polarized dipolar Bose gas with tilted polarization with respect to the plane of the system. Our results show that tilting the polarization orientation has a major impact on the quantum critical behavior of the system when compared with the already known case with perpendicular polarization. In this case, as the polarization angle departs from the normal direction the isolated quantum critical point present at $\alpha = 0$ breaks into three critical lines separating two phases at a time. Besides changing the critical behavior, a tilted polarization also produces structural changes in the modulated phases, mainly in the hexagonal and honeycomb phases, which develop axially anisotropic properties. In this respect, we obtain that this axial anisotropy induced by the in-plane polarization favors superfluidity along this direction and hinders it in the orthogonal direction. This result offers an interesting avenue to manipulate the superfluid properties

of hexagonal and honeycomb dipolar supersolids, which otherwise ($\alpha = 0$) present an isotropic behavior.

On another subject, it is important to remark that despite the existence of significant literature exploring the physics of strictly 2D dipolar systems with tilted polarization, the physical behavior of the analog quasi-2D systems is radically different and significantly under researched. Only recently the ground-state phase diagram of quasi-2D dipolar systems with perpendicular polarization was established [49], and the effects of the tilted polarization concerning the plane of the system remain unexplored until now.

We conclude by discussing the important aspect of the experimental realizations. The regime of parameters used for analytical calculations is compatible with current experimental capabilities [28, 32, 68–70]. A potential experiment using ^{162}Dy would allow a wide range of s-wave scattering lengths a_s. Considering the dipolar length $a_{dd} \approx 7\,\mathrm{nm}$, we will have a range of a_s/a_{dd} consistent with the values considered in this work. For ^{162}Dy, the characteristic units of length and time will be $\ell = 0.26\,\mu\mathrm{m}$ and $t_0 = 0.18\,\mathrm{ms}$. Hence, a trapping dimensionless frequency $\omega_z\, t_0 = 0.08$ is equivalent to $\omega_z \approx 450\,\mathrm{Hz}$. As an example, let us consider the configuration presented in Fig. 4(a) corresponding to $a_s/a_{dd} = 0.755$, $\rho = 120$ and $\alpha = 30°$, in this case, we will have $\sigma \approx 6.78\,\mu\mathrm{m}$ and a peak 3D density along the middle plane of the system $3\rho/4\sigma \approx 1.9 \times 10^{14}\,\mathrm{cm}^{-3}$. For these conditions, the ground-state characteristic wave vector of the compressed hexagonal solid is $k_0 \approx 0.4$, which results in a lattice spacing $D_x = 4\pi \tan(\theta)/k_0 \approx 4.59\,\mu\mathrm{m}$ and $D_d = 2\pi \sec(\theta)/k_0 \approx 4.75\,\mu\mathrm{m}$, i.e., a sufficiently small value that allows studying long-distance physical properties experimentally.

ACKNOWLEDGMENTS

A.M.C. acknowledge UNIFI for financial support and hospitality. A.M.C., D.L., and M.G. acknowledge the Fundação de Amparo à Pesquisa de Santa Catarina, Brazil (Fapesc), and Coordenação de Aperfeiçoamento de Pessoal de Nível Superior - Brasil (CAPES) - Finance Code 001. Fapesc, CAPES, and CNPq supported this work. F. C. and V. Z. acknowledge financial support from PNRR MUR Project No. PE0000023-NQSTI.

Appendix A: Variational procedure details

To illustrate how the variational method is applied in this work, Fig. 5(a) shows an example of the behavior of the energy difference of the modulated solutions with respect to the homogeneous state for $\omega = 0.08$, $\alpha = 0$ and $a_s/a_{dd} = 0.780$ as the density (ρ) is varied. As expected, the phase boundaries are located at the crossing points of the energy curves, and the phases are identified by the regions in which each curve presents the lowest values among all of them.

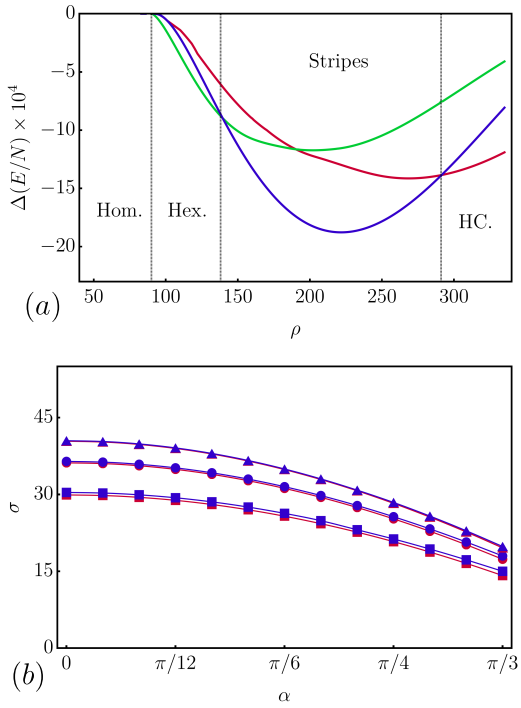

Figure 5. Variational behaviour of the energy per particle and condensate width for a trap frequency $\omega = 0.08$. Fig. (a) corresponds to the energy per particle difference of the modulated and homogeneous solutions as the density ρ is varied for $a_s/a_{dd} = 0.78$ and $\alpha = 0$. The green, blue, and red curves correspond to the hexagonal solid, stripe,s and honeycomb solutions. Fig. (b) shows the behavior of the condensate width σ as a function of the tilting angle for the homogeneous solution (red curve) and for the relevant modulated solution (blue curve). The square, circle and triangle symbols corresponds to $(\rho, a_s/a_{dd})$ values equal to $(120, 0.765)$, $(210, 0.775)$ and $(290, 0.785)$, respectively.

One additional feature of the variational method employed in this work is related to the treatment given to the variable associated to the condensate width σ. In general, for weak to moderate modulations, the variational width of the condensate for non-homogeneous solutions is expected to be very close to that of the homogeneous phase for the same set of parameters. As an example, in Fig. 5(b) we present a comparison between the value of this parameter determined variationally for the relevant modulated solution and for the homogeneous phase for the points (b), (c), and (d) in the phase diagram depicted in Fig. 1. The proximity between the curves $\sigma(\alpha)$ for the homogeneous and modulated solutions at low and moderate values of the tilting angle confirms the validity of the discussed approximation. However, we should note that the decreasing behavior of the width of

the condensate as the tilting angle is increased produces a progressive increment of the relative difference of the condensate width for the homogeneous and modulated solutions that ultimately, limits the validity of this approximation to low and moderate tilting angles.

In this way, for the more extensive part of our computations, which corresponds to the construction of phase diagrams at low and moderate values of α (see Fig. 1, Fig. 2 and Fig. 3), we make use of the approximation discussed above for the variational parameter σ. Conversely, for the phase diagrams exploring the large α behavior of the system presented in Fig. 4, the condensate width σ is considered a variational parameter for the modulated phases as well.

Appendix B: Ginsburg-Landau theory for Hexagonal to Stripes transition

The nature of the hexagonal to stripes phase transitions can be studied formally using a Ginzburg-Landau (G.L.) approach. For simplicity, let us consider initially that such transition takes place between weak modulated patterns, hence, the single-mode approximation is valid to describe both states. In this case, the ground-state wave function reads

$$\begin{aligned}\phi_{\rm hx}\left(\boldsymbol{r}\right) = &\Bigg[1+c_{1,0}\cos\left(k_0 y\right)\\ &+c_{0,1}\cos\left(\frac{k_0 x\cot\left(\theta\right)}{2}+\frac{k_0 y}{2}\right)\\ &+c_{0,1}\cos\left(\frac{k_0 x\cot\left(\theta\right)}{2}-\frac{k_0 y}{2}\right)\Bigg]/Z,\end{aligned} \tag{B1}$$

with $Z = 1 + c_{1,0}^2/2 + c_{0,1}^2$. The energy per particle function resulting from the evaluation of the functional in Eq. (5) has the generic form $\epsilon_{\rm hx} = G\left(c_{1,0}, c_{0,1}, \theta, k_0, a_s/a_{dd}, \rho\right)$. The explicit form of the function $G\left(...\right)$ is straightforward to obtain, however, since it is a lengthy expression we do not present it here.

Following the G.L. approach, we consider that in the region close to the stripes-hexagonal phase transition, the value of $c_{0,1}$ corresponding to the minimum of $G\left(...\right)$ with respect to the variational parameters is small, justifying to rewrite $G\left(...\right)$ as its expansion in powers of $c_{0,1}$. Differently from the scenario where $\alpha = 0$, in which $c_{0,1} = c_{1,0}$ and $\theta = \pi/6$, due to the presence of the six-fold rotational symmetry [43], in this case the expansion in powers of $c_{0,1}$ only contains even contributions. This produces a G.L. energy of the form

$$\begin{aligned}\epsilon_{\rm hx} = G\left(c_{0,1}=0\right) &+ \frac{1}{2!}\frac{\partial^2 G}{\partial c_{0,1}^2}\bigg|_{c_{0,1}=0} c_{0,1}^2\\ &+ \frac{1}{4!}\frac{\partial^4 G}{\partial c_{0,1}^4}\bigg|_{c_{0,1}=0} c_{0,1}^4 + O\left(c_{0,1}^4\right),\end{aligned} \tag{B2}$$

from which we can identify the conditions producing a phase transition from a stripes phase ($c_{1,0}^* \neq 0$ and $c_{0,1}^* = 0$) to a generic hexagonal phase ($c_{1,0}^* \neq 0$ and $c_{0,1}^* \neq 0$). Here, the asterisk symbol indicates the variational value of the corresponding parameter, resulting from the minimization of $\epsilon_{\rm hx}$. As expected, a scenario in which the system displays a second order phase transition is obtained when $\partial^4 G\left(c_{1.0}^*, c_{0,1}=0, \theta^*, k_0^*, a_s/a_{dd}, \rho\right)/\partial c_{0,1}^4 > 0$ and $\partial^2 G\left(c_{1,0}^*, c_{0,1}=0, \theta^*, k_0^*, a_s/a_{dd}, \rho\right)/\partial c_{0,1}^2$ changes from negative to positive as a_s/a_{dd} and ρ are varied. In the case where the fourth order derivative becomes negative, higher order terms in the expansion should be included to guarantee the stability of the system. Typically, the inclusion of higher order terms changes the nature of the transition to first order, explaining why the phase boundaries observed contain regions with continuous and discontinuous transitions.

Moreover, the position of the second order phase boundary will be determined from the set of equations

$$\begin{aligned}&\frac{\partial G}{\partial c_{1,0}}\left(c_{1,0}^*, c_{0,1}=0, \theta^*, k_0^*, a_s/a_{dd}, \rho\right) = 0,\\ &\frac{\partial^2 G}{\partial c_{0,1}^2}\left(c_{1,0}^*, c_{0,1}=0, \theta^*, k_0^*, a_s/a_{dd}, \rho\right) = 0,\\ &\frac{\partial G}{\partial k_0}\left(c_{1,0}^*, c_{0,1}=0, \theta^*, k_0^*, a_s/a_{dd}, \rho\right) = 0,\\ &\frac{\partial}{\partial\theta}\frac{\partial^2 G}{\partial c_{0,1}^2}\left(c_{1,0}^*, c_{0,1}=0, \theta^*, k_0^*, a_s/a_{dd}, \rho\right) = 0.\end{aligned} \tag{B3}$$

The solution of this set of equations allows the determination of $c_{1,0}$, θ and k_0 at the transition, as well as a_s/a_{dd} (ρ) considering ρ (a_s/a_{dd}) as a running free parameter. As the running parameter is varied, a continuum of critical points are obtained as the set of equations is solved generating our critical lines. In other words, the existence of critical lines in our case is also a consequence of the dimensionality of the space of parameters of our problem. Furthermore, we should notice that the discussion presented here can be directly generalized to the many-modes scenario as well as to the stripes-homogeneous phase transition. The main point to keep in mind in both cases is that the expansion of the energy per particle will contain only even powers of the Fourier amplitude taken as order parameter, for each of these transitions. Hence, the qualitative picture discussed above will hold in these scenarios too.

[1] E. Berg, E. Fradkin, E.-A. Kim, S. A. Kivelson, V. Oganesyan, J. M. Tranquada, and S. C. Zhang, Phys. Rev. Lett. **99**, 127003 (2007).
[2] D. G. Barci, A. Mendoza-Coto, and D. A. Stariolo, Phys. Rev. E **88**, 062140 (2013).
[3] A. Mendoza-Coto, D. A. Stariolo, and L. Nicolao, Phys. Rev. Lett. **114**, 116101 (2015).
[4] A. Mendoza-Coto, D. E. B. de Oliveira, L. Nicolao, and R. Díaz-Méndez, Phys. Rev. B **101**, 174438 (2020).
[5] A. Mendoza-Coto, D. G. Barci, and D. A. Stariolo, Phys. Rev. B **95**, 144209 (2017).
[6] L. Radzihovsky, Phys. Rev. Lett. **125**, 267601 (2020).
[7] A. Lahiri, A. Klein, and R. M. Fernandes, Phys. Rev. B **106**, L140503 (2022).
[8] S. Prestipino and F. Saija, The Journal of Chemical Physics **141**, 184502 (2014).
[9] S. Prestipino, A. Sergi, and E. Bruno, Phys. Rev. B **98**, 104104 (2018).
[10] A. Mendoza-Coto, R. Cenci, G. Pupillo, R. Díaz-Méndez, and E. Babaev, Soft Matter **17**, 915 (2021).
[11] A. Mendoza-Coto, D. d. S. Caetano, and R. Díaz-Méndez, Phys. Rev. A **104**, 013301 (2021).
[12] M. de Mello, R. Díaz-Méndez, and A. Mendoza-Coto, Entropy **25** (2023), 10.3390/e25020356.
[13] M. Ciardi, F. Cinti, G. Pellicane, and S. Prestipino, Phys. Rev. Lett. **132**, 026001 (2024).
[14] T. Dotera, T. Oshiro, and P. Ziherl, Nature **506**, 208 (2014).
[15] K. Barkan, M. Engel, and R. Lifshitz, Phys. Rev. Lett. **113**, 098304 (2014).
[16] A. Mendoza-Coto, R. Turcati, V. Zampronio, R. Díaz-Méndez, T. Macrì, and F. Cinti, Phys. Rev. B **105**, 134521 (2022).
[17] M. Ciardi, A. Angelone, F. Mezzacapo, and F. Cinti, Phys. Rev. Lett. **131**, 173402 (2023).
[18] M. Grossklags, M. Ciardi, V. Zampronio, F. Cinti, and A. Mendoza-Coto, Results in Physics **65**, 107991 (2024).
[19] V. Zampronio, A. Mendoza-Coto, T. Macrì, and F. Cinti, Phys. Rev. Lett. **133**, 196001 (2024).
[20] N. Podoliak, P. Salamon, L. Lejček, P. Kužel, and V. Novotná, Phys. Rev. Lett. **131**, 228101 (2023).
[21] J. Xia and Y. Han, Phys. Rev. Res. **6**, 033232 (2024).
[22] A. Bianconi, International Journal of Modern Physics B **14**, 3289 (2000).
[23] A. Bianconi, D. Di Castro, N. Saini, and G. Bianconi, "Superstripes," in *Phase Transitions and Self-Organization in Electronic and Molecular Networks*, edited by M. F. Thorpe and J. C. Phillips (Springer US, Boston, MA, 2001) pp. 375–388.
[24] T. D. Farokh Mivehvar, Francesco Piazza and H. Ritsch, Advances in Physics **70**, 1 (2021).
[25] L. Chomaz, I. Ferrier-Barbut, F. Ferlaino, B. Laburthe-Tolra, B. L. Lev, and T. Pfau, Reports on Progress in Physics **86**, 026401 (2022).
[26] L. Mathey, S.-W. Tsai, and A. H. Castro Neto, "Ultracold atomic gases: Novel states of matter," in *Encyclopedia of Complexity and Systems Science*, edited by R. A. Meyers (Springer New York, New York, NY, 2009) pp. 9679–9705.
[27] F. Schäfer, T. Fukuhara, S. Sugawa, Y. Takasu, and Y. Takahashi, Nat. Rev. Phys. **2**, 411 (2020).
[28] L. Tanzi, E. Lucioni, F. Famà, J. Catani, A. Fioretti, C. Gabbanini, R. N. Bisset, L. Santos, and G. Modugno, Phys. Rev. Lett. **122**, 130405 (2019).
[29] M. Lu, N. Q. Burdick, S. H. Youn, and B. L. Lev, Phys. Rev. Lett. **107**, 190401 (2011).
[30] K. Aikawa, A. Frisch, M. Mark, S. Baier, A. Rietzler, R. Grimm, and F. Ferlaino, Phys. Rev. Lett. **108**, 210401 (2012).
[31] L. Chomaz, D. Petter, P. Ilzhöfer, G. Natale, A. Trautmann, C. Politi, G. Durastante, R. M. W. van Bijnen, A. Patscheider, M. Sohmen, M. J. Mark, and F. Ferlaino, Phys. Rev. X **9**, 021012 (2019).
[32] F. Böttcher, J.-N. Schmidt, M. Wenzel, J. Hertkorn, M. Guo, T. Langen, and T. Pfau, Phys. Rev. X **9**, 011051 (2019).
[33] T. D. Lee, K. Huang, and C. N. Yang, Phys. Rev. **106**, 1135 (1957).
[34] D. Baillie, R. M. Wilson, R. N. Bisset, and P. B. Blakie, Phys. Rev. A **94**, 021602 (2016).
[35] R. N. Bisset, R. M. Wilson, D. Baillie, and P. B. Blakie, Phys. Rev. A **94**, 033619 (2016).
[36] R. Bombin, J. Boronat, and F. Mazzanti, Phys. Rev. Lett. **119**, 250402 (2017).
[37] E. P. Gross, Phys. Rev. **106**, 161 (1957).
[38] M. Boninsegni and N. V. Prokof'ev, Rev. Mod. Phys. **84**, 759 (2012).
[39] P. B. Blakie, D. Baillie, L. Chomaz, and F. Ferlaino, Phys. Rev. Res. **2**, 043318 (2020).
[40] M. A. Norcia, C. Politi, L. Klaus, E. Poli, M. Sohmen, M. J. Mark, R. N. Bisset, L. Santos, and F. Ferlaino, Nature **596**, 357 (2021).
[41] T. Bland, E. Poli, C. Politi, L. Klaus, M. A. Norcia, F. Ferlaino, L. Santos, and R. N. Bisset, Phys. Rev. Lett. **128**, 195302 (2022).
[42] Z.-K. Lu, Y. Li, D. S. Petrov, and G. V. Shlyapnikov, Phys. Rev. Lett. **115**, 075303 (2015).
[43] Y.-C. Zhang, F. Maucher, and T. Pohl, Phys. Rev. Lett. **123**, 015301 (2019).
[44] Y.-C. Zhang, T. Pohl, and F. Maucher, Phys. Rev. Res. **6**, 023023 (2024).
[45] E. Poli, T. Bland, C. Politi, L. Klaus, M. A. Norcia, F. Ferlaino, R. N. Bisset, and L. Santos, Phys. Rev. A **104**, 063307 (2021).
[46] J. Hertkorn, J.-N. Schmidt, M. Guo, F. Böttcher, K. S. H. Ng, S. D. Graham, P. Uerlings, T. Langen, M. Zwierlein, and T. Pfau, Phys. Rev. Res. **3**, 033125 (2021).
[47] M. Schmidt, L. Lassablière, G. Quéméner, and T. Langen, Phys. Rev. Res. **4**, 013235 (2022).
[48] Y.-C. Zhang, T. Pohl, and F. Maucher, Phys. Rev. A **104**, 013310 (2021).
[49] B. T. E. Ripley, D. Baillie, and P. B. Blakie, Phys. Rev. A **108**, 053321 (2023).
[50] Y. Kora and M. Boninsegni, Journal of Low Temperature Physics **197**, 337 (2019).
[51] F. Cinti and M. Boninsegni, Phys. Rev. A **96**, 013627 (2017).
[52] T. Macrì, F. Maucher, F. Cinti, and T. Pohl, Phys. Rev. A **87**, 061602 (2013).
[53] M. Kunimi and Y. Kato, Phys. Rev. B **86**, 060510 (2012).
[54] C.-H. Hsueh, T.-C. Lin, T.-L. Horng, and W. C. Wu, Phys. Rev. A **86**, 013619 (2012).

[55] S. Saccani, S. Moroni, and M. Boninsegni, Phys. Rev. Lett. **108**, 175301 (2012).
[56] R. Schützhold, M. Uhlmann, Y. Xu, and U. R. Fischer, Int. J. Mod. Phys. B **20**, 3555–3565 (2006).
[57] A. R. P. Lima and A. Pelster, Phys. Rev. A **84**, 041604 (2011).
[58] A. R. P. Lima and A. Pelster, Phys. Rev. A **86**, 063609 (2012).
[59] Here is important to notice that the areal density along the plane of the system ($\rho_\perp$) set by the harmonic trap can be written as $\rho_\perp = \rho\cos(\alpha)$.
[60] P. B. Blakie, Journal of Physics B: Atomic, Molecular and Optical Physics **57**, 115301 (2024).
[61] C. Josserand, Y. Pomeau, and S. Rica, Phys. Rev. Lett. **98**, 195301 (2007).
[62] N. Sepúlveda, C. Josserand, and S. Rica, The European Physical Journal B **78**, 439 (2010).
[63] L. D. Landau and E. M. Lifshitz, *Theory of Elasticity*, 3rd ed., Course of Theoretical Physics, Vol. 7 (Pergamon Press, Oxford, 1986).
[64] A. Tononi and L. Salasnich, Phys. Rev. Lett. **123**, 160403 (2019).
[65] A. Tononi, F. Cinti, and L. Salasnich, Phys. Rev. Lett. **125**, 010402 (2020).
[66] A. Tononi and L. Salasnich, Nature Reviews Physics **5**, 398 (2023).
[67] L. E. Young-S. and S. K. Adhikari, Phys. Rev. A **108**, 053323 (2023).
[68] L. Chomaz, R. M. W. van Bijnen, D. Petter, G. Faraoni, S. Baier, J. H. Becher, M. J. Mark, F. Wächtler, L. Santos, and F. Ferlaino, Nat. Phys. **14**, 442 (2018).
[69] H. Kadau, M. Schmitt, M. Wenzel, C. Wink, T. Maier, I. Ferrier-Barbut, and T. Pfau, Nature **530**, 194 (2016).
[70] M. Schmitt, M. Wenzel, F. Böttcher, I. Ferrier-Barbut, and T. Pfau, Nature **539**, 259 (2016).

3 Publication: *Engineering interaction potentials for stabilizing quantum quasicrystal phases*

Engineering interaction potentials for stabilizing quantum quasicrystal phases

Matheus Grossklags,[1,*] Daniel Lima,[1] Vinicius Zampronio,[2,†] Fabio Cinti,[2,3,4,‡] and Alejandro Mendoza-Coto[1,2,§]

[1] *Departamento de Física, Universidade Federal de Santa Catarina, 88040-900 Florianópolis, Brazil*
[2] *Dipartimento di Fisica e Astronomia, Università di Firenze, I-50019, Sesto Fiorentino (FI), Italy*
[3] *INFN, Sezione di Firenze, I-50019, Sesto Fiorentino (FI), Italy*
[4] *Department of Physics, University of Johannesburg, P.O. Box 524, Auckland Park 2006, South Africa*

We investigate the necessary features of the pair interaction for the stabilization of self-assembled quantum quasicrystals in two-dimensional bosonic systems. Unlike the classical scenario, our results show that two-dimensional octagonal, decagonal, and dodecagonal aperiodic phases require a distinct number of properly tuned characteristic length scales for their stabilization. By using a mean field spectral variational approach and Gross-Pitaevskii numerical calculations, we determine that the dodecagonal quasicrystal structure requires at least two characteristic length scales for its stabilization, while the decagonal and octagonal patterns need at least three and four length scales, respectively. The family of pair interaction potentials considered, albeit simple, is well justified in terms of a novel experimental platform based on laser-painted interactions in a cavity QED setup. Finally, we perform a structural characterization of the quasicrystal patterns obtained and show that these phases coexist with a finite superfluid fraction, forming what can be called a super quasicrystal phase.

I. INTRODUCTION

The self-assembly of complex phases such as cluster crystals[1–4], quasicrystals[5–15], supersolids[16–21], and topological phases[22–28] is a central topic of many-body physics, with applications in soft matter[29–34] and hard condensed matter[35–42]. In particular, quasicrystals in two and three dimensions are characterized by a lack of spatial periodicity while exhibiting long-range n-fold rotational symmetry (with $n > 6$) forbidden by conventional crystallography[43–45]. One singular realization of this kind of system are the so-called cluster quasicrystals[10,12]. These systems are typically produced by isotropic soft-core pair potentials with a degenerate two minima structure in momentum space properly tuned, at moderate temperatures[46,47]. To be precise, the relative position of the two competing unstable wave vectors controls the self-assembling process and hence the rotational symmetry of the stabilized quasicrystal[10]. Such interplay between length scales has been extensively studied using the Lifshitz-Petrich-Gaussian model[10,48] due to its mathematical flexibility, which allows the stabilization of periodic and aperiodic phases as the minima structure of the potential and thermal fluctuations are tuned.

These insights have recently guided the search for novel quantum phases, showing that the combined effect of tailored interactions and quantum fluctuations can similarly stabilize quantum quasicrystals[12–14,49]. Interestingly, all studies focusing on quantum self-assembled quasicrystals analogous to the one considered by Barkan et al.[10], but at zero temperature, have been related to the stabilization of a dodecagonal phase. In this case, the literature[13,50] seems to indicate that to enhance stability or even to achieve the stabilization of these phases at all, either the higher momentum minimum should be deeper than the low momentum minimum, or extra resonant incommensurate minima should be added to the pair interaction potential. In this scenario, to push forward the comprehension of the necessary properties of the pair interaction potential for the stabilization of quantum quasicrystals, it is essential to consider scenarios with different rotational symmetries.

Ultracold atoms provide a versatile platform for investigating quantum quasicrystals. With precise control over both internal and external degrees of freedom, these systems have been used to simulate a wide range of quantum phases[51–56]. However, the realization of quasicrystals[54,57] and other exotic phases[58,59] often requires long-range or oscillatory interactions, which are not typically accessible in systems of quantum gases. One novel approach involves the use of a high-finesse optical cavity and a beam shaped laser scanning the system to produce tailored effective sign-changing interactions between the atoms of the system[60]. In this work, the authors show that the effective interaction having the form $\hat{V}(\boldsymbol{q}) = g_{\rm aa} - \Delta\,\hat{\Omega}(\boldsymbol{q})^2$, is controlled by the Fourier transform of the Rabi frequency profile of the laser $\hat{\Omega}(\boldsymbol{q})$, the original contact interaction between atoms $g_{\rm aa}$ and the parameter Δ accounting for microscopic details of the quantum mechanism involved in the interaction process. The resulting expression offers an unprecedented degree of customization, providing the same level of flexibility of the Lifshitz-Petrich-Gaussian model for the production of classical quasicrystals and other modulated phases. Although this pioneering protocol has not been tested experimentally yet, similar setups have been successfully used already to stabilize supersolids[61,62], spin textured phases[54,58,63], and extended Hubbard models[64,65].

* matheus.grossklags@posgrad.ufsc.br
† v.zampronio@unifi.it
‡ fabio.cinti@unifi.it
§ alejandro.mendoza@ufsc.br

In the present paper, we use a mean field spectral variational approach[13,14,66] to explore the engineering principles of the pair interaction potential in Fourier space for the stabilization of three prominent quantum quasicrystal phases with octagonal, decagonal, and dodecagonal rotational symmetries. We systematically consider the effects of having two or more competing length scales in the pair potential properly tuned in order to stabilize the corresponding quasicrystal phase and enhance its extension in the ground state phase diagram. We show that, in contrast to the classical scenario, the stabilization of quantum quasicrystals with different rotational symmetries requires pair interaction potentials with a very distinct minima structure. Next, we investigate the reasons for the much greater stability of the dodecagonal structure in comparison to the decagonal and octagonal patterns and present a geometric argument clarifying the origin of such phenomenon. Moreover, to deepen our understanding on the reported phases, we analyze the behavior of the superfluid fraction in three particular cases showing that quasicrystalline order can coexist with global superfluidity, exhibiting a phase analogous to the supersolid phase. We employed two contrasting methods to study the superfluidity, the mean field spectral variational method and the numerical solution of the real-space Gross-Pitaevskii equation in imaginary time, showing that both techniques provide equivalent results. Finally, we discuss the results and present the concluding remarks of our work.

The paper is organized as follows: In Section II we introduce the model Hamiltonian and the applied methodology, while Section III presents results concerning the dodecagonal structure. Decagonal quasicrystal is presented in Section IV. Finally in Section V we discuss the octagonal setup. Section VI is devoted to our final remarks and conclusions.

II. MODEL AND METHOD

We consider a two-dimensional gas of N bosonic particles with mass m at zero temperature interacting with a pair potential $V(\boldsymbol{x})$. Within the mean field approximation, valid at high density of particles and weak enough interactions, the total energy of the system can be expressed as

$$E[\phi] = \frac{\hbar^2}{2m}\int d^2x|\boldsymbol{\nabla}\phi(\boldsymbol{x})|^2 + \frac{1}{2}\int d^2x d^2x' V(\boldsymbol{x}-\boldsymbol{x}') \times |\phi(\boldsymbol{x})|^2|\phi(\boldsymbol{x}')|^2, \tag{1}$$

where $\phi(\boldsymbol{x})$ stands for the wave function of the condensate, satisfying the normalization condition $\int d^2x|\phi(\boldsymbol{x})|^2 = N$. Moreover, we consider that the pair interaction potential is written in momentum space as $\hat{V}(\boldsymbol{q}) = g_{\rm aa} - \Delta\,\hat{\Omega}(\boldsymbol{q})^2$, such model of pair interaction was presented and discussed earlier in the introduction section. For a study of the stabilization conditions of distinct quasicrystal structures, we consider a rather simple laser beam model in momentum space $\hat{\Omega}(\boldsymbol{q})$, given by the superposition of several Gaussian profiles centered at different momenta with negligible overlapping between them. As a consequence, the pair interaction potential $\hat{V}(\boldsymbol{q})$ exhibits a series of local minima properly positioned in order to favor the stabilization of a particular quasicrystalline pattern[13,14].

To stabilize a quasicrystal exhibiting n-fold rotational symmetry with characteristic momentum q_1, it is expected that in addition to q_1, other resonant momenta associated with the corresponding quasicrystal structure should also be excited. In general, if we combine two wave vectors of the extended basis $\boldsymbol{q}_i = q_1(\cos(2\pi i/n), \sin(2\pi i/n))$ with $i = 0, 1, \ldots, n-1$, we obtain the first group of secondary characteristic wave vectors of the corresponding pattern. For the three simplest and most relevant quasicrystalline structures, octagonal, decagonal, and dodecagonal, $n = 8, 10$, and 12, respectively, the first group of secondary wave vectors contains three or more different sets of vectors with an incommensurate length with respect to the characteristic wave vector. Taking this into account, our approach to study the stabilization of quasicrystalline patterns involves separately exciting these length scales in $\hat{\Omega}(\boldsymbol{q})$, thus clarifying the necessary number of minima in $\hat{V}(\boldsymbol{q})$ for the desired quasicrystal stabilization. In this way, we consider

$$\hat{\Omega}(\boldsymbol{q}) = \sum_{j=1}^{4}\omega_j \exp\left(-\frac{(q-q_j)^2}{\alpha_j^2}\right), \tag{2}$$

where ω_j, α_j and q_j are positive parameters measuring the intensity, width and characteristic momentum of each Gaussian peak in $\hat{\Omega}(\boldsymbol{q})$, respectively. As previously discussed, once the characteristic momentum is set by the main peak in $\hat{V}(q)$, the position of the secondary modes to be excited are located at specific irrational numbers in units of q_1.

Considering q_1 the main wave vector of the quasicrystal structure as our unit of momentum, it is natural to choose $\lambda = 1/q_1$ and $\epsilon = \hbar^2/m\lambda^2$ as units of length and energy, respectively. Hence, the dimensionless vector position and momentum are defined as $\boldsymbol{r} = \boldsymbol{x}/\lambda$ and $\boldsymbol{k} = \boldsymbol{q}/q_1$. Considering these units of energy and length, the dimensionless energy per particle functional for our model writes

$$\frac{E[\psi]}{N\epsilon_0} = \frac{1}{2}\int\frac{d^2r}{A}|\boldsymbol{\nabla}\psi(\boldsymbol{r})|^2 + \frac{\lambda^2 U\rho}{2}\int\frac{d^2r d^2r'}{A} v(\boldsymbol{r}-\boldsymbol{r}')|\psi(\boldsymbol{r})|^2|\psi(\boldsymbol{r}')|^2, \tag{3}$$

where A stands for the area of the system and $\psi(\boldsymbol{r})$ represents the normalized wave function, satisfying $\int_A d^2r|\psi(\boldsymbol{r})|^2 = A$. Furthermore, the effective pair interaction potential $Uv(\boldsymbol{r})$ corresponds originally to $V(\boldsymbol{x})/\epsilon$. Here, we have introduced the dimensionless parameter U

to quantify the intensity of the pair interaction potential and $v(\boldsymbol{r})$ to encode the information about its spatial variation. To avoid any ambiguity in this definition we impose additionally that $\hat{v}(k=1)=-1$, without generality loss. Under these conditions, the local dimensionless density of particles is given by $\rho(\boldsymbol{r})=\lambda^2\rho|\psi(\boldsymbol{r})|^2$, where ρ represents the average particles density. It is worth noticing that within our framework the dimensionless parameter $\lambda^2 U\rho$ controls the relative intensity of the potential energy contribution in comparison to the kinetic energy in the ground-state energy functional, or in other words the intensity of the quantum fluctuations (zero point motion) in our system. In this way, $\lambda^2 U\rho$ is naturally one of the running parameter of the phase diagrams for the models considered.

To proceed, we consider that the ground-state wave function $\psi(\boldsymbol{r})$ minimizing the energy-per-particle functional can be written in a Fourier basis. In this way, we propose[13,17]

$$\psi(\boldsymbol{r})=\frac{1+\frac{1}{2}\sum_{j\neq 0}c(\boldsymbol{k}_j)\cos(\boldsymbol{k}_j\cdot\boldsymbol{r})}{\left(1+\frac{1}{4}\sum_{j\neq 0}c(\boldsymbol{k}_j)^2\right)^{1/2}}, \tag{4}$$

where $c(\boldsymbol{k}_j)$ and $\boldsymbol{k}_j$ represent the Fourier amplitudes and wave vectors of the expansion. The set of wave vectors and amplitudes $\{\boldsymbol{k}_j, c(\boldsymbol{k}_j)\}$ defines the type of modulated pattern under consideration and its symmetries. These wave vectors are constructed as all possible integers combinations of a vector basis $\{\boldsymbol{k}_{j,0}\}$, the number of elements of the basis defines the rank of the solution. In two dimensions, periodic pattern solutions correspond to configurations of rank 2 or smaller, while quasicrystals have a rank higher than 2. In Table I, we present the list of solutions considered as well as its wave vector basis, here the variational parameter k_m sets the scale of the wave vectors lattice. In terms of possible solutions, we consider all periodic patterns typically found in quasicrystal forming systems[10]: one dimensional modulations, i.e., stripes, 2D hexagonal and square crystalline patterns, as well as two different kinds of compressed hexagonal patterns exciting simultaneously the two dominant characteristic wave vectors of the pair potential[67–69] and finally, n-fold rotationally symmetric quasicrystals with $n=\{8,10,12\}$. Within the mean field spectral variational analysis, the set of Fourier amplitudes $\{c_j\}$ and the characteristic momentum k_m for each possible solution are determined from the minimization of the corresponding energy-per-particle functional[30,70]. Finally, the ground state is calculated selecting the solution with the lowest energy. For the special case of the homogeneous solution, all coefficients c_j vanish except for $c_0=1$. It is important to observe that the variational complexity of our problem can be significantly reduced by recognizing that Fourier amplitudes c_j's corresponding to equivalent wave vectors $\boldsymbol{k}_j$'s after symmetry operations of the associated density pattern should be equal. For numerical purposes, the Fourier expansion in Eq. (4) for each kind of solution is truncated using a large enough set of modes to guarantee energy convergence. Moreover, the truncation process employed guarantees that the symmetries of the corresponding pattern are fully preserved by the truncated anzats solution.

Pattern	Vector basis $\boldsymbol{k}_{j,0}$	Index range
Stripes	$k_m(1,0)$	
Square	$k_m(\cos(2\pi j/4),\sin(2\pi j/4))$	$j=0,1.$
Hexagonal	$k_m(\cos(2\pi j/6),\sin(2\pi j/6))$	$j=0,1.$
Comp. Hex.1	$k_m\left(1/2,\pm\sqrt{\tilde{k}_2^2-1/4}\right)$	
Comp. Hex.2	$k_m\left(\tilde{k}_2/2,\pm\sqrt{1-\tilde{k}_2^2/4}\right),$	
8-QC	$k_m(\cos(2\pi j/8),\sin(2\pi j/8))$	$j=0,\ldots,3.$
10-QC	$k_m(\cos(2\pi j/10),\sin(2\pi j/10))$	$j=0,\ldots,3.$
12-QC	$k_m(\cos(2\pi j/12),\sin(2\pi j/12))$	$j=0,\ldots,3.$

Table I. Modulated patterns considered in this work and their corresponding wave vector basis $\boldsymbol{k}_{j,0}$. The list of of possible solutions includes: stripes, square and hexagonal crystalline patterns, compressed hexagonal patterns exciting simultaneously wave vectors on the ratio $\tilde{k}_2$ (see Table II) and quasicrystalline patterns with eight- (8-QC), ten- (10-QC) or twelvefold (12-QC) rotational symmetry.

A. Pair interaction potential

Considering the model proposed for the laser profile $\hat{\Omega}(\boldsymbol{q})$, we represent the dimensionless pair interaction potential $\hat{v}(k)$ in the general form

$$\hat{v}(k)=g-\left(\sum_{j=1}^{4}d_j\exp\left[-\left(k-\tilde{k}_j\right)^2/\sigma_j^2\right]\right)^2, \tag{5}$$

As a consequence of our choice of length and energy scales, we have $\tilde{k}_1=1$ as the position of the first minimum in all cases, while the other minima in $\hat{v}(k)$ are located at selected incommensurate values favoring the stabilization of a selected n-fold quasicrystalline pattern, see Table II for details. To identify the key ingredients in this process, we considered pair interactions with a varying number of minima, i.e., considering cases in which some of the coefficients d_j's are equal to zero. Once we select a particular minima structure positioned at $\{\tilde{k}_j\}$ in momentum space, the corresponding coefficients $\{d_j\}$ are obtained setting the values of the pair potential at the local minima $\{\hat{v}(\tilde{k}_j)\}$. For all cases considered, we have $g=10$, $\sigma_j=0.1$ and $\hat{v}(\tilde{k}_1)=-1$. This choice of dimensionless parameters is consistent with the range

Pattern	$\tilde{k}_2$	$\tilde{k}_3$	$\tilde{k}_4$
8-QC	$2\cos(\pi/8)$	$2\cos(3\pi/8)$	$2\cos(2\pi/8)$
10-QC	$2\cos(\pi/10)$	$2\cos(4\pi/10)$	$2\cos(2\pi/10)$
12-QC	$2\cos(\pi/12)$	$2\cos(5\pi/12)$	$2\cos(3\pi/12)$

Table II. Secondary wave vectors excited in $\hat{v}(k)$ for each quasicrystal structure considered. The patterns n-QC, with $n = 8$, 10 and 12, correspond to the octagonal, decagonal, and dodecagonal structures, respectively.

of values achievable in current experiments for the contact interaction and intensity of the laser, respectively[60]. For a systematic study, we determine the ground-state phase diagram of the different cases using as running parameters the dimensionless intensity of the pair potential $\lambda^2 U\rho$ and the value of the pair potential at a local minimum $\hat{v}(\tilde{k}_j)$, where $\tilde{k}_j$ represents a selected resonant wave vector of the corresponding structure (see Table II).

B. Superfluid fraction

To deepen our characterization of the quasicrystalline phases, we study the behavior of the superfluid fraction (f_s) in these states. From the knowledge of the ground-state wave function $\psi(\boldsymbol{r})$ the superfluid fraction can be estimated by means of the Legget criterion, which provides a lower bound for this quantity. Following well established literature[71,72] we consider

$$f_s = \mathrm{Max}_\alpha \left[\int_0^L \frac{dx'}{L} \left(\int_0^L \frac{dy'}{L} |\psi'(\boldsymbol{r}')|^{-2} \right)^{-1} \right]. \qquad (6)$$

In Eq. (6), the prime symbol indicates that the coordinate system is rotated at an angle α with respect to the original coordinate system, consequently $\psi'(\boldsymbol{r}') = \psi(x'\cos(\alpha) - y'\sin(\alpha), x'\sin(\alpha) + y'\cos(\alpha))$. As occurs in the case of supersolids[73], the angle α providing the highest value for f_s coincides with the main directions of the structure, which in our case are given by the angles $\alpha_i = 2\pi i/n$, with $i = 0, ..., n-1$, for an n-fold quasicrystalline phase. Hence, for calculation purposes, we can simply set $\alpha = 0$.

The simultaneous characterization of the superfluid properties and the density pattern allow us to identify different kinds of phases: supersolid states, when superfluidity and a crystalline density pattern coexist, super quasicrystalline states, when the quasicrystal patterns present a finite superfluid fraction, and homogeneous superfluid phases. Moreover, all these phases have their insulating counterparts when the superfluid fraction is close enough to zero[13,14,74].

C. Gross-Pitaevskii equation

To verify the results computed within the spectral mean field variational method, we numerically solve the Gross-Pitaevskii[75,76] equation (GPE) evolved in imaginary time, which provides the ground-state wave function and allows the calculation of the observables of our choice.

The dimensionless GPE evolved in imaginary time $\tau = it$ for the model under consideration reads

$$\frac{\partial\psi(\boldsymbol{r},\tau)}{\partial\tau} = \left[\frac{1}{2}\nabla^2 - N\int d\boldsymbol{r}' v(\boldsymbol{r}-\boldsymbol{r}') |\psi(\boldsymbol{r}',\tau)|^2 \right] \psi(\boldsymbol{r},\tau). \qquad (7)$$

Eq. (7) is then solved numerically using an adaptive Runge-Kutta method, with a simulation box of linear size $L = 512\lambda$ and discretization $\Delta x = \Delta y = 0.25\lambda$. The non-local term $v_{NL}(\boldsymbol{r}) = \int d\boldsymbol{r}' v(\boldsymbol{r}-\boldsymbol{r}') |\psi(\boldsymbol{r}',\tau)|^2$ is computed efficiently with the use of fast-Fourier transformations since $\mathscr{F}[v_{NL}](\boldsymbol{k}) = \mathscr{F}[v](\boldsymbol{k})\,\mathscr{F}[|\psi|^2](\boldsymbol{k})$.

As mentioned previously, the ground-state wave function is found as the optimal stationary state of the GPE calculated using a variety of initial conditions. Our initial conditions are given by a droplet on a null background of each modulated pattern considered in our mean field spectral variational analysis placed at the center of our simulation box. When the corresponding pattern is metastable this droplet grows until covering the whole simulation box. If we integrate the GPE for long enough imaginary time a stationary state is achieved. In this way, all the metastable solutions obtained from GPE, which includes the ground state, can be compared with their counter part calculated from the variational approach. For all models considered, we observed a striking agreement between configurations computed in both ways, to show quantitatively such agreement we systematically compare the ground-state superfluid fraction using as inputs these configurations.

III. DODECAGONAL QUASICRYSTAL

To study the stabilization of the dodecagonal quasicrystalline pattern, we begin by considering an effective interaction potential with two length scales. The first minimum in $\hat{v}(k)$ is placed at $k = k_1 = 1$ while the second one is positioned at $k = \tilde{k}_2$, which corresponds to a length scale associated with a resonant wave vector of the dodecagonal structure (see Table II). By fixing the depth of the first minimum to be $\hat{v}(\tilde{k}_1) = -1$, it is possible to study the stabilization of the dodecagonal phase as the vertical position of the second minimum is varied. The form of $\hat{v}(k)$ is shown in Fig. 1(a) for three distinct values of the depth of the second minimum $\hat{v}(\tilde{k}_2)$ and the

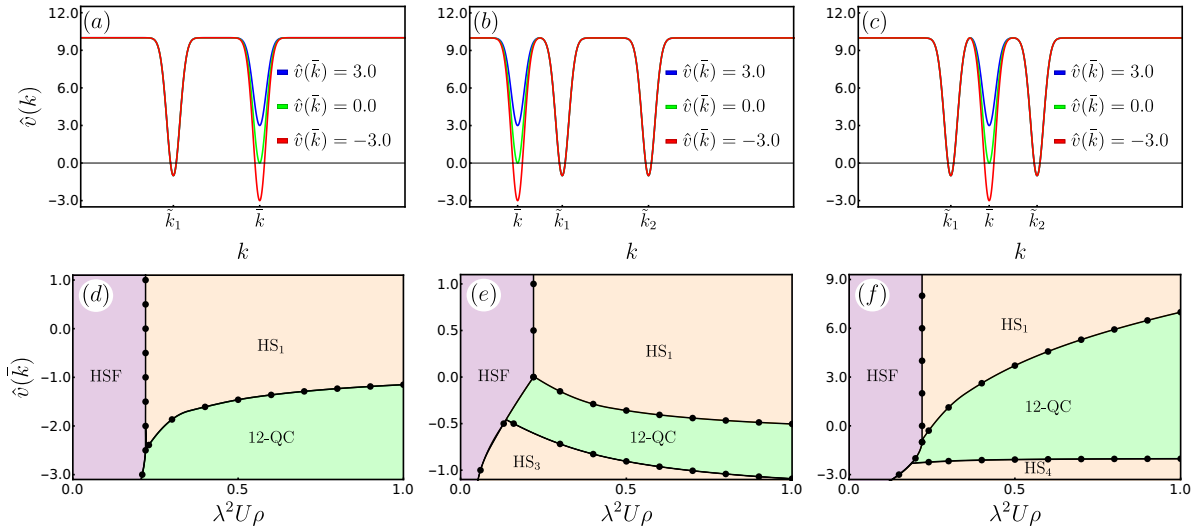

Figure 1. (a)-(c) Pair interaction potential minima structure in Fourier space for the corresponding phase diagrams in (d)-(f), where the first length scale is positioned at $k = \tilde{k}_1 = 1$ and the secondary resonant scales are determined in Table II. Phase diagram for the minima structure associated with the dodecagonal quasicrystal where (d) $\bar{k} = \tilde{k}_2$ (e) $\bar{k} = \tilde{k}_3$ and (f) $\bar{k} = \tilde{k}_4$ indicates the position of the minimum in reciprocal space for which we modify the depth as a parameter to determine the ground state of the system. The acronym HSF stands for homogeneous superfluid, whereas HS and 12-QC stands for hexagonal solid and dodecagonal quasicrystal phases, respectively. The hexagonal states HS_i refers to a hexagonal phase with characteristic wave vectors dominated by the minimum of $\hat{v}(k)$ at $\tilde{k}_i$.

corresponding ground-state phase diagram in the $\hat{v}(\tilde{k}_2)$–$\lambda^2 U\rho$ plane is shown in Fig. 1(d). As can be observed, three different phases are identified, a homogeneous superfluid phase (HSF) at low values of $\lambda^2 U\rho$, a dodecagonal quasicrystal (12-QC) phase for low values of $\hat{v}(\tilde{k}_2)$ and a hexagonal solid phase (HS_1) with characteristic momentum given by $\tilde{k}_1$. We notice that the presence of a second minimum at the first resonant wave vector of the dodecagonal structure is sufficient to stabilize such quasicrystalline phase when this minimum is deep enough. However, in the case of a degenerate minima structure, i.e. $\hat{v}(\tilde{k}_1) = \hat{v}(\tilde{k}_2)$, the 12-QC phase is only stabilized at large values of $\lambda^2 U\rho$ in a regime where presumably particles will be largely localized, in agreement with previous works[13]. Moreover, we observe that as the value of the second minimum in $\hat{v}(k)$ is decreased, the transition from the HS_1 phase to the 12-QC phase moves to lower values of $\lambda^2 U\rho$. This behavior is maintained up to the point at which we observe a direct transition from the superfluid to the 12-QC phase.

To further study the stabilization of the 12-QC phase, we modify the interaction potential including a third characteristic length scale manifesting as a minimum in $\hat{v}(k)$ at a resonant wave vector different from $\tilde{k}_2$. Here we decided to consider a scenario in which the minima in $\hat{v}(k)$ at $k = \tilde{k}_1$ and $k = \tilde{k}_2$ are degenerate, since this is a quite common assumption for models developing quasicrystalline phases, and investigate the effects of varying the depth of the third minimum added to $\hat{v}(k)$. Firstly, we examine the situation in which the third minima is added at $k = \tilde{k}_3$ (see Table II), examples of the resulting pair potential $\hat{v}(k)$ are shown in Fig. 1(b). The corresponding phase diagram in the $\hat{v}(\tilde{k}_3)$–$\lambda^2 U\rho$ plane is presented in Fig. 1(e). In agreement with the phase diagram obtained for the model with two minima, we observe that the addition of a third minimum not too deep in the pair interaction potential does not produce the stabilization of the 12-QC phase in the range of $\lambda^2 U\rho$ considered. However, when this minimum becomes negative we observe the existence of an interval of values in which the 12-QC phase is again stabilized. Finally, we observe that when the third minimum added is deep enough, a reentrant transition to a new hexagonal phase (HS_3) with characteristic wave vector given by $\tilde{k}_3$ takes place. This behavior is already expected since an isolated dominant minimum is anticipated to stabilize a hexagonal ground state.

Lastly, we consider the excitation of a third minimum at the remaining wave vector belonging to the first generation of resonant wave vectors of the dodecagonal quasicrystal, the one with $k = \tilde{k}_4$ (see Table II). In this scenario, the interaction potential takes the form depicted in Fig. 1(c) and the corresponding ground-state phase diagram varying $\hat{v}(\tilde{k}_4)$ is shown in Fig. 1(f). As can be observed, the addition of this third length scale is much more effective in promoting the stabilization of the quasicrystalline phase when compared to the scenario shown in Fig. 1(e). In this case, even the addition of a positive

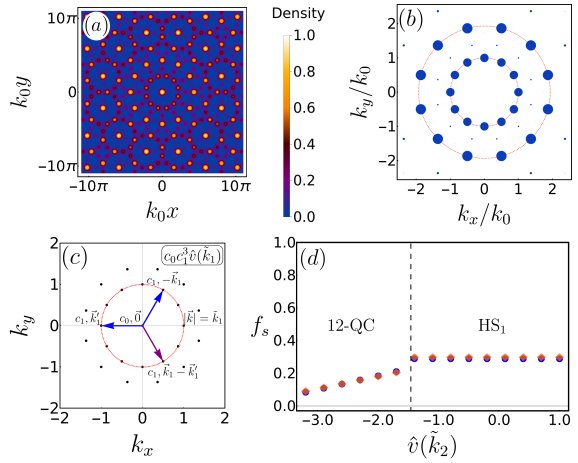

Figure 2. (a) Real space mapping for the dodecagonal structure in the phase diagram of Fig. 1(d) for parameter values $\hat{v}(\tilde{k}_2) = -2.30$ and $\lambda^2 U\rho = 0.50$ and its corresponding (b) diffraction pattern. The red circles indicates the two minima and the size of the Fourier modes in blue disks is scaled by a linear function, where the zero harmonic mode has been omitted. (c) Most relevant energy contributions to the total energy of the quasicrystalline structures as a contraction in the $\tilde{k}_1 = 1$ layer for the dodecagonal vectors. (d) Superfluid fraction for a fixed density value $\lambda^2 U\rho = 0.50$ in the dodecagonal quasicrystal for the ground state depicted in Fig. 1(d). The blue points represents the superfluid fraction obtained via mean field spectral variational method while the orange diamonds are determined via the solution of the GPE.

minimum with a relative high value already induces the stabilization of the 12-QC for moderate values of $\lambda^2 U\rho$. As expected, the strongest effect is achieved when the minimum is negative and in this case the preemptive hexagonal phase HS$_1$ is not present and we have a direct transition from the HSF to the 12-QC phase when $\lambda^2 U\rho$ is increased. Moreover, as in the previous case, a further decrease of $\hat{v}(\tilde{k}_4)$ eventually promotes a transition to the HS$_4$ phase with characteristic wave vector close to $\tilde{k}_4$.

The three scenarios discussed above show different routes for the stabilization of the 12-QC phase in two dimensional bosonic gases. Although, in this case, the presence of two properly positioned minima is enough for such stabilization, differently from the classical case[10,47], it requires a second high-momentum minimum much deeper than the first one to stabilize the 12-QC phase in the low $\lambda^2 U\rho$ regime. Alternatively, the addition of a third minimum to $\hat{v}(k)$ at $\tilde{k}_3$ or $\tilde{k}_4$ enhance significantly the stability of the 12-QC phase, even allowing us to observe this phase with a degenerate pair potential ($\hat{v}(\tilde{k}_1) = \hat{v}(\tilde{k}_2)$). In this sense, by comparing Fig. 1(e) and Fig. 1(f) we conclude that in order to enhance the stability of the 12-QC phase, it is more effective to decrease $\hat{v}(\tilde{k}_4)$ than $\hat{v}(\tilde{k}_3)$.

Regarding the structural properties of the 12-QC phase, as an example, we consider the scenario presented in Fig. 1(a) with parameters $\hat{v}(\tilde{k}_2) = -2.30$ and $\lambda^2 U\rho = 0.50$. In Fig. 2(a), we show the ground-state density pattern obtained after the energy minimization, and in Fig. 2(b) a graphic of the corresponding Fourier transform of the solution. The radii of the circles are proportional to the modulus of the Fourier amplitudes, excluding the circle corresponding to the $k = 0$ Fourier mode, which is not presented. The red circumferences indicate the position of the minima of $\hat{v}(k)$ in this case. As can be observed, the presence of the minima in $\hat{v}(k)$ controls which are the main modes excited in the quasicrystalline density pattern, this kind of phenomenology was verified in all scenarios considered in this work.

To better understand the process of stabilization of the dodecagonal pattern and the greater stability of this structure in comparison with other quasicrystalline phases, as we will see later, we consider a simplified two-mode expansion including only the two main modes of the structure with $|\boldsymbol{k}_j| = \{\tilde{k}_1, \tilde{k}_2\}$, as it is the case in Fig. 1(a). Our goal here is to assess the relative importance of the various interactions present in the energy per particle functional. Replacing Eq. (4) into Eq. (3) we can obtain the general expression:

$$\frac{E[\psi]}{N} = \frac{1}{8Z}\sum_j \boldsymbol{k}_j^2 |c(\boldsymbol{k}_j)|^2 + \frac{\lambda^2 U\rho}{32Z^2}\sum_{j,l,m} c(\boldsymbol{k}_j)\, c(\boldsymbol{k}_j + \boldsymbol{k}_l)^* \times \\ \times\, c(\boldsymbol{k}_m)\, c(\boldsymbol{k}_m - \boldsymbol{k}_l)^*\, \hat{v}(\boldsymbol{k}_l)\,, \tag{8}$$

where $Z = \frac{1}{4}\sum_j c(\boldsymbol{k}_j)^2$ and $c(0) = 2$. This expression is general and naturally remains valid for the two mode ansatz under consideration. As we can observe from Eq. (8), the potential energy contribution is given as a sum of contractions of four Fourier amplitudes paired carrying momentum $\boldsymbol{k}_l$ and $-\boldsymbol{k}_l$. At this point, it is possible to identify which contractions produces the highest contributions to the potential energy and hence the leading mechanisms of stabilization of a given quasicrystalline phase. The most relevant type of contraction is naturally the one of the form $c(\boldsymbol{0})\, c(\boldsymbol{k}_1)^*\, c(\boldsymbol{0})\, c(-\boldsymbol{k}_1)^*\, \hat{v}(\boldsymbol{k}_1)$ and its equivalents. However, this kind of contraction is present in the energy per particle of all the solutions considered due to their pattern inversion symmetry. The next most relevant contribution, which is only present for solutions with symmetry against rotations of $\pi/3$, are of the type $c(\boldsymbol{0})\, c(\boldsymbol{k}_1)^*\, c(\boldsymbol{k}_1')\, c(\boldsymbol{k}_1' - \boldsymbol{k}_1)^*\, \hat{v}(\boldsymbol{k}_1)$, where the vectors $\boldsymbol{k}_1$ and $\boldsymbol{k}_1'$ are of equal modulus ($|\boldsymbol{k}_1| = |\boldsymbol{k}_1'|$) and form an angle of $\pi/3$ between them. As we can see, this is a contribution combining one zero-momentum Fourier amplitude with three amplitudes corresponding to vectors in the same shell, see Fig. 2(c) for a pictorial representation of the corresponding contraction. In all the tests performed, this kind of term was responsible for around 40% of the total energy of the reduced expansion for the dodecagonal pattern explaining the great stability of this phase in comparison to other quasicrystal so-

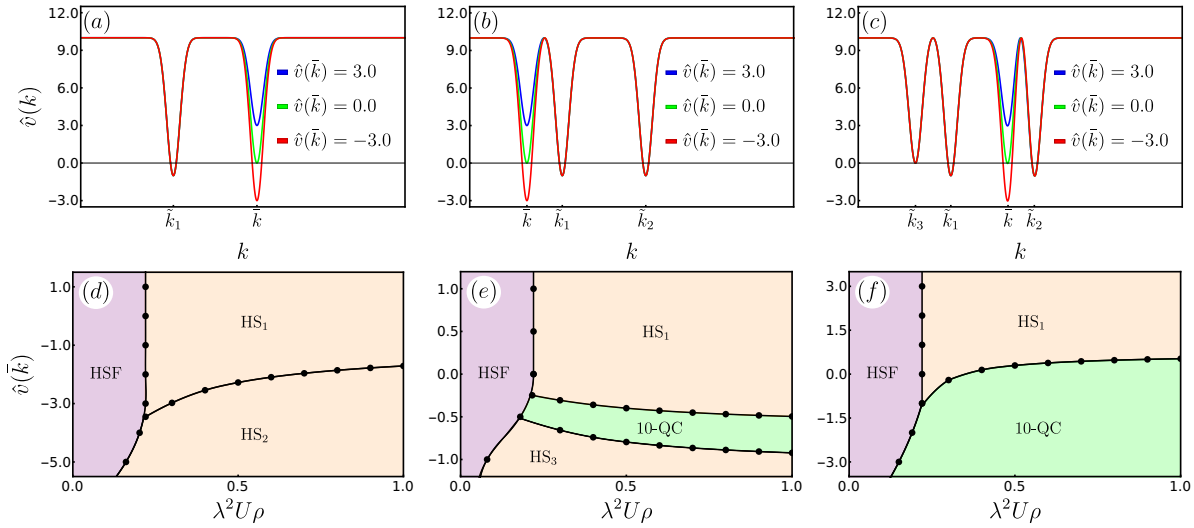

Figure 3. (a)-(c) Pair interaction potential minima structure in Fourier space for the corresponding phase diagrams in (d)-(f), in which the first length scale is positioned at $k = \tilde{k}_1 = 1$ and the secondary resonant scales are determined in Table II. Phase diagram for the minima structure associated with the decagonal quasicrystal where (d) $\bar{k} = \tilde{k}_2$ (e) $\bar{k} = \tilde{k}_3$ and (f) $\bar{k} = \tilde{k}_4$ indicates the position of the minimum in reciprocal space for which we modify the depth as a parameter to determine the ground state of the system. The notation employed to label the phases is analogous to the one established in Fig.1.

lutions that do not contain such interaction terms.

Moreover, we investigate how the superfluid properties of the 12-QC phase are impacted by the properties of the pair interaction potential. We estimate the superfluid fraction by means of the Legget's criterion and consider the scenario posed by Fig. 1(a). The superfluid fraction is calculated across a vertical line of the phase diagram of Fig. 1(d), specifically we consider $\lambda^2 U\rho = 0.50$ and use $\hat{v}(\tilde{k}_2)$ as the running parameter. The results are shown in Fig. 2(d), where the blue points corresponds to the values of the superfluid fraction obtained from the density profile calculated using the mean field spectral variational method while the orange diamonds corresponds to the profile determined via the GPE solution. Within the HS$_1$ phase, for $\hat{v}(\tilde{k}_2) \gtrsim -1.5$, we observe a superfluid fraction essentially constant. This is explained by the fact that Fourier modes with $|\boldsymbol{k}| = \tilde{k}_2$ are not present in the HS$_1$ state when the characteristic wave vector of the pattern is of the order of $\tilde{k}_1$. Moreover, the fact that superfluidity is significant along this phase allows us to conclude that it is actually a supersolid phase. On the other hand, in the region in which the model displays a 12-QC phase, we can notice how the increase of the depth of the second minimum decreases the superfluid fraction. This occurs because decreasing the energy cost of the second minimum promotes higher Fourier amplitudes which implies in a more localized quasicrystalline density pattern, hindering superfluidity in the system. Nonetheless, despite the tendency of the superfluidity, within the quasicrystalline phase its value is still significant, allowing us to confirm that this phase is actually a superfluid dodecagonal phase.

IV. DECAGONAL QUASICRYSTAL

Now we proceed to study the stabilization of the decagonal quasicrystal (10-QC) phase. We explore systematically pair potentials with multiple length scales in the form of several minima in $\hat{v}(k)$, positioned to enhance the stability of this structure. Naturally, the first model to be considered contains two minima, the first one at $k = \tilde{k}_1 = 1$ and the second one at $k = \tilde{k}_2$ (see Table II). The corresponding pair interaction potential is displayed in Fig. 3(a), while the associated ground-state phase diagram is shown in Fig. 3(d). In this case, a phase transition is observed at moderate and high intensity of the pair potential $\lambda^2 U\rho$ as the vertical position of the high momentum minima is varied. For low enough values of $\hat{v}(\tilde{k}_2)$, the system display a transition between two hexagonal solid phases in which the characteristic wave vector of the patterns changes from $\tilde{k}_1$ (HS$_1$) to $\tilde{k}_2$ (HS$_2$). Interestingly, despite the fact that this model produce the excitation of the two main wave vectors of the decagonal quasicrystal, this pair potential configuration is still favorable to the hexagonal structure even when the high momentum minimum dominates. This indicates the necessity of introducing additional minima in $\hat{v}(k)$ to achieve the stabilization of the decagonal quasicrystal pattern.

To proceed we consider the case in which a third minimum in $k = \tilde{k}_3$ (see Table II) is added to a two min-

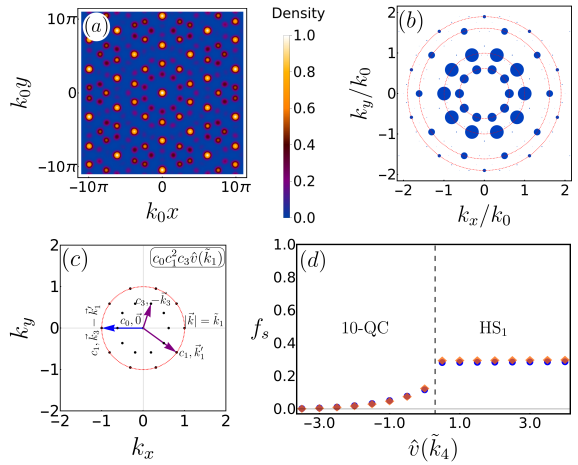

Figure 4. (a) Real space mapping for the decagonal structure in the phase diagram of Fig. 3(f) for parameter values $\hat{v}(\tilde{k}_4) = -1.50$ and $\lambda^2 U\rho = 0.50$ and its corresponding (b) diffraction pattern. The red circles indicates the two minima and the size of the Fourier modes in blue disks is scaled by a linear function, where the zero harmonic mode has been omitted. (c) Most relevant energy contributions to the total energy of the quasicrystalline structures as a contraction in the $k_1 = 1$ layer for the decagonal vectors. (d) Superfluid fraction for a fixed density value $\lambda^2 U\rho = 0.50$ in the decagonal quasicrystal for the ground state depicted in Figure 3(f). The blue points represents the superfluid fraction obtained via mean field spectral variational method while the orange diamonds are determined via GPE simulations.

ima degenerate potential with $\hat{v}(\tilde{k}_1) = \hat{v}(\tilde{k}_2) = -1$. The resulting model for $\hat{v}(k)$ can be observed in Fig. 3(b) and the corresponding ground-state phase diagram using as running parameters the $\hat{v}(\tilde{k}_3)$ and $\lambda^2 U\rho$ is shown in Fig. 3(e). As can be noticed, the introduction of a third characteristic length scale allows the stabilization of a 10-QC phase for a certain range of $\hat{v}(\tilde{k}_3)$. Interestingly, if $\hat{v}(\tilde{k}_3)$ is deep enough the system reenters into a hexagonal phase (HS$_3$) with characteristic wave vector $\tilde{k}_3$. Moreover, the quasicrystal phase exists up to the low intensity potential regime, making the system to present a direct transition from the homogeneous to the quasicrystal phase. However, this behavior is only present in a limited region of $\hat{v}(\tilde{k}_3)$, raising naturally the question about what can be done to enhance further the stability or extension of this phase within the phase diagram.

In order to answer this question, it is natural to consider the introduction of an additional length scale in the form of a minimum in $\hat{v}\,(k)$ at the remaining characteristic wave vector of the decagonal quasicrystalline structure. In this way, we add a minimum at $k = \tilde{k}_4$ (see Table II) to a three minima potential that does not display a quasicrystal phase at any intensity ($\lambda^2 U\rho$) of the pair potential. In terms of minima position, this model satisfy $\hat{v}(\tilde{k}_1) = \hat{v}(\tilde{k}_2) = -1$, $\hat{v}(\tilde{k}_3) = 0$ and $\hat{v}(\tilde{k}_4)$ is taken as running parameter for the construction of the corresponding phase diagram. The typical form of this kind of pair potential is displayed in Fig. 3(c), while in Fig. 3(f) we present the corresponding ground-state phase diagram obtained. As can be observed, when the depth of the fourth minimum at $\tilde{k}_4$ is increased the system transitions from a HS$_1$ to a 10-QC phase. This means that only the addition of this extra minimum promotes the stabilization of the 10-QC phase, but the extension of the quasicrystal phase is greatly enhanced.

To deepen our understanding about the 10-QC phase, we now focus on its structural properties. In Fig. 4(a) and (b), we present a typical density pattern configuration and its corresponding Fourier transform for a pair potential of the type presented in Fig. 3(c) ($\hat{v}(\tilde{k}_4) = -1.50$ and $\lambda^2 U\rho = 0.50$). The radius of each circle in the Fourier transform plot is proportional to the corresponding Fourier amplitude. As we can see, the main modes excited in the density pattern corresponds to those promoted by the minima structure of the pair potential as in the case of the 12-QC phase. An analysis of the potential energy contractions leading to dominant contributions, analogous to the one performed in the case of the dodecagonal structure, reveals that this structure does not have exclusive amplitude contractions which are specially impactful as in the previous case considered. In this case, contractions allowed for all quasicrystal structures, such as the one depicted in Fig. 4(c) for the decagonal pattern, are the leading contribution in the potential energy expansion.

The behavior of the superfluid fraction for the model in Fig. 3(c), keeping $\lambda^2 U\rho = 0.50$ and using $\hat{v}(\tilde{k}_4)$ as our running parameter, is shown in Fig. 4(d). We can observe that within the region corresponding to the HS$_1$ phase, modifying $\hat{v}(\tilde{k}_4)$ does not affect the superfluid fraction. As previously observed, since $\tilde{k}_4$ does not match any resonant momentum of the hexagonal crystal solution with characteristic momentum $\tilde{k}_1$, the hexagonal ground state is not affected by variations of $\hat{v}(\tilde{k}_4)$ and hence neither the superfluid fraction. On the other hand, when the system transitions to the decagonal phase, we observe that making deeper the minimum at $\tilde{k}_4$ results in a decrease of the superfluid fraction. This behavior is a consequence of increasing the stability of the quasicrystalline phase, which results in an increase of the quasicrystal Fourier amplitudes. This in turn reflects on a more localized density profiles which hinder superfluidity. Moreover, is interesting to notice that close to the quasicrystal phase boundary, the superfluid fraction takes significant values, indicating the existence of a superfluid decagonal phase.

V. OCTAGONAL QUASICRYSTAL

Finally, we focus on the study of the stability of the octagonal quasicrystal (8-QC) phase. As in the previous cases, we initially consider a two minima model with a first minimum positioned at $\tilde{k}_1 = 1$ with $\hat{v}(\tilde{k}_1) = -1$ and

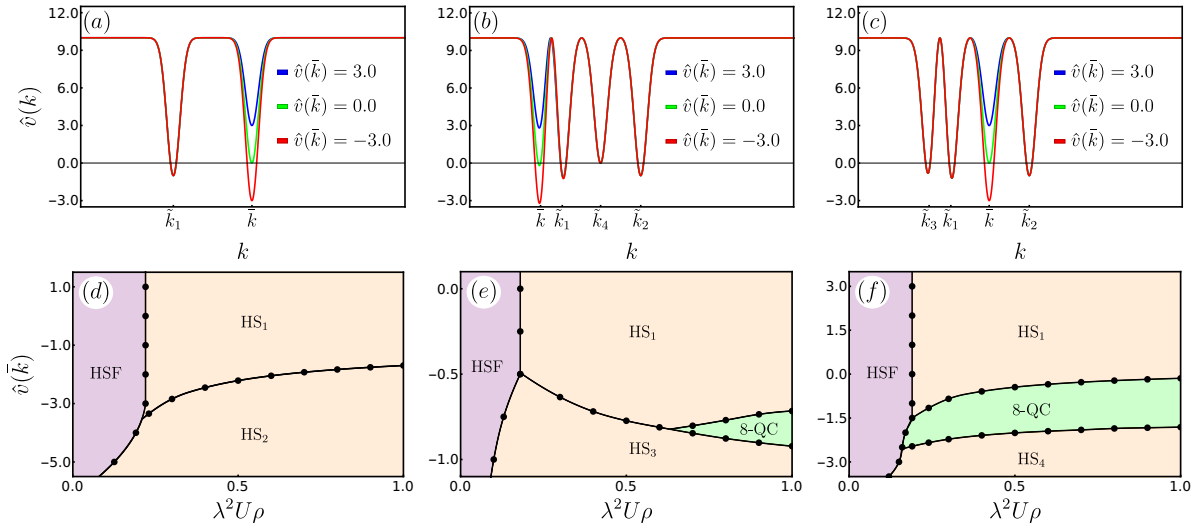

Figure 5. (a)-(c) Pair interaction potential minima structure in Fourier space for the corresponding phase diagrams in (d)-(f), where the first length scale is positioned at $k = \tilde{k}_1 = 1$ and the secondary resonant scales are determined in Table II. Phase diagram for the minima structure associated with the octagonal quasicrystal where (d) $\bar{k} = \tilde{k}_2$ (e) $\bar{k} = \tilde{k}_3$ and (f) $\bar{k} = \tilde{k}_4$ indicates the position of the minimum in reciprocal space for which we modify the depth as a parameter to determine the ground state of the system. The notation employed to label the phases is analogous to the one established in Fig.1.

a second minimum at $\tilde{k}_2$ (see Table II) with a varying vertical position, as it is shown in Fig. 5(a). The resulting phase diagram for this model is shown in Fig. 5(d). The obtained phase diagram presents the trivial homogeneous superfluid phase for low values of $\lambda^2 U\rho$ and a phase transition from a hexagonal phase with characteristic wave vector $\tilde{k}_1$ (HS$_1$) to one with characteristic wave vector $\tilde{k}_2$ (HS$_2$) as $\hat{v}(\tilde{k}_2)$ is decreased. Interestingly, the addition of a third resonant length scale of the 8-QC phase to the pair potential $\hat{v}(k)$, either $k = \tilde{k}_3$ or $k = \tilde{k}_4$, in a scenario with two degenerate minima is not sufficient for the stabilization of the 8-QC phase as occurs in the case of the decagonal pattern, see Fig. 4(e). Even in a scenario without any degeneracy we did not observe the stabilization of the 8-QC pattern using only potentials with three characteristic length scales.

In this way we proceed by allowing the existence of a fourth minimum in $\hat{v}(k)$. Hence, our pair potential potential have local minima at $k = \tilde{k}_1$, $\tilde{k}_2$, $\tilde{k}_3$ and $\tilde{k}_4$, see table II. For this kind of model, we set $\hat{v}(\tilde{k}_1)$ and $\hat{v}(\tilde{k}_2)$ as degenerate minima, while we explore separately the phase diagram varying the vertical position of the other two minima present in $\hat{v}(k)$. Firstly, we set $\hat{v}(\tilde{k}_4) = 0$ and vary the depth of the minimum at $\tilde{k}_3$. The resulting model is presented in Fig. 5(b) and the corresponding phase diagram is shown in Fig. 5(e). Here we observe that in the low $\lambda^2 U\rho$ regime, the system has a similar behavior to the two-minima model presented in Fig. 5(a), with the HS$_3$ phase having characteristic momentum $\tilde{k}_3$. However, for large enough potential intensity we observe the stabilization of an 8-QC in a narrow range of $\hat{v}(\tilde{k}_3)$. Although, strictly speaking the 8-QC exist as the ground state of this model, its stabilization occurs in a region where the validity of the mean field approximation itself can be questioned as the intensity of the pair potential in this region can be hardly considered as weak.

In the last possible scenario, we explore a four-minima interaction potential fixing $\hat{v}(\tilde{k}_3) = -0.6$, a value that in principle favors the formation of the octagonal quasicrystal without turning this minimum the dominant one, see Fig. 5(c). Meanwhile, we use the depth of the minimum at $k = \tilde{k}_4$ as a running parameter for the construction of the phase diagram displayed in Fig. 5(f). As can be observed, this last family of models greatly enhances the stability of the 8-QC phase. This is evident since, in this case, there is a significant range of $\hat{v}(\tilde{k}_4)$ for which we have a direct transition from the homogeneous to the 8-QC phase increasing the potential intensity. Moreover, the system naturally displays a HS$_4$ phase with characteristic momentum close to $\tilde{k}_4$ when the potential minimum at this momentum is deep enough. The systematic study presented allow us to conclude that in order to stabilize the 8-QC phase for the model considered, at least four characteristic wave vectors of this structure should be excited by the pair interaction potential $\hat{v}(k)$. Interestingly, the value of $\hat{v}(\tilde{k}_4)$ seem to have a much stronger impact enhancing stability of the 8-QC than the value of $\hat{v}(\tilde{k}_3)$.

A real space density configuration example and its corresponding Fourier transform plot, for the model in Fig. 5(c), are presented in Fig. 6(a) and (b), respectively.

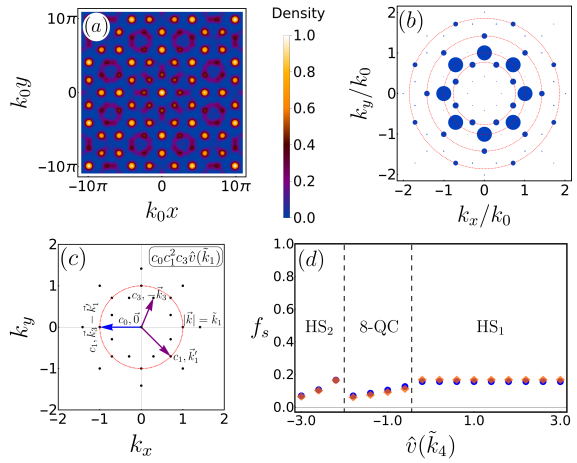

Figure 6. (a) Real space mapping for the octagonal structure in the phase diagram of Fig. 5(f) for parameter values $\hat{v}(\tilde{k}_4) = -1.25$ and $\lambda^2 U\rho = 0.50$ and its corresponding (b) diffraction pattern. The red circles indicates the two minima and the size of the Fourier modes in blue disks is scaled by a linear function, where the zero harmonic mode has been omitted. (c) Most relevant energy contributions to the total energy of the quasicrystalline structures as a contraction in the $\tilde{k}_1 = 1$ layer for the octagonal vectors. (d) Superfluid fraction for a fixed density value $\lambda^2 U\rho = 0.50$ in the octagonal quasicrystal for the ground state depicted in Fig. 5(f). The blue points represents the superfluid fraction obtained via mean field spectral variational method while the orange diamonds are determined via GPE simulations.

The parameters employed for the variational minimization are $\hat{v}(\tilde{k}_4) = -1.25$ and $\lambda^2 U\rho = 0.50$. It is worth noticing how the stabilization of 8-QC phase occurs when all the unstable momenta of the engineered pair potential are excited in the density pattern of the system. Moreover, the investigation of the energy behavior using a reduced Fourier expansion for the 8-QC reveals a scenario similar to the one observed for the 10-QC, where no exclusive form of contraction has a high impact on the energy values and, in this context, only the introduction of additional modes and the eventual emergence of new contractions with higher momentum are effective in the stabilization of the 8-QC phase. We show in Fig. 6(c) an example of the leading contractions for this phase, the specific wave vectors employed for such contractions can switch depending on which is the most unstable wave vector in the system, however preserving the rule of having two modes excited at the most unstable momenta of the system, one at the second most unstable momenta and one with zero momentum.

For completeness, we finally study the behavior of the superfluid fraction for the model described in Fig. 5(c) and Fig. 5(f), using $\hat{v}(\tilde{k}_4)$ as running parameter and fixing $\lambda^2 U\rho = 0.50$. The results obtained are displayed in Fig. 6(d). As previously observed, since the HS$_1$ phase does not excite Fourier modes with momentum $\tilde{k}_4$ or close to it, this phase is unaffected by changes in $\hat{v}(\tilde{k}_4)$. In turn, when the system transition to a phase in which Fourier modes with momentum $\tilde{k}_4$, or close to it, are excited, to decrease the value of $\hat{v}(\tilde{k}_4)$ promote localization of the density pattern, as explained in previous cases. This is the reason for the observed decreasing behavior of the superfluid fraction as we decrease the value of $\hat{v}(\tilde{k}_4)$ for the 8-QC and the HS$_4$ phase, respectively. Moreover, we can notice that as in previous cases, also the 8-QC phase is able to host significant superfluidity confirming the existence of a superfluid octagonal phase.

VI. FINAL REMARKS

In this work, we systematically studied the necessary conditions for the stabilization of eight-, ten- and twelve-fold self-organized quantum quasicrystals. Unlike the classical scenario, we found that quantum quasicrystals with distinct rotational symmetries need pair interaction potentials with a different number of properly selected unstable wave vectors. In the case of the dodecagonal quasicrystal, a two negative minima potential is enough for the stabilization, as previously pointed out in the literature[50]. Meanwhile, the decagonal and octagonal quasicrystal structures need pair interaction potentials with at least three and four minima negative minima properly engineered to be stabilized, respectively. The greater stability of the dodecagonal quasicrystal with respect to other quasicrystalline structures considered resides in the geometric property of having six-fold rotational symmetry. Ultimately, this property is responsible for the existence of Fourier-mode triplets with wave vectors of equal modulus that adds up to zero. As occurs in hexagonal crystals, this feature is responsible for cubic potential energy contributions with a significant impact on decreasing the total energy cost of phases that share this symmetry, see Section III. Moreover, as can be observed in Fig. 1(f), Fig. 3(f) and Fig. 5(f), all quasicrystalline phases studied have a sector in which the superfluid fraction is significant, allowing us to conclude that these are actually super quasicrystal phases. These results were confirmed by extensive Gross-Pitaevskii computations, which produce equivalent configuration and superfluid fraction to those obtained with our variational spectral approach.

We believe that the present results are relevant for the investigation of quasicrystal structures produced in cavity mediated interacting Bose-Einstein condensates[54,57,77,78]. The design on demand of cavity mediated interactions have paved a way to investigate a variety of cutting-edge many-body phases. In this regard, such systems show the interesting opportunity to operate with lattice phononic modes, a flexible manner to test quasicrystals in a quantum framework. At the same time, the

interplay between long-range magnetic and light-induced interactions in a Bose-Einstein condensate[79] is another promising experimental setup that, in principle, should observe 8-QC, 10-QC and 12-QC patterns displaying a finite superfluid signal. Especially relevant is also the usage of dipolar atoms in cavities[60], allowing the implementation of many-body systems with highly tunable interactions capable of producing self-assembled quasicrystal clusters. Here it will be of key importance to inspect the stability of octagonal as well as decagonal phases.

VII. ACKNOWLEDGMENTS

A.M.C. acknowledge UNIFI for financial support and hospitality. This work was supported by the European Union through the Next Generation EU funds through the Italian MUR National Recovery and Resilience Plan, Mission 4 Component 2–Investment 1.4–National Center for HPC, Big Data and Quantum Computing (CUP Grant No. B83C22002830001). F. C. and V. Z. acknowledge financial support from PNRR Ministero Università e Ricerca Project No. PE0000023-NQSTI funded by European Union-Next-Generation EU. The numerical solution of the GPE was performed using the XMDS2 software[80].

[1] T. Neuhaus and C. N. Likos, Journal of Physics: Condensed Matter **23**, 234112 (2011).
[2] F. Cinti, T. Macrì, W. Lechner, G. Pupillo, and T. Pohl, Nature Communications **5**, 3235 (2014).
[3] M. de Mello, R. Díaz-Méndez, and A. Mendoza-Coto, Entropy **25** (2023), 10.3390/e25020356.
[4] A. Mendoza-Coto, D. d. S. Caetano, and R. Díaz-Méndez, Phys. Rev. A **104**, 013301 (2021).
[5] D. Shechtman, I. Blech, D. Gratias, and J. W. Cahn, Phys. Rev. Lett. **53**, 1951 (1984).
[6] M. Engel and H.-R. Trebin, Phys. Rev. Lett. **98**, 225505 (2007).
[7] D. V. Talapin, E. V. Shevchenko, M. I. Bodnarchuk, X. Ye, J. Chen, and C. B. Murray, Nature **461**, 964 (2009).
[8] S. Fischer, A. Exner, K. Zielske, J. Perlich, S. Deloudi, W. Steurer, P. Lindner, and S. Förster, Proceedings of the National Academy of Sciences **108**, 1810 (2011).
[9] N. A. Wasio, R. C. Quardokus, R. P. Forrest, C. S. Lent, S. A. Corcelli, J. A. Christie, K. W. Henderson, and S. A. Kandel, Nature **507**, 86 (2014).
[10] K. Barkan, M. Engel, and R. Lifshitz, Phys. Rev. Lett. **113**, 098304 (2014).
[11] T. Dotera, T. Oshiro, and P. Ziherl, Nature **506**, 208 (2014).
[12] G. Pupillo, P. c. v. Ziherl, and F. Cinti, Phys. Rev. B **101**, 134522 (2020).
[13] A. Mendoza-Coto, R. Turcati, V. Zampronio, R. Díaz-Méndez, T. Macrì, and F. Cinti, Phys. Rev. B **105**, 134521 (2022).
[14] M. Grossklags, M. Ciardi, V. Zampronio, F. Cinti, and A. Mendoza-Coto, Results in Physics **65**, 107991 (2024).
[15] V. Zampronio, A. Mendoza-Coto, T. Macrì, and F. Cinti, Phys. Rev. Lett. **133**, 196001 (2024).
[16] F. Cinti, P. Jain, M. Boninsegni, A. Micheli, P. Zoller, and G. Pupillo, Phys. Rev. Lett. **105**, 135301 (2010).
[17] Y.-C. Zhang, F. Maucher, and T. Pohl, Phys. Rev. Lett. **123**, 015301 (2019).
[18] F. Böttcher, J.-N. Schmidt, M. Wenzel, J. Hertkorn, M. Guo, T. Langen, and T. Pfau, Phys. Rev. X **9**, 011051 (2019).
[19] L. Tanzi, E. Lucioni, F. Famà, J. Catani, A. Fioretti, C. Gabbanini, R. N. Bisset, L. Santos, and G. Modugno, Phys. Rev. Lett. **122**, 130405 (2019).
[20] L. Chomaz, D. Petter, P. Ilzhöfer, G. Natale, A. Trautmann, C. Politi, G. Durastante, R. M. W. van Bijnen, A. Patscheider, M. Sohmen, M. J. Mark, and F. Ferlaino, Phys. Rev. X **9**, 021012 (2019).
[21] P. B. Blakie, D. Baillie, L. Chomaz, and F. Ferlaino, Phys. Rev. Res. **2**, 043318 (2020).
[22] E. Berg, E. Fradkin, E.-A. Kim, S. A. Kivelson, V. Oganesyan, J. M. Tranquada, and S. C. Zhang, Phys. Rev. Lett. **99**, 127003 (2007).
[23] D. G. Barci, A. Mendoza-Coto, and D. A. Stariolo, Phys. Rev. E **88**, 062140 (2013).
[24] A. Mendoza-Coto, D. A. Stariolo, and L. Nicolao, Phys. Rev. Lett. **114**, 116101 (2015).
[25] R. M. W. van Bijnen and T. Pohl, Phys. Rev. Lett. **114**, 243002 (2015).
[26] A. Mendoza-Coto, D. G. Barci, and D. A. Stariolo, Phys. Rev. B **95**, 144209 (2017).
[27] A. Mendoza-Coto, D. E. B. de Oliveira, L. Nicolao, and R. Díaz-Méndez, Phys. Rev. B **101**, 174438 (2020).
[28] L. Radzihovsky, Phys. Rev. Lett. **125**, 267601 (2020).
[29] S. Prestipino and F. Saija, The Journal of Chemical Physics **141**, 184502 (2014).
[30] S. Prestipino, A. Sergi, and E. Bruno, Phys. Rev. B **98**, 104104 (2018).
[31] A. Mendoza-Coto, R. Cenci, G. Pupillo, R. Díaz-Méndez, and E. Babaev, Soft Matter **17**, 915 (2021).
[32] N. Podoliak, P. Salamon, L. Lejček, P. Kužel, and V. Novotná, Phys. Rev. Lett. **131**, 228101 (2023).
[33] J. Xia and Y. Han, Phys. Rev. Res. **6**, 033232 (2024).
[34] A. Mendoza-Coto, V. Mattiello, R. Cenci, N. Defenu, and L. Nicolao, Phys. Rev. B **109**, 064101 (2024).
[35] A. Bianconi, International Journal of Modern Physics B **14**, 3289 (2000).
[36] A. Bianconi, D. Di Castro, N. Saini, and G. Bianconi, "Superstripes," in *Phase Transitions and Self-Organization in Electronic and Molecular Networks*, edited by M. F. Thorpe and J. C. Phillips (Springer US, Boston, MA, 2001) pp. 375–388.
[37] R. Díaz-Méndez, A. Mendoza-Coto, R. Mulet, L. Nicolao, and D. A. Stariolo, The European Physical Journal B **81**, 309 (2011).

[38] R. M. Fernandes, A. V. Chubukov, J. Knolle, I. Eremin, and J. Schmalian, Phys. Rev. B **85**, 024534 (2012).
[39] A. Mendoza-Coto and D. A. Stariolo, Phys. Rev. E **86**, 051130 (2012).
[40] R. M. Fernandes, A. V. Chubukov, and J. Schmalian, Nature Physics **10**, 97 (2014).
[41] A. Mendoza-Coto, O. V. Billoni, S. A. Cannas, and D. A. Stariolo, Phys. Rev. B **94**, 054404 (2016).
[42] A. Mendoza-Coto, L. Nicolao, and R. Díaz-Méndez, Scientific Reports **9**, 2020 (2019).
[43] D. Levine and P. J. Steinhardt, Phys. Rev. B **34**, 596 (1986).
[44] J. E. S. Socolar, T. C. Lubensky, and P. J. Steinhardt, Phys. Rev. B **34**, 3345 (1986).
[45] R. Lifshitz, Israel Journal of Chemistry **51**, 1156 (2011).
[46] X. Zeng, G. Ungar, Y. Liu, V. Percec, A. E. Dulcey, and J. K. Hobbs, Nature **428**, 157 (2004).
[47] T. Dotera, Israel Journal of Chemistry **51**, 1197 (2011).
[48] K. Jiang, P. Zhang, and A.-C. Shi, Journal of Physics: Condensed Matter **29**, 124003 (2017).
[49] M. Ciardi, A. Angelone, F. Mezzacapo, and F. Cinti, Phys. Rev. Lett. **131**, 173402 (2023).
[50] V. Heinonen, K. J. Burns, and J. Dunkel, Phys. Rev. A **99**, 063621 (2019).
[51] S. Gopalakrishnan, B. L. Lev, and P. M. Goldbart, Nature Physics **5**, 845 (2009).
[52] S. Gopalakrishnan, B. L. Lev, and P. M. Goldbart, Phys. Rev. A **82**, 043612 (2010).
[53] V. D. Vaidya, Y. Guo, R. M. Kroeze, K. E. Ballantine, A. J. Kollár, J. Keeling, and B. L. Lev, Phys. Rev. X **8**, 011002 (2018).
[54] T. D. Farokh Mivehvar, Francesco Piazza and H. Ritsch, Advances in Physics **70**, 1 (2021).
[55] Y.-C. Zhang, V. Walther, and T. Pohl, Phys. Rev. A **103**, 023308 (2021).
[56] P. Karpov and F. Piazza, Phys. Rev. Lett. **128**, 103201 (2022).
[57] F. Mivehvar, H. Ritsch, and F. Piazza, Phys. Rev. Lett. **123**, 210604 (2019).
[58] Y. Guo, R. M. Kroeze, V. D. Vaidya, J. Keeling, and B. L. Lev, Phys. Rev. Lett. **122**, 193601 (2019).
[59] Y. Guo, R. M. Kroeze, B. P. Marsh, S. Gopalakrishnan, J. Keeling, and B. L. Lev, Nature **599**, 211 (2021).
[60] M. Bonifacio, F. Piazza, and T. Donner, PRX Quantum **5**, 040332 (2024).
[61] K. Baumann, C. Guerlin, F. Brennecke, and T. Esslinger, Nature **464**, 1301 (2010).
[62] J. Klinder, H. Keßler, M. Wolke, L. Mathey, and A. Hemmerich, Proceedings of the National Academy of Sciences **112**, 3290 (2015).
[63] F. Mivehvar, H. Ritsch, and F. Piazza, Phys. Rev. Lett. **122**, 113603 (2019).
[64] J. Klinder, H. Keßler, M. R. Bakhtiari, M. Thorwart, and A. Hemmerich, Phys. Rev. Lett. **115**, 230403 (2015).
[65] R. Landig, L. Hruby, N. Dogra, M. Landini, R. Mottl, T. Donner, and T. Esslinger, Nature **532**, 476 (2016).
[66] D. Lima, M. Grossklags, V. Zampronio, F. Cinti, and A. Mendoza-Coto, "Supersolid dipolar phases in planar geometry: effects of tilted polarization," (2025), arXiv:2501.09641 [cond-mat.quant-gas].
[67] R. Lifshitz and D. M. Petrich, Phys. Rev. Lett. **79**, 1261 (1997).
[68] K. Jiang, J. Tong, and P. Zhang, Communications in Computational Physics **19**, 559 (2016).
[69] J. Yin, K. Jiang, A.-C. Shi, P. Zhang, and L. Zhang, Proceedings of the National Academy of Sciences **118**, e2106230118 (2021).
[70] S. Prestipino, A. Sergi, and E. Bruno, Journal of Physics A: Mathematical and Theoretical **52**, 015002 (2018).
[71] A. J. Leggett, Phys. Rev. Lett. **25**, 1543 (1970).
[72] A. J. Leggett, Journal of Statistical Physics **93**, 927 (1998).
[73] P. B. Blakie, Journal of Physics B: Atomic, Molecular and Optical Physics **57**, 115301 (2024).
[74] R. Gautier, H. Yao, and L. Sanchez-Palencia, Phys. Rev. Lett. **126**, 110401 (2021).
[75] L. P. Pitaevskii, Sov. Phys. JETP **13**, 451 (1961).
[76] E. P. Gross, Journal of Mathematical Physics **4**, 195 (1963).
[77] N. Masalaeva, H. Ritsch, and F. Mivehvar, Phys. Rev. Lett. **131**, 173401 (2023).
[78] F. Orsi, N. Sauerwein, R. P. Bhatt, J. Faltinath, E. Fedotova, N. Reiter, T. Cantat-Moltrecht, and J.-P. Brantut, PRX Quantum **5**, 040333 (2024).
[79] C. Mishra, S. Ostermann, F. Mivehvar, and B. P. Venkatesh, Phys. Rev. A **107**, 023312 (2023).
[80] G. R. Dennis, J. J. Hope, and M. T. Johnsson, Computer Physics Communications **184**, 201 (2013).

Parte II

Conclusions and perspectives

4 Conclusions

In our study *Supersolid dipolar phases in planar geometry: effects of tilted polarization*, the identification of key characteristics in these periodic structures enabled a Fourier mode-based representation of supersolids. To accurately capture the quantitative behavior of the energy per particle of a modulated ground-state, we developed a generalized harmonic expansion method for modulated structures. By employing symmetry arguments, we expressed the energy of each pattern solely in terms of independent harmonic modes, significantly improving computational efficiency in analysing the models of interest.

To determine the phase diagram, we minimized the energy per particle of each modulated pattern as a function of the variational parameters, and this allowed us to characterize the ground-state behavior with the lowest energy. We further validated our results by computing a phase diagram using an ansatz with an extended Fourier basis. Our analysis confirms that the critical boundary between stripe and homogeneous phases remains robust, while the precise locations of the critical and triple points exhibit minor shifts.

We explored a comparatively simple yet hitherto unexplored configuration: a quasi-two-dimensional, planar dipolar Bose gas with a tilted polarization axis. Our results demonstrate that tilting the polarization has a profound impact on the system's quantum critical behavior compared to the well-studied perpendicular case. As the polarization angle deviates from the normal direction, the single quantum critical point present at $\alpha = 0$ splits into three distinct critical lines, each separating two phases. Beyond altering the critical structure, a tilted polarization also induces significant structural changes in the modulated phases. Specifically, the hexagonal and honeycomb phases develop marked axial anisotropy. We find that this anisotropy enhances superfluid transport along the favored in-plane polarization axis while suppressing it in the perpendicular direction. This effect provides a promising mechanism for controlling the superfluid response in dipolar supersolids, which are otherwise isotropic when $\alpha = 0$.

It is important to note that while the physics of strictly two-dimensional dipolar systems with tilted polarization has been extensively studied, the behavior of their quasi-two-dimensional counterparts is fundamentally different and remains largely unexplored. Only recently has the ground-state phase diagram for quasi-2D systems with perpendicular polarization been established; the case of tilted polarization, as studied here, is entirely novel.

Finally, we address the experimental feasibility of our results. For instance, using ^{162}Dy (with a dipolar length $a_{dd} \approx 131a_0 \approx 7$ nm), the range of s-wave scattering lengths

a_s and ratios a_s/a_{dd} required are readily achievable. The characteristic units for ^{162}Dy are length $\ell = 0.26$ μm and time $t_0 = 0.18$ ms. A dimensionless trapping frequency $\omega_z t_0 = 0.08$ then corresponds to $\omega_z \approx 450$ Hz. As a concrete example, with parameters $a_s/a_{dd} = 0.755$, $\rho = 120$, and $\alpha = 30°$. For this case, we find a width $\sigma \approx 6.78$ μm and a peak 3D density at the mid-plane of $3\rho/4\sigma \approx 1.9 \times 10^{14}\text{cm}^{-3}$. The characteristic wave vector of the compressed hexagonal solid is $k_0 \approx 0.4$ μm^{-1}, yielding lattice spacings of $D_x = 4\pi \tan(\theta)/k_0 \approx 4.59$ μm and $D_d = 2\pi \sec(\theta)/k_0 \approx 4.75$ μm. These length scales are sufficiently large to facilitate the experimental observation of long-distance physical properties.

In the work *Engineering interaction potentials for stabilizing quantum quasicrystal phases*, proceeding with a similar variational approach to minimize the energy per particle functional, we have systematically investigated the minimal ingredients required to stabilize octagonal (8-fold), decagonal (10-fold) and dodecagonal (12-fold) self-organized quantum quasicrystals in a bosonic condensate. Using an experimentally motivated, multi-well effective pair interaction in momentum space (relevant to cavity QED and laser-painted interaction platforms), we constructed sequences of pair potentials that progressively excite the characteristic wave-vector sets of each quasicrystalline structure and computed the corresponding ground-state phase diagrams.

Across all cases the diagrams display a homogeneous phase at low values of the control parameter $\lambda^2\rho U$, while intermediate and large $\lambda^2\rho U$ produce sequences of modulated phases as the relative energetic cost of exciting each characteristic Fourier mode is varied. The variational spectral approach used to construct and analyze the phases is corroborated by extensive Gross–Pitaevskii simulations, which recover equivalent configurations and superfluid fractions.

We found, as a central result, that distinct quantum quasicrystals require pair potentials with different numbers of carefully chosen unstable wave vectors. The quantum stabilization of the dodecagonal quasicrystal can be achieved with a two-minima potential, whereas decagonal and octagonal quasicrystals require at least three and four tailored minima, respectively. The enhanced robustness of the 12-fold pattern is traced to a geometric property of its wave-vector lattice: the existence of triplets of equal-modulus vectors that sum to zero. Those triplets enable cubic (three-mode) contractions in the interaction energy that substantially lower the total energy of phases sharing this symmetry, analogous to mechanisms that stabilize hexagonal order.

Thus, in summary, this work clarifies the minimal momentum-space interaction features necessary to realize quantum quasicrystalline order in Bose–Einstein condensates, and highlights a symmetry-driven mechanism that favors 12-fold order, and establishes that these exotic spatially ordered phases generically coexist with superfluidity, opening a coherent path toward their observation in cavity experiments.

These findings are directly relevant to ongoing and near-term experiments. Cavity-

mediated and laser-engineered interactions provide flexible routes to design the required multi-well momentum-space potentials. Such a platform could explore the predicted 8-, 10-, and 12-fold self-organized patterns in BECs.

Credit authorship contribution statement

Supersolid dipolar phases in planar geometry: effects of tilted polarization: using the commercial software Mathematica, I performed functional minimization to find the most energetically favorable quantum phase for a given set of parameters, as well as computed the superfluidity and contrast. After assembling several sequential cases, as well as applying a bisection algorithm, I discovered the transition lines, their critical and triple points. I also validate the computation by computing cases with a large Fourier basis. All computations were time-demanding, and I had to manage the computational resources as well.

Engineering interaction potentials for stabilizing quantum quasicrystal phases: I was concentrated on discovering the most energetically favorable quantum phases by performing functional minimization with a huge set of variational parameters. This was accomplished by carefully adding variational parameters at each step in a sequence of functional minimizations. In the end, as a result, a functional minimization with a huge quantity of variational parameters is performed. I formatted all the phases and physical quantities of interest, and made it available to a cloud service for my colleagues to build the phase diagram.

APPENDIX A – The dipolar Bose gas

Dipolar condensates can be made of electric or magnetic dipoles, thus, this section addresses briefly a recapitulation on the dipolar potential, as well as the corresponding LHY correction that will be used.

A.1 Dipole-Dipole Interaction

The interaction potential $V(\mathbf{r})$ between two identical electric or magnetic dipoles separated by a relative position vector $\mathbf{r}$ is expressed as [93]:

$$V(\mathbf{r}) = \frac{C_{dd}}{4\pi}\frac{(\mathbf{e}_1 \cdot \mathbf{e}_2)r^2 - 3(\mathbf{e}_1 \cdot \mathbf{r})(\mathbf{e}_2 \cdot \mathbf{r})}{r^5}, \tag{A.1}$$

where C_{dd} defines the coupling strength. For magnetic dipoles with moment μ, $C_{dd} = \mu_0\mu^2$ (μ_0: vacuum permeability), while for electric dipoles with moment d, $C_{dd} = d^2/\varepsilon_0$ (ε_0: vacuum permittivity). In this work, as in most modern studies, the dipoles are aligned along a common axis via an external magnetic field. Choosing this polarization direction as the z-axis simplifies Eq. (A.1) to:

$$V_{dd}(\mathbf{r}) = \frac{C_{dd}}{4\pi}\frac{1 - 3\cos^2\theta}{r^3}, \tag{A.2}$$

where θ is the angle between $\mathbf{r}$ and the z-axis (Figure 2.1). This potential exhibits two key features: (i) a long-range r^{-3} decay, contrasting with the short-range r^{-6} van der Waals interaction, and (ii) anisotropy governed by θ. For fixed r, $V_{dd}(\mathbf{r})$ varies from a minimum of $-\frac{C_{dd}}{2\pi r^3}$ (attractive) at $\theta = 0$ (head-to-tail alignment) to a maximum of $\frac{C_{dd}}{4\pi r^3}$ (repulsive) at $\theta = \pi/2$ (side-by-side alignment). The interaction vanishes at $\theta_0 = \arccos(1/\sqrt{3}) \approx 54.7°$. Due to the periodicity of $\cos^2\theta$, attraction occurs for $|\theta| < \theta_0$ or $\theta_0 + \pi/2 < \theta < \theta_0 + \pi$, and repulsion otherwise. This angular dependence drives dipoles to favor low-energy head-to-tail configurations, profoundly affecting the stability of dipolar Bose-Einstein condensates (BECs). To characterize the interaction strength, the *dipolar length* a_{dd} is defined as:

$$a_{dd} = \frac{C_{dd}m}{12\pi\hbar^2}, \tag{A.3}$$

where m is the particle mass. This parameter quantifies the relative influence of dipole-dipole interactions compared to kinetic energy scales.

A.2 Comparative Analysis of Dipolar Lengths

The dipolar length a_{dd} serves as a universal metric for comparing electric and magnetic dipole strengths (Table 1 taken from [94]). Notably, electric dipoles (e.g., polar

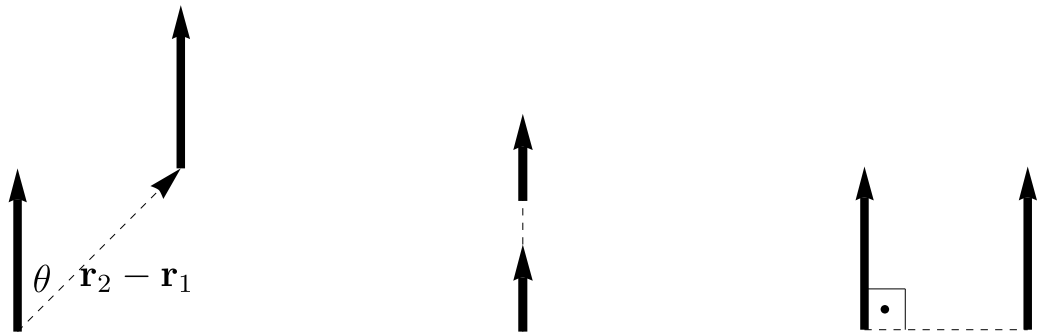

(a) (b) Attractive (c) Repulsive

Figure 16 – Anisotropy of the dipole-dipole interaction. (a) Geometry of two aligned dipoles separated by $\mathbf{r}$, with θ denoting the angle relative to the polarization axis z. (b) Attractive interaction in the head-to-tail configuration ($\theta = 0$). (c) Repulsive interaction in the side-by-side configuration ($\theta = \pi/2$). Source: created by the author.

Species	**Dipole Moment**	$\boldsymbol{a_{dd}}$
^{52}Cr	$6\mu_B$	$15a_0$
^{164}Dy	$9.9\mu_B$	$130a_0$
^{166}Er	$7\mu_B$	$65.5a_0$
KRb	$0.6D$	$2 \times 10^3 a_0$

Table 1 – Dipolar lengths a_{dd} for species achieving quantum degeneracy. Magnetic bosonic atoms (^{52}Cr, ^{164}Dy, ^{166}Er) form BECs, while fermionic polar molecules (KRb) exhibit Fermi degeneracy. μ_B: Bohr magneton; a_0: Bohr radius.

molecules like KRb) exhibit a_{dd} values orders of magnitude larger than magnetic dipoles (e.g., atoms like ^{52}Cr or ^{164}Dy), making them theoretically ideal for observing dipolar effects. However, experimental limitations—such as complex cooling techniques—have restricted the quantum degenerate regime of polar molecules to fermionic systems [95]. In contrast, magnetic atoms readily form BECs, enabling robust studies of dipolar physics despite weaker interactions. This thesis focuses on magnetic BECs, where the interplay between magnetic dipole-dipole forces and contact interactions underpins novel quantum phenomena.

APPENDIX B – The supersolid in a slowly moving frame

To analyse the superfluid behaviour, we examine our system under the assumption of hypothetical boundaries moving at velocity v relative to the laboratory frame. These moving boundaries result from an infinitesimal irregularity in the confinement potential, which does not perturb the system's state except by establishing the reference frame for the normal component. Consequently, the case of a periodic density (coupled to the zero-temperature normal component) shifts at velocity v. The central point is that, at equilibrium, only the normal component responds to the moving boundaries, leaving the superfluid undisturbed. This low-speed behaviour can be described by the expectation value of the total linear momentum operator, $-i\hbar\nabla$, in the frame of the laboratory

$$\lim_{v\to 0} P_i(\mathbf{v}) = M\sum_j(\delta_{ij} - f_{ij})v_j, \tag{B.1}$$

where M is the total mass, and f_{ij} is the superfluid fraction that might decrease the mechanical response in the ij-direction. Therefore, when $f_{ij} \to 1$, in the case of a pure superfluid, the system remains stationary in the laboratory frame (yielding P = 0). Conversely, when $f_{ij} = 0$, the system behaves as a normal fluid with $\mathbf{P} = M\mathbf{v}$.

The ground state in the co-moving frame is determined by solving the time-independent Gross-Pitaevskii equation (GPE) for the wave function in the co-moving frame, which is obtained by a Galilean transformation $\mathbf{x}' = \mathbf{x} - \mathbf{v}t$:

$$\psi(\mathbf{x}, t) = \tilde{\psi}(\mathbf{x}', t), \tag{B.2}$$

whose equation

$$\mu_{\mathbf{v}}\tilde{\psi}_{\mathbf{v}} = \mathcal{L}_{\mathrm{GP}}\tilde{\psi}_{\mathbf{v}} + i\hbar\mathbf{v}\cdot\nabla'\tilde{\psi}_{\mathbf{v}}, \tag{B.3}$$

where the operator ∇' differentiates primed spatial coordinates. Let ψ_0 be the stationary solution for $\mathbf{v} = 0$. For small velocity v, approximately, the new spatially periodic wave solution is postulated to be

$$\tilde{\psi}_{\mathbf{v}}(\mathbf{x}') \approx \psi_0(\mathbf{x}')e^{i\phi_1(\mathbf{x}')}. \tag{B.4}$$

where ϕ_1 represents the first-order phase correction. Then, when computing the probability current[1], and neglecting spatial derivatives of the density $\rho_0 = |\psi_0|^2$, for the density of

[1] $\mathbf{j} = \dfrac{\hbar}{2mi}(\psi^*\nabla\psi - \psi\nabla\psi^*)$, and the conservation law for the density of probability ρ, $\dfrac{\partial\rho}{\partial t} + \nabla\cdot\mathbf{j} = 0$.

probability $\rho_0 = |\psi_0|^2$ one has that

$$\mathbf{j}(\mathbf{x}') = \rho_0(\mathbf{x}') \left(\frac{\hbar}{m} \nabla' \phi_1 - \mathbf{v} \right). \tag{B.5}$$

As $\partial|\psi|^2/\partial t = 0$, because $\psi(\mathbf{x}', t)$ is a stationary state, the condition $\nabla \cdot \mathbf{j} = 0$ is imposed, guaranteeing that the density remains stationary in the moving frame (i.e., the crystal moves with the frame). Applying this condition, non-trivial solutions for the flow field exist in higher dimensions, found by solving

$$\frac{\hbar}{m} \nabla \cdot (\rho_0 \nabla \phi_1) = \mathbf{v} \cdot \nabla \rho_0. \tag{B.6}$$

In the context of estimating the superfluid fraction of solid ^{4}He, in the Ref. [96], the same equation was obtained in the reciprocal space. The expectation value of the linear momentum operator, in the frame of the laboratory, is

$$\mathbf{P}(\mathbf{v}) = \hbar \int d\mathbf{r}' \rho_0 \nabla \phi_1, \tag{B.7}$$

which is not always aligned in the direction of $\mathbf{v}$.

The solution of the Eq. (B.6) is computed by using an auxiliary vector field $\mathbf{K}$ as

$$\phi_1(\mathbf{r}') = \frac{m}{\hbar} \mathbf{v} \cdot \mathbf{K}(\mathbf{r}'), \tag{B.8}$$

then, substituting in the Eq. (B.6), the equation to be solved is

$$\nabla \cdot (\rho_0 \nabla K_i) = \frac{\partial \rho_0}{\partial x_i'}, \quad (i = \{x, y\}) \tag{B.9}$$

and, consequently, the momentum in the frame of the laboratory is

$$\mathbf{P}(\mathbf{v}) = m \int d\mathbf{r}' \rho_0 \nabla (\mathbf{v} \cdot \mathbf{K}). \tag{B.10}$$

Thus, inserting Eq. (B.10) into Eq. (B.1), the superfluid fraction can be computed with partial derivatives

$$f_{ij} = \delta_{ij} - \frac{1}{m} \frac{\partial P_i}{\partial v_j} = \delta_{ij} - \frac{1}{N} \int d\mathbf{r}' \rho_0 \frac{\partial K_j}{\partial x_i'}. \tag{B.11}$$

References

1 ALLEN, J. New Phenomena Connected with Heat Flow in Helium II. Nature, v. 141, p. 243–244, 938.

2 LANDAU, L. Theory of the superfluidity of Helium II. Physical Review, American Physical Society, v. 60, p. 356, Aug 1941.

3 TISZA, L. Transport phenomena in Helium II. Nature, American Physical Society, v. 141, p. 913, May 1938.

4 ANDERSON, M. H. et al. Observation of bose-einstein condensation in a dilute atomic vapor. Science, American Association for the Advancement of Science (AAAS), v. 269, n. 5221, p. 198–201, jul. 1995. Disponível em: <https://doi.org/10.1126/science.269.5221.198>.

5 PRESTIPINO, S.; SAIJA, F.; GIAQUINTA, P. V. Hexatic phase in the two-dimensional gaussian-core model. Phys. Rev. Lett., American Physical Society, v. 106, p. 235701, Jun 2011. Disponível em: <https://link.aps.org/doi/10.1103/PhysRevLett.106.235701>.

6 PRESTIPINO, S.; SAIJA, F. Hexatic phase and cluster crystals of two-dimensional gem4 spheres. The Journal of Chemical Physics, v. 141, n. 18, p. 184502, 11 2014. ISSN 0021-9606. Disponível em: <https://doi.org/10.1063/1.4901302>.

7 KROISS, P.; BONINSEGNI, M.; POLLET, L. Ground-state phase diagram of gaussian-core bosons in two dimensions. Phys. Rev. B, American Physical Society, v. 93, p. 174520, May 2016. Disponível em: <https://link.aps.org/doi/10.1103/PhysRevB.93.174520>.

8 CINTI, F. et al. Defect-induced supersolidity with soft-core bosons. Nat. Commun., v. 5, n. 1, p. 3235, Feb 2014. ISSN 2041-1723. Disponível em: <https://doi.org/10.1038/ncomms4235>.

9 BLAND, T. et al. Two-dimensional supersolid formation in dipolar condensates. Phys. Rev. Lett., American Physical Society, v. 128, p. 195302, May 2022. Disponível em: <https://link.aps.org/doi/10.1103/PhysRevLett.128.195302>.

10 RIPLEY, B. T. E.; BAILLIE, D.; BLAKIE, P. B. Two-dimensional supersolidity in a planar dipolar bose gas. Phys. Rev. A, American Physical Society, v. 108, p. 053321, Nov 2023. Disponível em: <https://link.aps.org/doi/10.1103/PhysRevA.108.053321>.

11 STAUDINGER, C. et al. Striped dilute liquid of dipolar bosons in two dimensions. Physical Review A, American Physical Society (APS), v. 108, n. 3, set. 2023. ISSN 2469-9934. Disponível em: <http://dx.doi.org/10.1103/PhysRevA.108.033303>.

12 BLAKIE, P. B. et al. Supersolidity in an elongated dipolar condensate. Phys. Rev. Res., American Physical Society, v. 2, p. 043318, Dec 2020. Disponível em: <https://link.aps.org/doi/10.1103/PhysRevResearch.2.043318>.

13 BARKAN, K.; ENGEL, M.; LIFSHITZ, R. Controlled self-assembly of periodic and aperiodic cluster crystals. Phys. Rev. Lett., American Physical Society, v. 113, p. 098304, Aug 2014. Disponível em: <https://link.aps.org/doi/10.1103/PhysRevLett.113.098304>.

14 PUPILLO, G.; ZIHERL, P. c. v.; CINTI, F. Quantum cluster quasicrystals. Phys. Rev. B, American Physical Society, v. 101, p. 134522, Apr 2020. Disponível em: <https://link.aps.org/doi/10.1103/PhysRevB.101.134522>.

15 MENDOZA-COTO, A. et al. Exploring quantum quasicrystal patterns: A variational study. Phys. Rev. B, American Physical Society, v. 105, p. 134521, Apr 2022. Disponível em: <https://link.aps.org/doi/10.1103/PhysRevB.105.134521>.

16 BONIFACIO, M.; PIAZZA, F.; DONNER, T. Laser-painted cavity-mediated interactions in a quantum gas. PRX Quantum, American Physical Society, v. 5, p. 040332, Dec 2024. Disponível em: <https://link.aps.org/doi/10.1103/PRXQuantum.5.040332>.

17 TAYLOR, C. The Atomists Leucippus and Democritus. [S.l.]: University of Toronto Press, 1999.

18 EINSTEIN, A. Quantentheorie des einatomigen idealen Gases. Sitzber. Kgl. Preuss. Akad. Wiss., v. 261, 1924.

19 BOSE, N. Planck's Law and Light Quantum Hypothesis. Z. Phys., v. 26, p. 178, 1924.

20 KAPITZA, P. Viscosity of liquid Helium below the λ-point. Nature, American Physical Society, v. 141, p. 74, Jan 1938.

21 ALLEN, J.; MISENER, A. Viscosity of liquid Helium below the λ-point. Nature, American Physical Society, v. 141, p. 75, Jan 1938.

22 AMIGÓ, M. L. et al. A quantitative experiment on the fountain effect in superfluid helium. European Journal of Physics, IOP Publishing, v. 38, n. 5, p. 055103, aug 2017. Disponível em: <https://doi.org/10.1088/1361-6404/aa818c>.

23 FABROCINI, A.; FANTONI, S.; KROTSCHECK, K. Intorduction to Modern Methods of Quatum Many-Body Theory and Their Applications. [S.l.]: World Scientific Publishing Co. Pte. Ltd, 2002.

24 BOSE, N. The superconductivity of mercury. Commun. Phys. Lab. Univ.Leiden, p. 1, 1911.

25 BARDEEN, J.; COOPER, L. N.; SCHRIEFFER, J. R. Theory of superconductivity. Phys. Rev., American Physical Society, v. 108, p. 1175–1204, Dec 1957. Disponível em: <https://link.aps.org/doi/10.1103/PhysRev.108.1175>.

26 LANDAU, L. D. On the theory of phase transitions. Zh. Eksp. Teor. Fiz., v. 7, p. 19–32, 1937.

27 MARINO, E. C. Quantum Field Theory Approach to Condensed Matter Physics. [S.l.]: Cambridge University Press, 2017.

28 HIGGS, P. W. Broken symmetries and the masses of gauge bosons. Phys. Rev. Lett., American Physical Society, v. 13, p. 508–509, Oct 1964. Disponível em: <https://link.aps.org/doi/10.1103/PhysRevLett.13.508>.

29 ENGLERT, F.; BROUT, R. Broken symmetry and the mass of gauge vector mesons. Phys. Rev. Lett., American Physical Society, v. 13, p. 321–323, Aug 1964. Disponível em: <https://link.aps.org/doi/10.1103/PhysRevLett.13.321>.

30 SORNETTE, D. Stock market speculation: Spontaneous symmetry breaking of economic valuation. Physica A: Statistical Mechanics and its Applications, v. 284, n. 1, p. 355–375, 2000. ISSN 0378-4371. Disponível em: <https://www.sciencedirect.com/science/article/pii/S0378437100002612>.

31 PITAEVSKII, L.; STRINGARI, S. Bose-Einstein Condensation and Superfluidity. Oxford University Press, 2016. ISBN 9780198758884. Disponível em: <https://doi.org/10.1093/acprof:oso/9780198758884.001.0001>.

32 NELSON, D. R. Defects and Geometry in Condensed Matter Physics. Cambridge: Cambridge University Press, 2002. ISBN 9780521004008.

33 LIKOS, C. N. et al. Why do ultrasoft repulsive particles cluster and crystallize? analytical results from density-functional theory. The Journal of Chemical Physics, AIP Publishing, v. 126, n. 22, jun. 2007. ISSN 1089-7690. Disponível em: <http://dx.doi.org/10.1063/1.2738064>.

34 LIKOS, C. N. et al. Criterion for determining clustering versus reentrant melting behavior for bounded interaction potentials. Phys. Rev. E, American Physical Society, v. 63, p. 031206, Feb 2001. Disponível em: <https://link.aps.org/doi/10.1103/PhysRevE.63.031206>.

35 NEPOMNYASHCHII, Y. A. Coherent crystals with one-dimensional and cubic lattices. Theoretical and Mathematical Physics, v. 8, n. 3, p. 928–938, 1971. ISSN 1573-9333. Disponível em: <https://doi.org/10.1007/BF01029350>.

36 NEPOMNYASHCHII, Y. A.; NEPOMNYASHCHII, A. A. Collective spectrum of coherent crystals. Theoretical and Mathematical Physics, v. 9, n. 1, p. 1033–1041, 1971. ISSN 1573-9333. Disponível em: <https://doi.org/10.1007/BF01036033>.

37 JOSSERAND, C.; POMEAU, Y.; RICA, S. Coexistence of ordinary elasticity and superfluidity in a model of a defect-free supersolid. Phys. Rev. Lett., American Physical Society, v. 98, p. 195301, May 2007. Disponível em: <https://link.aps.org/doi/10.1103/PhysRevLett.98.195301>.

38 MERMIN, N. D.; WAGNER, H. Absence of ferromagnetism or antiferromagnetism in one- or two-dimensional isotropic heisenberg models. Phys. Rev. Lett., American Physical Society, v. 17, p. 1133–1136, Nov 1966. Disponível em: <https://link.aps.org/doi/10.1103/PhysRevLett.17.1133>.

39 WAGNER, H. Long-wavelength excitations and the goldstone theorem in many-particle systems with “broken symmetries”. Zeitschrift für Physik, v. 195, n. 3, p. 273–299, 1966. ISSN 0044-3328. Disponível em: <https://doi.org/10.1007/BF01325630>.

40 HALPERIN, B. I.; NELSON, D. R. Theory of two-dimensional melting. Phys. Rev. Lett., American Physical Society, v. 41, p. 121–124, Jul 1978. Disponível em: <https://link.aps.org/doi/10.1103/PhysRevLett.41.121>.

41 KOSTERLITZ, J. M.; THOULESS, D. J. Ordering, metastability and phase transitions in two-dimensional systems. Journal of Physics C: Solid State Physics, v. 6, n. 7, p. 1181, apr 1973. Disponível em: <https://dx.doi.org/10.1088/0022-3719/6/7/010>.

42 YOUNG, A. P. Melting and the vector coulomb gas in two dimensions. Phys. Rev. B, American Physical Society, v. 19, p. 1855–1866, Feb 1979. Disponível em: <https://link.aps.org/doi/10.1103/PhysRevB.19.1855>.

43 PRESTIPINO, S.; SAIJA, F. Hexatic phase and cluster crystals of two-dimensional gem4 spheres. The Journal of Chemical Physics, v. 141, n. 18, p. 184502, 11 2014. ISSN 0021-9606. Disponível em: <https://doi.org/10.1063/1.4901302>.

44 BOGOLIUBOV, N. N. On the theory of superfluidity. J. Phys. (USSR), v. 11, p. 23, 1947. Izv. Akad. Nauk Ser. Fiz. 11, p. 77 (1947).

45 SANKOVICH, D. P. Bogolyubov's theory of superfluidity. Physics of Particles and Nuclei, v. 41, n. 7, p. 1068–1070, dez. 2010.

46 YANG, C. N. Concept of off-diagonal long-range order and the quantum phases of liquid he and of superconductors. Rev. Mod. Phys., American Physical Society, v. 34, p. 694–704, Oct 1962. Disponível em: <https://link.aps.org/doi/10.1103/RevModPhys.34.694>.

47 SCHMITT, A. Introduction to superfluidity – Field-theoretical approach and applications. 2014. Disponível em: <https://arxiv.org/abs/1404.1284>.

48 POLLOCK, E. L.; CEPERLEY, D. M. Path-integral computation of superfluid densities. Phys. Rev. B, American Physical Society, v. 36, p. 8343–8352, Dec 1987. Disponível em: <https://link.aps.org/doi/10.1103/PhysRevB.36.8343>.

49 SINDZINGRE, P.; KLEIN, M. L.; CEPERLEY, D. M. Path-integral monte carlo study of low-temperature ^{4}He clusters. Phys. Rev. Lett., American Physical Society, v. 63, p. 1601–1604, Oct 1989. Disponível em: <https://link.aps.org/doi/10.1103/PhysRevLett.63.1601>.

50 LEGGETT, A. J. Can a solid be "superfluid"? Phys. Rev. Lett., American Physical Society, v. 25, p. 1543–1546, Nov 1970. Disponível em: <https://link.aps.org/doi/10.1103/PhysRevLett.25.1543>.

51 LEGGETT, A. J. On the superfluid fraction of an arbitrary many-body system at t=0. Journal of Statistical Physics, v. 93, n. 3, p. 927–941, nov 1998. ISSN 1572-9613. Disponível em: <https://doi.org/10.1023/B:JOSS.0000033170.38619.6c>.

52 BLAKIE, P. B. Superfluid fraction tensor of a two-dimensional supersolid. Journal of Physics B: Atomic, Molecular and Optical Physics, IOP Publishing, v. 57, n. 11, p. 115301, may 2024. Disponível em: <https://dx.doi.org/10.1088/1361-6455/ad41c1>.

53 MCQUARRIE, D. A. Statistical Mechanics. Sausalito, California: University Science Books, 2000. ISBN 9781891389153.

54 ROSSI, M. et al. Off-diagonal long-range order studied in a soft-core solid: Two-dimensional screened coulomb bosons. Phys. Rev. B, American Physical Society, v. 84, p. 052504, Aug 2011. Disponível em: <https://link.aps.org/doi/10.1103/PhysRevB.84.052504>.

55 HSUEH, C.-H. et al. Quantum crystals in a trapped rydberg-dressed bose-einstein condensate. Phys. Rev. A, American Physical Society, v. 86, p. 013619, Jul 2012. Disponível em: <https://link.aps.org/doi/10.1103/PhysRevA.86.013619>.

56 OLSON, A. J.; WHITENACK, D. L.; CHEN, Y. P. Effects of magnetic dipole-dipole interactions in atomic bose-einstein condensates with tunable<mml:math xmlns:mml="http://www.w3.org/1998/math/mathml"display="inline»<mml:mi>s</mml:mi></mm wave interactions. Physical Review A, American Physical Society (APS), v. 88, n. 4, out. 2013. ISSN 1094-1622. Disponível em: <http://dx.doi.org/10.1103/PhysRevA.88.043609>.

57 HERBST, A. et al. Rapid generation of all-optical <mml:math xmlns:mml="http://www.w3.org/1998/math/mathml»<mml:mmultiscripts><mml:mi mathvariant="normal»k</mml:mi><mml:mprescripts/><mml:none/><mml:mn>39</mml:mn><mml:mn><mml:mn></mml:mn></mml:mmultiscripts></mml:math> bose-einstein condensates using a low-field feshbach resonance. Physical Review A, American Physical Society (APS), v. 106, n. 4, out. 2022. ISSN 2469-9934. Disponível em: <http://dx.doi.org/10.1103/PhysRevA.106.043320>.

58 KOCH, T. et al. Stabilization of a purely dipolar quantum gas against collapse. Nature Physics, Springer Science and Business Media LLC, v. 4, n. 3, p. 218–222, fev. 2008. ISSN 1745-2481. Disponível em: <http://dx.doi.org/10.1038/nphys887>.

59 STOOF, H. T. C.; DICKERSCHEID, D. B. M.; GUBBELS, K. Ultracold Quantum Fields. [S.l.]: Springer Netherlands, 2009.

60 GÓRAL, K.; żEWSKI, K. Rzą; PFAU, T. Bose-einstein condensation with magnetic dipole-dipole forces. Phys. Rev. A, American Physical Society, v. 61, p. 051601, Mar 2000. Disponível em: <https://link.aps.org/doi/10.1103/PhysRevA.61.051601>.

61 TANZI, L. et al. Observation of a dipolar quantum gas with metastable supersolid properties. Phys. Rev. Lett., American Physical Society, v. 122, p. 130405, Apr 2019. Disponível em: <https://link.aps.org/doi/10.1103/PhysRevLett.122.130405>.

62 LU, M. et al. Strongly dipolar bose-einstein condensate of dysprosium. Phys. Rev. Lett., American Physical Society, v. 107, p. 190401, Oct 2011. Disponível em: <https://link.aps.org/doi/10.1103/PhysRevLett.107.190401>.

63 AIKAWA, K. et al. Bose-einstein condensation of erbium. Phys. Rev. Lett., American Physical Society, v. 108, p. 210401, May 2012. Disponível em: <https://link.aps.org/doi/10.1103/PhysRevLett.108.210401>.

64 CHOMAZ, L. et al. Dipolar physics: a review of experiments with magnetic quantum gases. Reports on Progress in Physics, IOP Publishing, v. 86, n. 2, p. 026401, dec 2022. Disponível em: <https://dx.doi.org/10.1088/1361-6633/aca814>.

65 NORCIA, M. A. et al. Two-dimensional supersolidity in a dipolar quantum gas. Nature, v. 596, n. 7872, p. 357–361, ago. 2021.

66 CASOTTI, E. et al. Observation of vortices in a dipolar supersolid. Nature, v. 635, n. 8038, p. 327–331, nov. 2024.

67 ZHANG, Y.-C.; MAUCHER, F.; POHL, T. Supersolidity around a critical point in dipolar bose-einstein condensates. Phys. Rev. Lett., American Physical Society, v. 123, p. 015301, Jul 2019. Disponível em: <https://link.aps.org/doi/10.1103/PhysRevLett.123.015301>.

68 ZHANG, Y.-C.; POHL, T.; MAUCHER, F. Phases of supersolids in confined dipolar bose-einstein condensates. Phys. Rev. A, American Physical Society, v. 104, p. 013310, Jul 2021. Disponível em: <https://link.aps.org/doi/10.1103/PhysRevA.104.013310>.

69 KROTSCHECK, E. Theory of correlated basis functions. In: FABROCINI, A.; FANTONI, S.; KROTSCHECK, E. (Ed.). Introduction to Modern Methods of Quantum Many-Body Theory and their Applications. Singapore: World Scientific, 2002, (Advances in Quantum Many-Body Theory, v. 7). p. 267–330.

70 LEE, T. D.; HUANG, K.; YANG, C. N. Eigenvalues and eigenfunctions of a bose system of hard spheres and its low-temperature properties. Phys. Rev., American Physical Society, v. 106, p. 1135–1145, Jun 1957. Disponível em: <https://link.aps.org/doi/10.1103/PhysRev.106.1135>.

71 LIMA, A. R. P.; PELSTER, A. Beyond mean-field low-lying excitations of dipolar bose gases. Phys. Rev. A, American Physical Society, v. 86, p. 063609, Dec 2012. Disponível em: <https://link.aps.org/doi/10.1103/PhysRevA.86.063609>.

72 LIMA, A. R. P.; PELSTER, A. Quantum fluctuations in dipolar bose gases. Phys. Rev. A, American Physical Society, v. 84, p. 041604, Oct 2011. Disponível em: <https://link.aps.org/doi/10.1103/PhysRevA.84.041604>.

73 BAILLIE, D. et al. Self-bound dipolar droplet: A localized matter wave in free space. Phys. Rev. A, American Physical Society, v. 94, p. 021602, Aug 2016. Disponível em: <https://link.aps.org/doi/10.1103/PhysRevA.94.021602>.

74 BISSET, R. N. et al. Ground-state phase diagram of a dipolar condensate with quantum fluctuations. Phys. Rev. A, American Physical Society, v. 94, p. 033619, Sep 2016. Disponível em: <https://link.aps.org/doi/10.1103/PhysRevA.94.033619>.

75 BOMBIN, R.; BORONAT, J.; MAZZANTI, F. Dipolar bose supersolid stripes. Phys. Rev. Lett., American Physical Society, v. 119, p. 250402, Dec 2017. Disponível em: <https://link.aps.org/doi/10.1103/PhysRevLett.119.250402>.

76 ADHIKARI, S. K. Dynamically stable two- and four-droplet solitons in a very strongly dipolar nacs condensate. Phys. Rev. E, American Physical Society, v. 111, p. 054212, May 2025. Disponível em: <https://link.aps.org/doi/10.1103/PhysRevE.111.054212>.

77 ZHANG, Y.-C.; POHL, T.; MAUCHER, F. Metastable patterns in one- and two-component dipolar bose-einstein condensates. Phys. Rev. Res., American Physical Society, v. 6, p. 023023, Apr 2024. Disponível em: <https://link.aps.org/doi/10.1103/PhysRevResearch.6.023023>.

78 BARKAN, K.; DIAMANT, H.; LIFSHITZ, R. Stability of quasicrystals composed of soft isotropic particles. Phys. Rev. B, American Physical Society, v. 83, p. 172201, May 2011. Disponível em: <https://link.aps.org/doi/10.1103/PhysRevB.83.172201>.

79 SEVRYUK, M. B.; TOENNIES, J. P.; CEPERLEY, D. M. Why are para-hydrogen clusters superfluid? a quantum theorem of corresponding states study. The Journal of Chemical Physics, v. 133, n. 6, p. 064505, 08 2010. ISSN 0021-9606. Disponível em: <https://doi.org/10.1063/1.3458640>.

80 CEPERLEY, D. M. Path integrals in the theory of condensed helium. Rev. Mod. Phys., American Physical Society, v. 67, p. 279–355, Apr 1995. Disponível em: <https://link.aps.org/doi/10.1103/RevModPhys.67.279>.

81 MENDOZA-COTO, A. et al. Exploring quantum quasicrystal patterns: A variational study. Phys. Rev. B, American Physical Society, v. 105, p. 134521, Apr 2022. Disponível em: <https://link.aps.org/doi/10.1103/PhysRevB.105.134521>.

82 GOPALAKRISHNAN, S.; LEV, B. L.; GOLDBART, P. M. Emergent crystallinity and frustration with bose–einstein condensates in multimode cavities. Nature Physics, v. 5, n. 11, p. 845–850, 2009. ISSN 1745-2481. Disponível em: <https://doi.org/10.1038/nphys1403>.

83 GOPALAKRISHNAN, S.; LEV, B. L.; GOLDBART, P. M. Atom-light crystallization of bose-einstein condensates in multimode cavities: Nonequilibrium classical and quantum phase transitions, emergent lattices, supersolidity, and frustration. Phys. Rev. A, American Physical Society, v. 82, p. 043612, Oct 2010. Disponível em: <https://link.aps.org/doi/10.1103/PhysRevA.82.043612>.

84 VAIDYA, V. D. et al. Tunable-range, photon-mediated atomic interactions in multimode cavity qed. Phys. Rev. X, American Physical Society, v. 8, p. 011002, Jan 2018. Disponível em: <https://link.aps.org/doi/10.1103/PhysRevX.8.011002>.

85 MIVEHVAR, F. et al. Cavity qed with quantum gases: new paradigms in many-body physics. Advances in Physics, Taylor & Francis, v. 70, n. 1, p. 1–153, 2021. Disponível em: <https://doi.org/10.1080/00018732.2021.1969727>.

86 KARPOV, P.; PIAZZA, F. Light-induced quantum droplet phases of lattice bosons in multimode cavities. Phys. Rev. Lett., American Physical Society, v. 128, p. 103201, Mar 2022. Disponível em: <https://link.aps.org/doi/10.1103/PhysRevLett.128.103201>.

87 MIVEHVAR, F. et al. Cavity qed with quantum gases: new paradigms in many-body physics. Advances in Physics, Informa UK Limited, v. 70, n. 1, p. 1–153, jan. 2021. ISSN 1460-6976. Disponível em: <http://dx.doi.org/10.1080/00018732.2021.1969727>.

88 KORA, Y.; BONINSEGNI, M. Patterned supersolids in dipolar bose systems. J. Low Temp. Phys., Springer Science and Business Media LLC, v. 197, n. 5-6, p. 337–347, set. 2019. Disponível em: <https://doi.org/10.1007/s10909-019-02229-z>.

89 CINTI, F.; BONINSEGNI, M. Classical and quantum filaments in the ground state of trapped dipolar bose gases. Phys. Rev. A, American Physical Society, v. 96, p. 013627, Jul 2017. Disponível em: <https://link.aps.org/doi/10.1103/PhysRevA.96.013627>.

90 MACRÌ, T. et al. Elementary excitations of ultracold soft-core bosons across the superfluid-supersolid phase transition. Phys. Rev. A, American Physical Society, v. 87, p. 061602, Jun 2013. Disponível em: <https://link.aps.org/doi/10.1103/PhysRevA.87.061602>.

91 KUNIMI, M.; KATO, Y. Mean-field and stability analyses of two-dimensional flowing soft-core bosons modeling a supersolid. Phys. Rev. B, American Physical Society, v. 86, p. 060510, Aug 2012. Disponível em: <https://link.aps.org/doi/10.1103/PhysRevB.86.060510>.

92 SACCANI, S.; MORONI, S.; BONINSEGNI, M. Excitation spectrum of a supersolid. Phys. Rev. Lett., American Physical Society, v. 108, p. 175301, Apr 2012. Disponível em: <https://link.aps.org/doi/10.1103/PhysRevLett.108.175301>.

93 JACKSON, J. D. Classical Electrodynamics. 2nd. ed. New York, NY: Wiley, 1975.

94 LAHAYE, T. et al. The physics of dipolar bosonic quantum gases. Reports on Progress in Physics, v. 72, n. 12, p. 126401, nov 2009. Disponível em: <https://dx.doi.org/10.1088/0034-4885/72/12/126401>.

95 MARCO, L. D. et al. A degenerate fermi gas of polar molecules. Science, United States, v. 363, n. 6429, p. 853–856, jan. 2019.

96 SASLOW, W. M. Superfluidity of periodic solids. Phys. Rev. Lett., American Physical Society, v. 36, p. 1151–1154, May 1976. Disponível em: <https://link.aps.org/doi/10.1103/PhysRevLett.36.1151>.